Shifting the Starspot Paradigm through Imaging Magnetic Structures and Evolution

by

Rachael M. Roettenbacher

A dissertation submitted in partial fulfillment
of the requirements for the degree of
Doctor of Philosophy
(Astronomy and Astrophysics)
in the University of Michigan
2016

Doctoral Committee:

Professor John D. Monnier, Chair
Assistant Research Scientist Alicia N. Aarnio
Professor Fred C. Adams
Professor Nuria P. Calvet
Professor Emeritus Charles R. Cowley

But what about stars other than the sun? If they are at all similar to the sun, should they not have such spots, too, and, if so, is it possible to learn anything about their properties?

The other stars are too distant to be observed as resolved disks with optical equipment now available, or, probably, with optical equipment that will ever be available to us. Thus direct observation, even with a large telescope, is probably out of the question.

—from "Star Spots?" by Gerald E. Kron, 1950

ACKNOWLEDGMENTS

For whatever reason, I have this very distinct memory of sitting in my dorm room at Ohio Wesleyan University and reading a news article about Altair, as the first star vaguely like Sun to be *imaged*, not just resolved (Monnier, 2007). At that point, my research interests were being cultivated by projects imaging starspots via light-curve inversion. As a result, the idea of resolving surfaces and potentially features on those surfaces was exciting. Years later, in an equally distinct memory, I sat in the dingy lodging at NASA Ames reading through a list of potential projects for incoming astronomy graduate students at UM and was incredulous that there was a project resolving starspots on the surfaces of giant stars with interferometry.

With that, I would like to thank John Monnier for supporting my work on and excitement about both spotted stars and interferometry. I could not have imagined a project that would excite me more than this exact project, and I must note the incredible coincidence of the project being possible just when I was arriving at UM. John especially deserves thanks for his patience and guidance—ideally fulfilling his role as advisor. He has encouraged my ideas and independence, for which I am unspeakably grateful. Beyond this, I have enjoyed discussions with John on astronomy and a wide variety of random topics. Thank you, John, for the challenges, encouragements, and opportunities; I am honored to have gotten the chance to work with you. My only regret is not counting the number of times we both showed up dressed in plaid and Chuck Taylors.

I also extend my thanks to the dissertation committee, which, beyond John, in-

cludes (alphabetically) Alicia Aarnio, Fred Adams, Nuria Calvet, and Chuck Cowley who have supported this work and welcomed my infiltration of the departmental Star Formation group meetings, even though my stars formed a long time ago. Additionally, I thank collaborators who have not only helped me push these projects forward, but also have taken the time to encourage me along the way: Bob Harmon, Heidi Korhonen, and Stephen Kane.

I thank my friends near and far for their support and encouragement. I am grateful for the reprieve from science they provided (admittedly, I still did a lot of science discussing with them). Receiving recognition are those that stood together with me (even across vast distances) as we struggled against the beast that is graduate school: (somewhat chronologically) Matt Miller, Ilse Cleeves, Mark Haynes, Nic Scott, Colin Slater, Traci Johnson, and Kamber Schwarz. Outside of academia, Andrew Wiertella deserves acknowledgement for the discussions about art, history, and humanity that kept me grounded.

Finally, family. My parents have been most supportive through this whole endeavor, particularly at the point when I abruptly told them I was going to move to Michigan. Their love and encouragement have been invaluable. My sister has done the same but has additionally provided prospective. I am grateful for the solace from work that she along with her fiancé provided when needed.

TABLE OF CONTENTS

LIST OF FIGURES

Figure

LIST OF TABLES

Table

LIST OF APPENDICES

Appendix

ABSTRACT

Magnetism is present in stars across all masses and evolutionary states. For cool stars with a convective outer envelope, stellar magnetic fields are generated through complex interactions between the convective layer and radiative core due to rotation. Magnetism in cool stars fuels stellar activity, in particular as starspots. Using starspots as a proxy, this work concentrates on imaging stellar magnetism. With state-of-the-art observations and imaging techniques, I investigate shifting the spot paradigm of localized starspots blemishing an otherwise bright surface (analogous to the solar photosphere) to a surface hosting a widespread network of magnetically-suppressed convection. This network is capable of affecting measurements of fundamental stellar parameters, such as radius and temperature, leading to inaccurate mass and age estimates. To accomplish this shift, I use precision *Kepler* data and a light-curve inversion algorithm for studies of stellar differential rotation and starspot evolution. Additionally, with long-baseline interferometric data collected with the Michigan Infrared Combiner (MIRC) at Georgia State University's Center for High Angular Resolution Astronomy (CHARA) Array, I target the bright, spotted, giant primary stars of close binary (RS CVn) systems. For these stars, I combine interferometric detections with radial velocity data to measure orbital and stellar parameters, which are used in concert with long-term photometric light curves to observe ellipsoidal variations, measure gravity darkening, and isolate the starspot signatures. In direct imaging using the interferometric data, I observe a spotted RS CVn star through an entire rotation period to detect canonical starspots, a polar starspot, and globally-suppressed convection. The regions of magnetically-suppressed convection

cover a large fraction of the surface, potentially impacting estimates of stellar parameters. The combination of these efforts provides a start to a new era of detailed imaging and understanding of stellar magnetism, which will impact stellar evolution, star and planet formation, and planetary studies.

CHAPTER I

Introduction

1.1 Solar Magnetism

1.1.1 Observations of Sunspots

For centuries, dark regions on the solar surface have been observed and recorded. China and Korea have still-existing written records of spots on the Sun dating back to 200 BC (Vaquero & Vázquez, 2009). The first known record of drawings of spots came from John of Worcester in 1128. The first systematic recording of the Sun's surface began with Galileo and others in the 17th century, coinciding with the advent of the telescope (see Figure 1.1; Galileo, 1613; Vaquero & Vázquez, 2009, and references therein). In these hand-drawn accounts, details and evolution of sunspots have been observed (see Figure 1.2; Hevelius, 1647).

The telescope led to the frequent (nearly daily) drawings of sunspots that continue today, making the sunspot record one of the longest observational data sets in all of science. Such a baseline of observation has led to the discovery that the number of sunspots present is cyclic—periodically fluctuating from virtually no spots to many and back to few or none every eleven years (Schwabe, 1844). Longer-term features in the sunspot record include a "prolonged sunspot minimum," or Maunder Minimum, lasting several sunspot cycles where the number of sunspots was exceptionally low

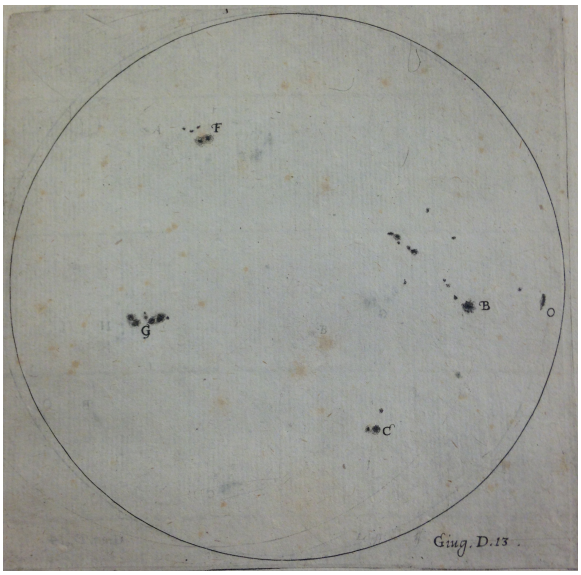

Figure 1.1: Drawing of sunspots on 1613 June 13 by Galileo Galilei. This drawing and the others published alongside it are the beginning of the long-term sunspot observations that continue through today (Galileo, 1613).

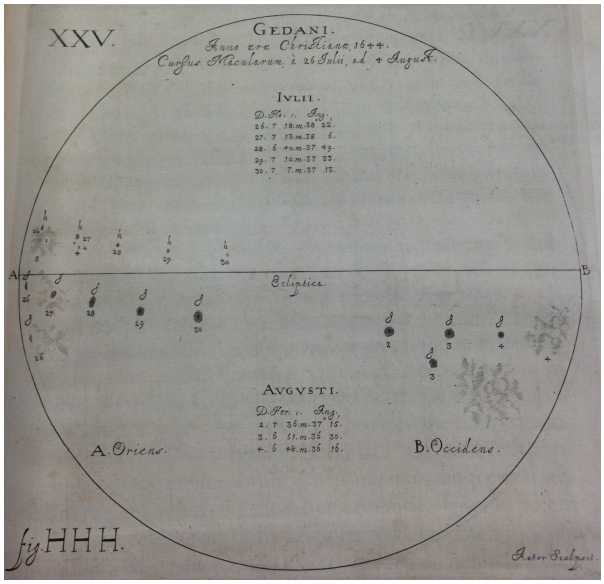

Figure 1.2: Drawing of sunspots by Johannes Hevelius. These sunspot drawings show clear evidence for early detection of structure in sunspots. The dark, umbral region is frequently surrounded by a less dark penumbral region connecting it to the photosphere (Hevelius, 1647).

even when at the maximum of the cycle (Maunder, 1894).

Sophisticated observing techniques now exist to accompany the sunspot drawings, including high-resolution images from ground-based facilities such as GREGOR (a 1.5-m solar telescope at the Observatorio del Teide on Tenerife, Canary Islands) and space-based satellites such as the Solar TErrestrial RElations Observatory (STEREO) and the Solar and Heliospheric Observatory (SOHO). Modern solar observatories additionally have spectrographic and polarimetric capabilities that have allowed for the detection and monitoring of the solar magnetic fields.

The magnetic fields of sunspots were first detected through observations of strong Zeeman splitting of atomic spectral lines (Hale, 1908). Zeeman splitting is a measure of how strongly the energy levels of a particular electronic transition are shifted due to the presence of a magnetic field, approximated by

$$\Delta\lambda_{\mathrm{B}} \propto \lambda_0^2 g B,$$

where $\Delta\lambda_{\mathrm{B}}$ is the average displacement of the spectral line from the expected wavelength without a magnetic field (λ_0), B is the magnetic field, and g is the effective Landé factor (measure of the magnetic sensitivity of the particular spectral line). The strength of the solar magnetic field depends upon the region measured. The solar photosphere typically has a magnetic field strength of a few Gauss (e.g., Borrero & Ichimoto, 2011). Sunspots have much stronger fields that vary across the spots reaching up to a few kiloGauss.

The umbra, the darkest region of the sunspot seen in Figure 1.1 and 1.2, is where the strongest magnetic fields are found (Hale, 1908, measured 2.6-2.9 kG). The temperature in these regions is usually 1000 K cooler than the photosphere ($T_{\mathrm{phot}} = 5777$ K). In the penumbra, the region that often serves as the border between the dark sunspot and the photosphere, magnetic fields are typically a few

hundred Gauss. The penumbra exhibits temperatures of up to 200 K below $T_{\rm phot}$ (Borrero & Ichimoto, 2011).

1.1.2 Dynamo Theory

The generation of solar magnetic fields is described by dynamo theory. Magnetic fields develop in convective cells as a result of cyclonic turbulence and rotational sheer (Parker, 1955). Magnetic fields begin to form at the bottom of the convective zone, where the region meets the radiative core (e.g., Charbonneau, 2005). In the Sun, this region (the tachocline) is located $0.3R_{\odot}$ below the photosphere, as determined by helioseismology (Charbonneau et al., 1999; Basu & Antia, 2003).

In order to create the toroidal field observed on the Sun, the Babcock-Leighton model suggests that the Sun begins with a dipolar field that gets twisted around into a toroidal field due to differential rotation—equatorial regions rotating faster than the polar regions. As the Sun differentially rotates, the magnetic fields are dragged around with rotation as they are embedded in the stellar material. The magnetic field then builds up around the equatorial regions where the fields can be lifted by convective flows to the solar surface. Where the magnetic field is protruding from the surface, the solar material cannot release energy efficiently via convection and is cooler, appearing darker (Babcock, 1961; Leighton, 1964, 1969).

As mentioned above, the Sun exhibits an 11-year periodicity in sunspot number (Schwabe, 1844). During this time, sunspots form at lower and lower latitudes (decreasing in number, as well; see Figure 1.3; Maunder, 1904) as the magnetic field undergoes a polarity reversal. After the reversal occurs, there is a resetting of the location of sunspot formation with the next cycle beginning at the higher latitude with an increased numbers of sunspots.

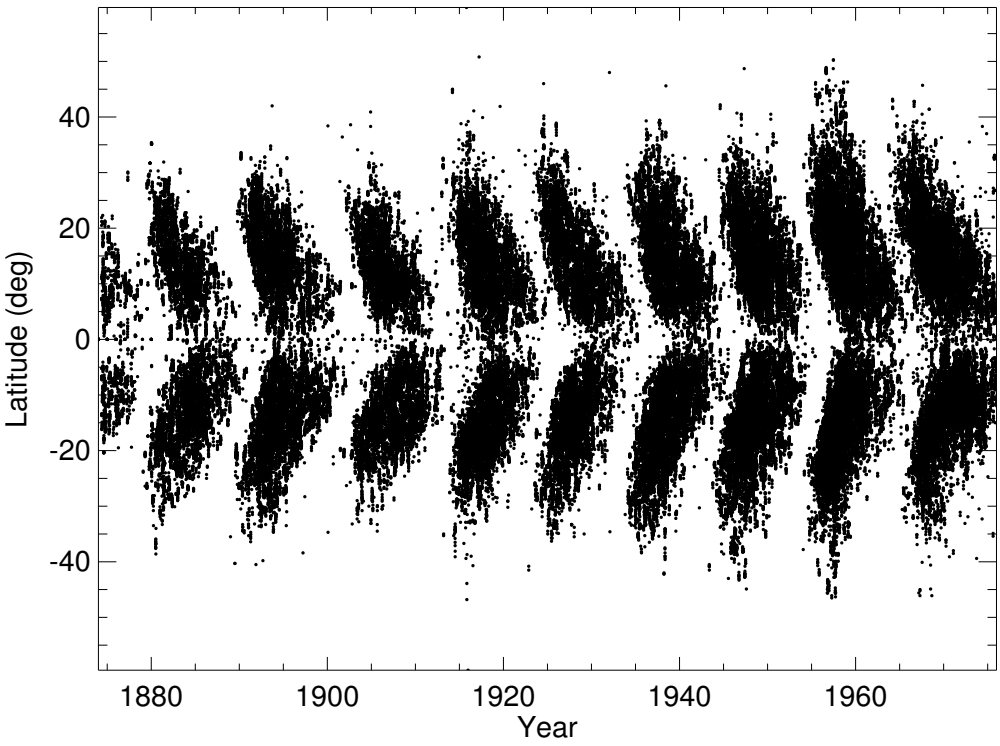

Figure 1.3: "Butterfly" diagram showing the formation latitude of sunspots over time. In an 11-year cycle, the sunspots decrease their formation latitude and number. Once the solar magnetic field reverses, the process begins again at the high latitude. Data plotted are from the archives of the Royal Greenwich Observatory/United States Air Force/National Oceanic and Atmospheric Administration.

1.2 Stellar Magnetism

1.2.1 Observations of Starspots

In the mid-twentieth century, the first serious considerations of whether or not stars other than the Sun should have spots began to develop (e.g., Kron, 1950a). Astronomers noted that since other stars were believed to be like the Sun, spots should be observed on them as well. However, there had been seemingly no definitive evidence of starspots.

Lending support to the search for starspots, Babcock (1947) detected Zeeman splitting on the first star other than the Sun (78 Virginis, a peculiar A star), proving other stars were magnetized (B = 1.5 kG). While Kron (1947) suggested that the eclipsing binary system AR Lacertae (AR Lac) had variable patches due to modulations observed in the light curve during an eclipse, he did not connect them to sunspots at that time. The first suggestion that this sort of variation was analogous to sunspots came from Kron (1950b) for low-mass M dwarfs.

Throughout the years, particularly after the development of photoelectric detectors, many long-term studies of spotted stars have begun. For example, the ground-based Automated Photometric Telescopes at Mount Hopkins Observatory, AZ operated by Tennessee State University have been observing variable stars for nearly thirty years. These long-term studies allow for studies of individual stars showing a variety of spot features including evolving starspots, differential rotation, and active longitudes (e.g., Henry et al., 1995; Roettenbacher et al., 2011).

These studies have been vital for understanding the brightest of stars with large variations, but space-based light curves have allowed for the detection of more subtle sunspot-like spot features on stars. Satellites including MOST, CoRoT, and *Kepler* have allowed for detailed studies of starspots (e.g., Mosser et al., 2009; Savanov, 2011a, and Chapters II and III).

Similar to the analysis of solar magnetic fields, measuring Zeeman splitting of atomic and molecular lines via spectroscopy is also used to detect and quantify magnetic fields on stars (e.g., Babcock, 1947; Mathys, 1989). However, the signal of the splitting can be easily obscured by rotational line broadening making other means of detection necessary (Donati & Landstreet, 2009).

Spectropolarimetry, often in conjunction with Doppler imaging (see below), is used to measure and dissect stellar magnetic fields (Donati et al., 2007). These observations involve detecting combinations of linear and circular polarizations of light, as well as Zeeman broadening. The polarization occurs from the magnetic field orientation, allowing astronomers to reconstruct the surface spot features.

1.2.2 Theory

Polarimetric studies of cool stars with starspots and large convective envelopes have revealed complex structures suggesting that stellar magnetic fields can be even more complicated than those of the Sun (Donati & Landstreet, 2009). Stellar magnetic fields of cool stars are believed to occur by the same dynamo action that causes solar magnetic fields (Donati & Landstreet, 2009, and references therein). However, many active stars are rotating much more rapidly than the Sun, pushing the limits of solar dynamo theory. Donati & Landstreet (2009) discuss that large-scale stellar magnetic fields detected with spectropolarimetry are complicated with several distinct populations that depend on the rotation and mass. Young (rapidly-rotating), low-mass stars are found to have the strongest magnetic fields, while older (more slowly rotating) have weaker fields. This slow-down in single stars is due to the magnetic fields extending beyond the stellar surface and coupling with stellar winds (ejected charged particles). This coupling creates a drag as the star rotates, slowing it down (e.g., Schatzman, 1962).

While activity is correlated with both rotation and spectral type (Noyes et al.,

1984), for late-type, main-sequence stars, the amount of activity increases as the rotation period decreases. However, there is a limit beyond which faster rotation will not result in an increase in activity because it has saturated (Noyes et al., 1984; Pizzolato et al., 2003).

Saturation arises when magnetic activity does not increase below a specific Rossby number ($R_{\rm o} \equiv P_{\rm rot}/\tau_{\rm conv}$, where $P_{\rm rot}$ is the rotation period and $\tau_{\rm conv}$ is the convective turnover time; see Figure 1.4). Saturation occurs for a variety of magnetic activity measures (Hα, Ca II H and K, and X-ray emission and Zeeman-splitting of FeH absorption lines; e.g., Mamajek & Hillenbrand, 2008; Reiners et al., 2009; Wright et al., 2011). For M dwarfs, in particular, Reiners et al. (2009) showed that the Rossby number at which this saturation happens is roughly the same for Hα, FeH, and X-ray activity measures ($R_{\rm o} \sim 0.1$). Reiners et al. (2009) suggested that there are two possible explanations for the saturation: the star is limited in the strength of magnetic fields that it can produce or the stellar surface cannot sustain more regions where strong magnetic fields are suppressing convection (starspots).

For stars that have evolved off of the main sequence, the stars follow a different power law with decreasing period (see Figure 1.4). However, present data do not show clear evidence of saturation (e.g., Gondoin, 2005; Aurière et al., 2015).

1.2.3 RS Canum Venaticorum Stars

Many stars are much more active and in very different environments and evolutionary states than the Sun, which may push solar dynamo theories beyond their limits of applicability. One such group testing the limits of dynamo theories consists of active, evolved, close binary stars—RS Canum Venaticorum (RS CVn) stars. These typically involve a bright, giant primary star and a faint main-sequence companion (Hall, 1976). With rotation and orbital periods often on the order of a few weeks, the primary star has been spun-up by tidal locking with the companion. RS CVns

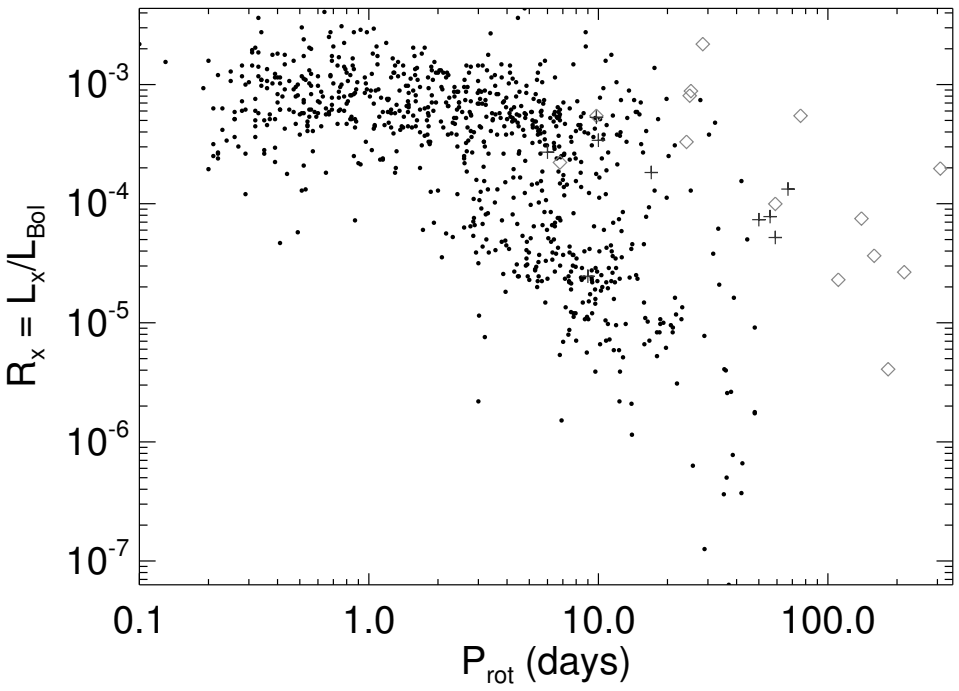

Figure 1.4: Activity, measured by the ratio of X-ray to bolometric luminosity, $R_{\rm X}$, saturates with small Rossby numbers ($R_{\rm o} \equiv P_{\rm rot}/\tau_{\rm conv}$). This trend is not well-understood and is observed across main-sequence spectral types in a variety of activity measures. The black dots represent main-sequence stars, the plusses and diamonds are giant stars. The data plotted appear in Wright et al. (2011), Gondoin (2005), and Aurière et al. (2015), respectively.

are known to exhibit starspots typically with more surface coverage than sunspots (e.g., XX Trianguli had a spot covering 11% of its surface, Strassmeier, 1999) that are detected with a variety of imaging techniques (see below).

RS CVn starspots tend to be longer-lived than sunspots (e.g., II Pegasi, Roettenbacher et al., 2011) and can be located at high latitudes, including polar regions (e.g., ζ Andromedae, Kővári et al., 2007a). Because these stars are cool giants with inflated radii (and deep convective zones) and rotation periods on the order of a few weeks (see Chapters IV and V, for example), they tend to have more activity manifesting as larger starspots. Polar starspots are believed to be caused by meridional flows that pull magnetic flux toward the poles at the top of the convective cells (Holzwarth et al., 2006).

1.2.4 Starspots and Planet Signals

While large starspots are of interest to imaging stellar surface features and are useful for studying the complex stellar magnetic fields, starspots more comparable to sunspots are of interest for searching for planets, as the signatures of starspots can hide or mimic the signals of planets. Saar & Donahue (1997) studied slowly-rotating main-sequence stars (F8 - K7) and showed that starspots can shift radial velocity curves tens of meters per second. In late M dwarfs, the radial velocity shifts due to starspots can exceed 100 m s^{-1} (Barnes et al., 2015).

In the attempts to find an Earth-like planet in an Earth-like orbit around a Sun-like star—a true Earth-analog—a signature of $\sim$ m s^{-1} will overwhelm the reflex motion of the star caused by the planet ($\sim$ 10 cm s^{-1}). The spectroscopic resources presently being developed will be capable of detecting radial velocity shifts of $\sim$ 10 cm s^{-1} (e.g., Échelle SPectrograph for Rocky Exoplanet and Stable Spectroscopic Observations (ESPRESSO) for the European Southern Observatory's Very Large Telescope and Yale's EXtreme PREcision Spectrometer (EXPRES) for Lowell Observatory's

Discovery Channel Telescope). In order to detect an Earth-analog, radial velocity studies will have to carefully account for the jitter caused by even the smallest starspots.

Starspots additionally impact planetary transits in light curves. For example, starspots have been found to cause transit timing variations and affect the depth of transits (e.g., Kawahara et al., 2013; Mazeh et al., 2015). Variations from starspots within an eclipse have been used to improve the orbital parameters of transiting systems, namely obliquity (Sanchis-Ojeda et al., 2011).

A number of studies, including those mentioned above, have investigated the effects of starspots on the detection of planets. With ever-improving observational methods, the nature of starspots and their impact on planetary detections must be better understood.

1.3 Imaging Techniques

While the signatures of magnetic fields can be observed through a variety of techniques, in this work, I will focus on imaging starspots. In this section, I will discuss the techniques available for imaging starspots, each with a unique set of advantages and disadvantages (see Table 1.1).

Table 1.1. Stellar Surface Imaging Techniques

Method Name	Advantages	Disadvantages	Sample Instruments/Telescopes
Light-curve inversion	Requires widely-available photometers	Poor latitude constraints	*Kepler*/*K2*
	Constrains starspot longitude	Weak inclination constraints	MOST, CoRoT, TESS*
	Applied to wide variety of stars	Detects only rotational modulations	Ground-based surveys
Doppler imaging	Detects rotational and stationary features	Requires rapidly-rotating stars	UVES/VLT
	Constrains starspot longitudes	Requires accurate absorption line modeling	HARPS/ESO La Silla
	Constrains starspot latitudes	Degeneracy across hemispheres	FIES/NOT
Aperture synthesis	Determines rotation axis on sky (PA, i)	Few observational facilities	CHARA/MIRC
	Fewer degeneracies spot location	Requires spatially-large stars	NPOI/VISION*
	No fundamental limit to resolution	Presently few accessible targets	VLTI/PIONIER

Note. — * denotes a future resource or potential capability.

1.3.1 Light-Curve Inversion

Light-curve inversion is a method that reconstructs the stellar surface from only variations in photometric observations (Kiurkchieva, 1989), resultant from starspots rotating in and out of view. The algorithms that reconstruct the stellar surface from a light curve break the surface into a series of patches that are varied individually to recreate a stellar surface that would emit the observed light curve. To vary the patches, the algorithm must use a regularizer to attempt to find a unique solution to the inversion. Typically, these regularizers work to balance fitting the observed light curve to account for the large spot structures without overfitting, ultimately imaging noise. Additionally, algorithms require a bias parameter favoring dark spots on a bright surface (analogous to sunspots) compared to bright spots. In order to further reduce degeneracy, light-curve inversion algorithms can require input of photospheric and spot temperatures, as well as inclination angles. For a more detailed discussion of a specific light-curve inversion algorithm, see Section 2.5.

The primary advantage to light-curve inversion techniques is that they can be applied to a wide variety of stars, especially faint stars. Using either ground- or space-based photometry, light-curve inversion requires only a light curve with reasonably complete phase coverage (e.g., Roettenbacher et al., 2011, reconstructed large spots of II Pegasi using only twelve data points; see Figure 1.5).

Because light-curve inversion methods rely on rotational modulation for mapping, they can locate starspots in longitude well. Weak information on relative latitudes can be distinguished for a single bandpass. Multiple simultaneously-collected light curves will allow for better determination of spot latitudes, but will still fail to yield absolute latitude information (Harmon & Crews, 2000). The importance of latitude information is that it allows for the determination of differential rotation, which can give insight into the structure of the outer convective layers of stars.

Light-curve inversion has been used with ground-based, multi-bandpass light curves

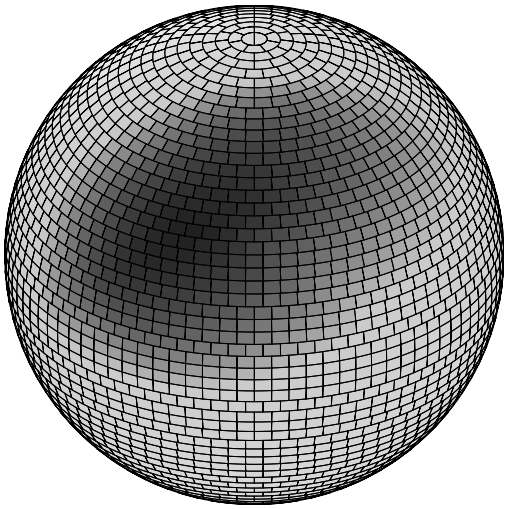

Figure 1.5: Reconstructed surface of II Pegasi, an RS CVn star known to present large starspots. This reconstruction used twelve data points (largest phase gap $\sim$ 0.15). This figure is excerpted and reprinted with permission from Roettenbacher et al. (2011).

to identify starspots and observe their covering fraction, evolution, and differential rotation (e.g., Roettenbacher et al., 2011). Light-curve inversion has also been more recently used to study starspots with space-based photometers observing long-term light curves (e.g., Savanov, 2011a, and Chapters II and III). Given the wealth of data as a result of recent and upcoming space-based photometric planet searches (e.g., *Kepler*/*K2* and the Transiting Exoplanet Survey Satellite (TESS)), light-curve inversion techniques can take advantage of these data, creating unprecedented studies of stellar activity.

1.3.2 Doppler Imaging

Doppler imaging is a method that reconstructs a stellar surface based upon the motion of features that move across absorption lines as the star rotates and spots come in and out of view. Due to the cooler temperatures of the spots, these features can resemble small emission signatures that fill in the absorption lines to a degree that depends on the size, location, and temperature of the surface feature. For large spot

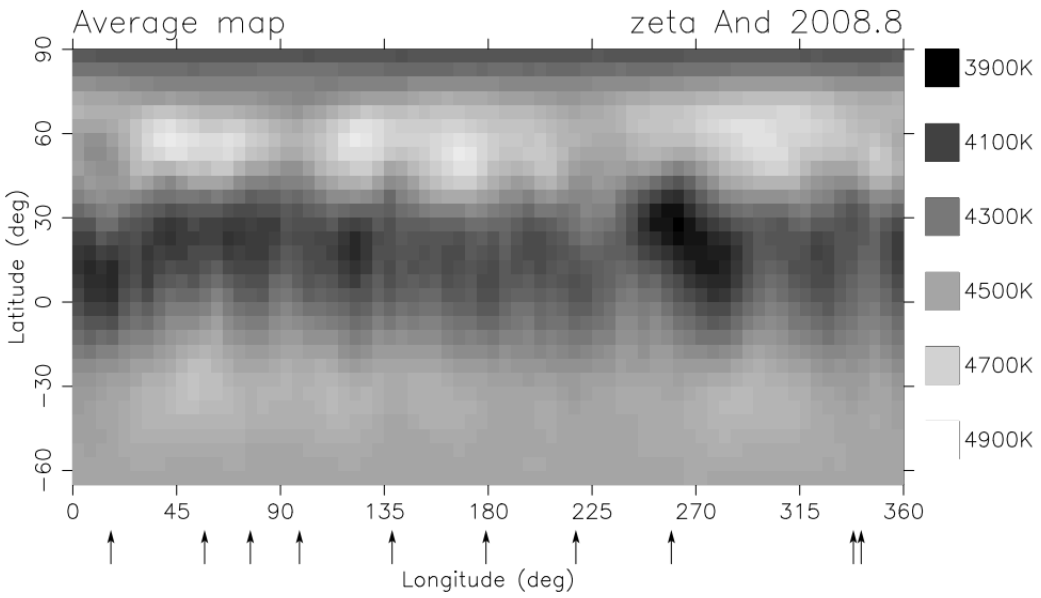

Figure 1.6: Reconstructed surface of ζ Andromedae, an RS CVn star known to present large starspots. This reconstruction combined six spectral lines observed at ten epochs. This figure is reprinted with permission from Korhonen et al. (2010).

structures, the entire absorption line can shift mimicking a radial velocity variation. Using a full rotation period of observations, the star is imaged at once using the motion of the bumps across absorption lines to locate the starspot on the surface (Vogt & Penrod, 1983, see also Figure 1.6).

Doppler imaging requires the stars to be rapidly rotating such that the rotational profile of the spectral line is broader than the intrinsic linewidth (Vogt & Penrod, 1983, suggests $v \sin i > 30$ km s^{-1}). Because the Sun and similar stars have low rotation velocities ($\sim$ 2 km s^{-1} for the Sun), this constraint only allows Doppler imaging on the young stars or evolved stars in a close binary.

Like light-curve inversion, there are some uncertainties associated with locating the latitude of the starspot. In the case of Doppler imaging, the latitude of the starspot can be obtained by the location in the absorption lines where the starspot begins to impact the line (i.e., higher-latitude spots will manifest lower in the core

of the line). Particularly in the case of high inclinations, a degeneracy remains between which hemisphere the starspot belongs in, as Doppler imaging (and light-curve inversion) will favor reconstructing a spot in the hemisphere facing Earth.

Doppler imaging requires astronomers to model the stellar spectrum. Because starspots manifest as perturbations of absorption lines, the quality of the Doppler image depends on the ability to model the stellar spectrum (including temperature, surface gravity, and micro- and macro-turbulence). For example, a slightly incorrect model could lead to the core of the absorption line being filled slightly, which would mimic the signature of a polar starspot.

Doppler imaging has been been used to image the surfaces of a variety of stars, including giant stars with large starspots (e.g., Strassmeier, 1999) to brown dwarfs with signatures of clouds (e.g., Crossfield et al., 2014). With high-resolution spectrographs at telescopes of all sizes, Doppler imaging is possible for a large number of spotted, rapidly rotating stars.

1.3.3 Aperture Synthesis

Aperture synthesis imaging requires interferometric observations to image the stellar surface. Optical (visible and infrared wavelengths) long-baseline interferometry uses multiple telescopes separated by hundreds of meters to resolve the structures on the surface of stars. Each pair of telescopes observes a particular point in the target's *uv* plane (the Fourier transform of the stellar brightness on the sky). In order to fill in the *uv* plane as completely as possible to obtain the best image, observations require as many telescopes pairs as possible. The most telescopes in an optical interferometric array is presently six with baselines measuring up to 331m (ten Brummelaar et al., 2005). As the Earth rotates, the *uv* coverage is extended further through the changing lengths of the project baselines. Typically, an object will be imaged as a sort of snapshot, based on a single set of observations (see Figure 1.7).

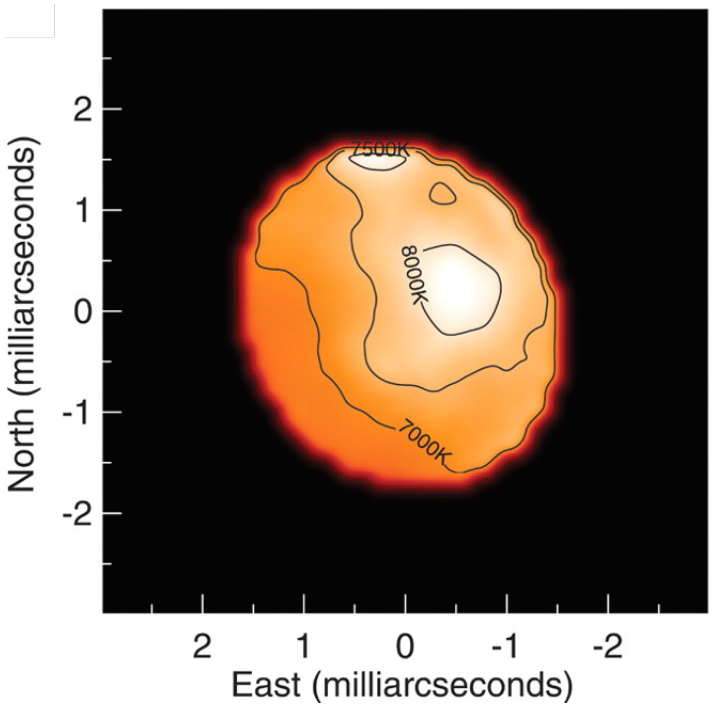

Figure 1.7: Reconstructed surface of Altair, a rapidly-rotating main sequence A star. This reconstruction used four telescopes at the CHARA Array with the light combined with the Michigan InfraRed Combiner (MIRC). This figure is reprinted with permission from Monnier (2007).

In order to observe the complete surface in the same sense as Doppler and light-curve inversion, snapshots of the stellar surface are not sufficient. Observing the target over an entire night allows the rotation of the Earth extend uv coverage further. To improve uv coverage across the rotating surface, the target must be observed frequently throughout its rotation, a novel technique for which a new imaging-on-a-sphere technique can be utilized (Monnier et al., in prep.).

Aperture synthesis imaging is a direct mapping of surface features; therefore, this technique does not suffer the degeneracies in discerning latitude or hemisphere of light-curve inversion and Doppler imaging. Interferometric images accurately reflect the observed object as it appears on the sky. With this, parameters including position angle and inclination are readily measured.

The disadvantage of this sort of imaging is that there are only a few targets that can be resolved with the present interferometric facilities. In order to image the starspots using an interferometer, the stars are required to be nearby (so as to be spatially large), bright, and spotted. Also restrictive is the time required to obtain detailed images of the targets available as the best uv coverage for imaging requires observing stars for complete rotation periods.

Because interferometry is only limited in resolution by baseline length, should interferometers be extended to have larger baselines, more detailed images of stellar surfaces will be possible. Additional gains in resolution can be obtained by probing shorter wavelengths. While few in number (see Chapter VII), the stars that can have surface features resolved can provide information for stellar activity, formation, and evolution.

1.4 Dissertation Overview

This work consists of five chapters that seek to describe spotted stars to an unprecedented degree using state-of-the-art observational facilities and analyses. These

chapters are followed by concluding remarks that highlight the work and suggest directions for future efforts.

In Chapter II, I introduce the work that I have done applying the Light-curve Inversion (LI; Harmon & Crews, 2000) algorithm to data from the *Kepler* satellite on one spotted star, KIC 5110407. In this chapter, I present details of the algorithm and discuss its application to the data. I measure differential rotation KIC 5110407 finding that it occurs in the same sense as that of the Sun (equatorial material rotating more rapidly than polar material), but to a lesser extent, as predicted by theory. I also explore the relationship between white-light flare timing and the position of the largest starspot features finding that only the largest flares occur when the spots are facing *Kepler*. In the associated Appendix A, I include the complete set of reconstructed surfaces.

In Chapter III, I demonstrate LI on another *Kepler* star, KOI-1003. For this eclipsing binary system, I not only reconstruct the stellar surface of the primary star (Appendix B), but I also explore the effect of starspots on the primary eclipses present in the data and characterize the system. This work is the first step in applying LI more widely to understand how starspots impact the detection and characterization of low-mass companions.

In Chapter IV, I introduce a detailed study of σ Geminorum (σ Gem), a binary system with a giant primary star and previously-unseen companion. Combining interferometric detections of the companion with new and archival radial velocity curves of both stellar components allows for measuring orbital and stellar parameters. From just those parameters, I model the light curve, which when compared to an archival light curve, reveals ellipsoidal variations. These ellipsoidal variations have been previously misidentified as active longitudes, specific longitudes at which starspots preferentially form. When accounting for the ellipsoidal variations, σ Gem is shown to still be spotted. This analysis also provides a measurement of gravity

darkening.

In Chapter V, I performed the same analysis as in Chapter IV on o Draconis (o Dra), another binary system with a giant primary star and a previously-unseen companion. o Dra is not found to be as spotted as previous studies had shown, but those mistaken features are actually the combination of ellipsoidal variations and the secondary eclipse. Because o Dra does not present large starspots, the measurement of gravity darkening for this star is well-constrained.

In Chapter VI, I use two interferometric data sets to image ζ Andromedae (ζ And), a star like σ Gem and o Dra, but with previously-known ellipsoidal variations. Using a new imaging-on-a-sphere technique to combine a full rotation period of data, I image the star to verify the existence of high-latitude spots that have been observed with Doppler imaging but have not been otherwise detected. The interferometric images also highlight globally-suppressed convection believed to be caused by widespread, strong magnetic fields stifling convection across the stellar surface. This spot network is in opposition to the canonical paradigm of starspots as isolated dark regions analogous to sunspots.

Finally, in Chapter VII, I discuss the results of the previous chapters in the context of stellar magnetism and activity. I also develop suggestions for future extensions of these works.

CHAPTER II

Imaging Starspot Evolution on *Kepler* Target KIC 5110407 Using Light-curve Inversion

2.1 Preface

This chapter is adapted from work of the same title appearing in the Astrophysical Journal, Volume 767, 60 (Roettenbacher et al., 2013). This work is coauthored by John D. Monnier, Robert O. Harmon, Thomas Barclay, and Martin Still. The paper is adapted and partially reproduced here under the non-exclusive rights of republication granted by the American Astronomical Society to the paper authors.

Additional information (Section 2.6.3) from later work investigating the flares of the target in the complete *Kepler* data set is from proceedings from the 18$^{\text{th}}$ Cambridge Workshop on Cool Stars, Stellar Systems, and the Sun held at Lowell Observatory in Flagstaff, AZ in June 2014 (Roettenbacher et al., 2015b). The coauthors on these proceedings are John D. Monnier and Robert O. Harmon.

For my part in this project, I obtained the *Kepler* light curves and removed the cotrending basis vectors to prepare the data for these works. I removed the flares from the light curve and prepared the individual rotation periods (which I determined) for the application of Light-curve Inversion (LI). I applied LI to each light curve for a variety of inclination angles and determined the best rms value for

each. I determined the location and size of each starspot, analyzing spot coverage and differential rotation. I compared the timing of the flaring events with the location of the darkest portion of the starspot. I created all of the figures and tables for these works, as well as wrote the majority of the paper (except for the section on LI and some of the text about *Kepler* observations) and all of the conference proceeding.

2.2 Abstract

The *Kepler* target KIC 5110407, a K-type star, shows strong quasi-periodic light curve fluctuations likely arising from the formation and decay of spots on the stellar surface rotating with a period of 3.4693 days. Using an established light-curve inversion algorithm, we study the evolution of the surface features based on *Kepler* space telescope light curves over a period of two years (with a gap of .25 years). At virtually all epochs, we detect at least one large spot group on the surface causing a 1–10% flux modulation in the *Kepler* passband. By identifying and tracking spot groups over a range of inferred latitudes, we measured the surface differential rotation to be much smaller than that found for the Sun. We also searched for a correlation between the seventeen stellar flares that occurred during our observations and the orientation of the dominant surface spot at the time of each flare. No statistically-significant correlation was found except perhaps for the very brightest flares, suggesting most flares are associated with regions devoid of spots or spots too small to be clearly discerned using our reconstruction technique. While we may see hints of long-term changes in the spot characteristics and flare statistics within our current dataset, a longer baseline of observation will be needed to detect the existence of a magnetic cycle in KIC 5110407.

2.3 Introduction

Starspots are the clearest manifestation of magnetic fields on the surface of stars. The contrast of dark starspots against a bright photosphere results from strong magnetic fields inhibiting convection on low-mass stars (Strassmeier, 2009). The structure and evolution of stellar magnetic fields are poorly understood, but observing the formation and evolution of starspots could provide insight into modeling the stellar magnetic dynamo (Brandenburg & Dobler, 2002; Berdyugina, 2005; Hotta & Yokoyama, 2011).

Spots have been imaged on stars using a variety of techniques. For bright stars that are rotating quickly, high-resolution spectroscopy can follow spot motions across the surface by tracking variations in absorption lines (Vogt & Penrod, 1983) through a rotational cycle. This technique is called *Doppler imaging* and has successfully detected differential rotation (e.g. Hatzes, 1998; Collier Cameron et al., 2002; Kővári et al., 2007b) as well as polar spots (e.g. Strassmeier et al., 1991; Mackay et al., 2004) in some sources. For stars rotating more slowly, new interferometric facilities can image spots directly using *aperture synthesis imaging* techniques. Unfortunately, this technique can only be applied to nearby stars of large angular size (e.g. Parks et al., 2011). The vast majority of spotted stars cannot be imaged with either of these techniques because of their inherent faintness.

The most general method for imaging spots is through the *light-curve inversion* technique, which relies only on measuring total flux variations (e.g. Korhonen et al., 2002; Roettenbacher et al., 2011). A specific non-linear inversion algorithm for this purpose was developed by Harmon & Crews (2000) and was called "Light-curve Inversion" (LI). In Roettenbacher et al. (2011), LI was tested using nearly twenty years of ground-based photometry on the spotted star II Pegasi (II Peg). The results from LI were shown to be generally consistent with contemporaneous Doppler imaging studies (Berdyugina et al., 1998, 1999; Gu et al., 2003), although both methods

suffer from some degeneracy when the inclination of the star is unknown. Up until recently, light-curve inversion techniques have only been applied using ground-based data with the usual limitations in signal-to-noise and large gaps in temporal coverage. In the study of Roettenbacher et al. (2011), up to ten rotation cycles were needed to fold a light curve complete enough to create a surface map making it difficult to quantitatively determine a rate of differential rotation, an important measurement for understanding stellar activity.

The launch of the *Kepler* space telescope in 2009 has ushered in a new era for precision photometry in astronomy, overcoming many of the limitations of ground-based photometric monitoring. *Kepler* monitored over 10^5 stars simultaneously with nearly continuous time coverage and with better than millimagnitude precision. While much initial excitement has focused on transits of Earth-like planets as well as fundamental contributions to asteroseismology, *Kepler* data are also poised to revolutionize the study of active stars through the modeling of the light curves. For example, Frasca et al. (2011) and Fröhlich et al. (2012) recently modeled the *Kepler* light curves of rapidly-rotating young solar analogues using analytic models with seven or more spots. With a technique based upon the algorithm described in Savanov & Strassmeier (2008), the light curves of several low-mass, photospherically-active stars have been analyzed to find active longitudes and differential rotation (e.g. Savanov, 2011a,b; Savanov & Dmitrienko, 2011, 2012).

In this chapter, we perform the first LI image reconstructions of an active star based on *Kepler* data, focusing on the K-type star KIC 5110407. In Section 2.4, we introduce our target and describe the *Kepler* observations. In Section 2.5, we give a detailed overview of LI, including an explanation of all assumptions and the known degeneracies with the method. In Section 2.6, we present our example image reconstructions and explain how spots were identified and tracked through time. We discuss spot characteristics, quantify the amount of observed differential rotation, and

analyze the timing of stellar flares we detected during our observations. We include a brief summary of our findings in the context of other recent work and our conclusions in Section 2.7; Appendix A contains image reconstructions for all 172 epochs.

2.4 Observations

Street et al. (2005) identify KIC 5110407 (2MASS J19391993+4014266) as a BY Dra star, a star with short-period photometric variations on timescales of less than a month, with a period of $P = 3.41 \pm 0.47$ days. The *Kepler* light curve supports this classification, finding variations in magnitude as large as $\Delta K_{\rm p} = 0.13$ ($K_{\rm p} = 16.786$). According to the *Kepler Input Catalog*, KIC 5110407 has an effective temperature of $T_{\rm eff} \sim 5200$ K, a logarithmic surface gravity of $\log g \sim 3.8$, metallicity of [Fe/H]~ -0.18, and radius $R \sim 2.2\ R_{\odot}$ (Brown et al., 2011). The effective temperature is consistent with those provided in Pinsonneault et al. (2012) and indicates KIC 5110407 is an early K-type star (Kenyon & Hartmann, 1995). Adopting these values, we find KIC 5110407 to be located about 4 kpc away, with luminosity $3.2 L_{\odot}$. Assuming the star is quite young based on the observed rapid rotation, we find a mass of $M = 1.7 M_{\odot}$ using Siess et al. (2000) evolutionary tracks. Alternatively, Street et al. (2005) suggested this star is a member of NGC 6819, a 2.6 Gyr old cluster about 2.4 kpc away (Yang et al., 2013). High-resolution spectroscopy of this target would allow for a more precise determination of $\log g$, which would independently constrain the stars evolutionary state.

KIC 5110407 was observed by the *Kepler* space telescope (Borucki et al., 2010; Koch et al., 2010) as a target of the Guest Observer program. *Kepler* data naturally divides into quarters owing to the semi-regular 90° roll of the telescope. One quarter spans approximately 93 days after which a roll occurs and the star falls onto a different detector. KIC 5110407 was observed over an observational baseline of 736 days between Quarters 2–9, save for Quarter 6 when the star fell on a failed detector.

These observations were undertaken in Long Cadence mode where the brightness of a star is recorded with a time resolution of 29.4 min (Jenkins et al., 2010).

We used the Simple Aperture Photometry flux time series from the Kepler FITS files (Thompson & Fraquelli, 2012). These data have undergone basic calibration (Quintana et al., 2010), but no attempt has been made to remove the majority of instrumental systematics from the data. In order to remove systematics such as thermally-induced focus changes and differential velocity aberration, we applied cotrending basis vectors (CBVs)[1]. These data contain information on the instrumental signals pertaining to each CCD for every Quarter and take the form of time series data. We used the *kepcotrend* tool (the use of which is discussed by Barclay et al., 2012) from the PyKE software package (Still & Barclay, 2012) to linearly fit and subtract basis vectors. We found fitting the first four basis vectors to each Quarter of data gave optimal results, i.e. systematics were largely removed but starspot activity was not overfit (Quarters 4 and 8 were fit with the first three basis vectors). Following calibration, our work shows point-to-point ($\Delta T = 30$ mins) rms noise fluctuations of approximately 1600 ppm, not too different from the post-flight measures of 2100 ppm estimate for a 16.74 mag target (`http://keplergo.arc.nasa.gov/CalibrationSN.shtml`). Since the target object shows a rotational modulation of approximately 0.13 mag, we see that a typical light curve has a point-to-point dynamic range of ~ 75. By comparison, the Roettenbacher et al. (2011) II Peg light curve had a lower dynamic range (~ 30 for Johnson V) but for an object approximately ~ 6000 times brighter with longer averaging times, and much poorer phase coverage. The now largely-systematic free light curve of KIC 5110407 (see Figure 2.1) is ready to be divided into light curves of single rotation periods, normalized to the maximum flux of that rotation cycle, and analyzed with LI.

[1]Available at `http://archive.stsci.edu/kepler/cbv.html`

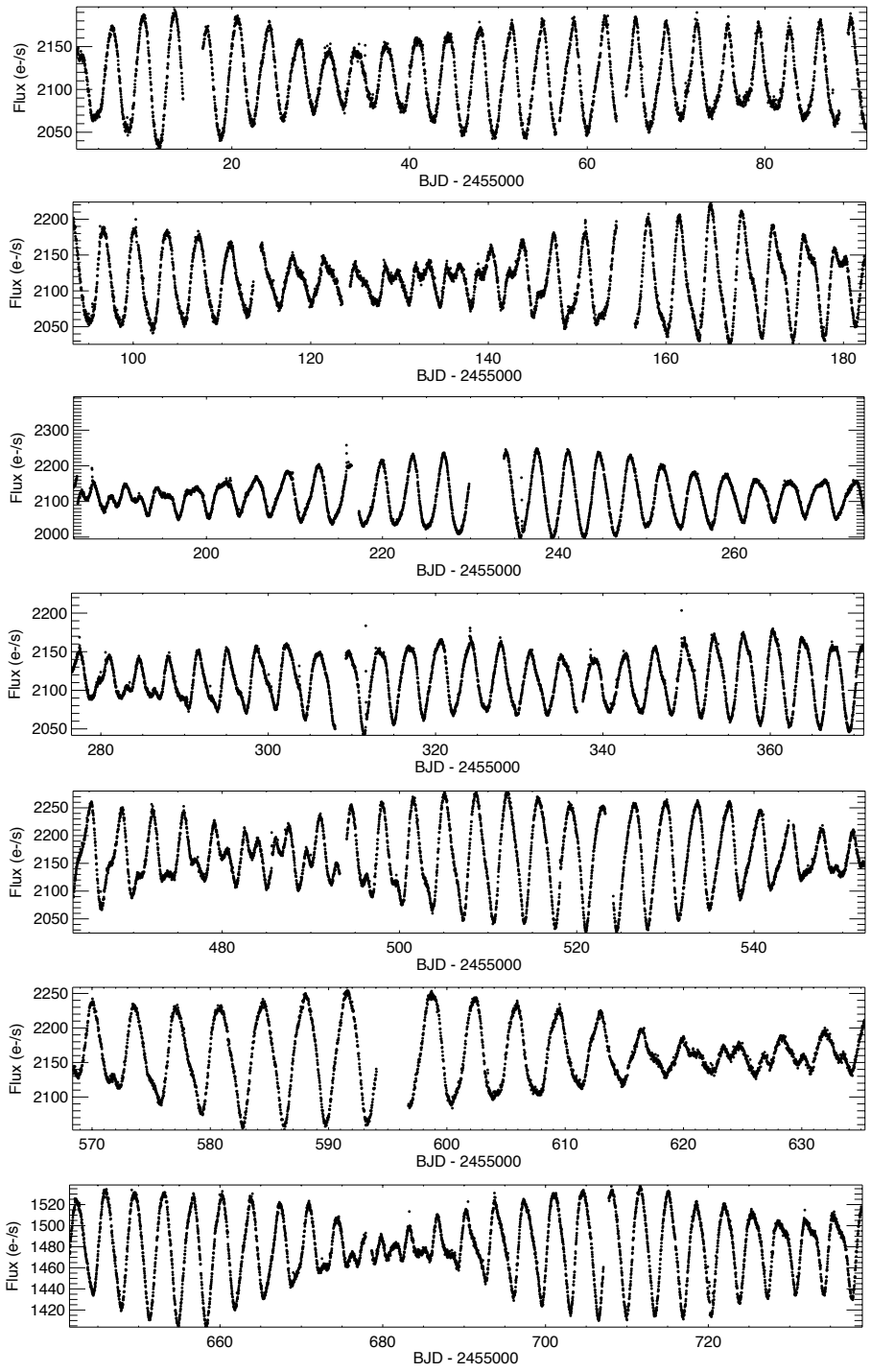

Figure 2.1: Long cadence light curves of KIC 5110407 for Quarters 2−5 and 7−9 after the cotrending basis vectors have been removed.

2.5 Light-curve Inversion (LI) Method

Information about the spot geometry and evolution can be inferred from changes in the light curve. For example, a single spot will be seen as a periodic modulation of the flux level at the rotational period. As a spot grows or reduces in strength, this modulation will change. Furthermore, spots at different latitude will affect the light curve in subtly different ways as they rotate in and out of view and are affected by limb-darkening. In general, there may be multiple spots or spot groups that are each evolving simultaneously on the surface. In this work, we attempt to quantify these photometric variations by creating surface maps using Light-curve Inversion (LI; Harmon & Crews, 2000). The LI method has been described elsewhere in detail and extensively tested on simulated and observational data (Harmon & Crews, 2000; Roettenbacher et al., 2011). In this section, we provide an introduction to the technique and provide details on its specific application for KIC 5110407.

In LI, the stellar surface is modeled as a sphere subdivided into N bands parallel to the equator having equal extents in latitude, with each band further subdivided into patches of equal extents in longitude which are "spherical rectangles." The number of patches in a band is proportional to the cosine of the latitude in order that all the patches on the surface have nearly equal areas. In this work, there are 60 latitude bands and 90 patches in the two bands which straddle the stellar equator, resulting in a partition having 3434 patches, each approximately 12 sq. deg. in size. Note that since the light curve for each rotation cycle consists of only ~ 170 points ($<<$ 3434 patches we wish to reconstruct), a regularization procedure must be employed to permit a unique solution to the light curve inversion.

The goal of LI is to compute a set of patch brightnesses that mimics the appearance of the actual stellar surface as closely as possible. An obstacle to achieving this is that the inversion problem is inherently very sensitive to the presence of noise in the light curve data. This can be understood by noting that the theoretical light curve

of a featureless stellar surface would be a horizontal line, while actual photometry obtained for such a star would exhibit a high-frequency ripple due to noise in the observations. Conversely, the rotational light curve produced by a surface covered with a quasi-uniform distribution of small spots would have nearly equal numbers of spots appearing over the approaching limb and disappearing over the receding limb. The result is a light curve that is nearly flat with a high-frequency ripple superimposed on it. Because the effects of noise and of numerous small spots are very similar, simply finding the set of patch intensities which provides the best fit to the photometry will yield a surface covered by small spots in order to fit the noise.

To avoid noise amplification and to allow for a unique solution for this ill-posed inversion problem, we obtain the patch brightnesses by minimizing the *objective function* (Twomey, 1977; Craig & Brown, 1986)

$$E(\hat{\mathbf{J}}, \mathbf{I}, \lambda, B) = G(\hat{\mathbf{J}}, \mathbf{I}) + \lambda S(\hat{\mathbf{J}}, B). \tag{2.1}$$

Here $\hat{\mathbf{J}}$ represents the set of patch brightnesses on the reconstructed stellar surface as computed by LI, while $\mathbf{I}$ represents the set of observed photometric intensities, i.e. the data light curve. Because the distance to the star and its surface area are not accurately known, no attempt is made to calculate absolute fluxes from the surface patches; all that is desired are the brightnesses of the patches relative to one another. The function $G(\hat{\mathbf{J}}, \mathbf{I})$ expresses the goodness-of-fit of the calculated light curve to the data light curve, such that smaller values of G imply a better fit. The *smoothing function* $S(\hat{\mathbf{J}}, B)$ is defined such that it takes on smaller values for surfaces that are "smoother" in an appropriately defined sense, and in particular is minimized for a featureless surface. Finally, λ is an adjustable Lagrange multiplier called the *tradeoff parameter*, and B is an adjustable parameter called the *bias parameter*. Note that as $\lambda \to 0$, the first term on the right dominates, so that minimizing E is equivalent to

minimizing G, yielding the surface that best fits the light curve data but is dominated by spurious noise artifacts. On the other hand, as $\lambda \to \infty$, the second term dominates, producing a nearly featureless surface that gives a poor fit to the photometry. For intermediate values of λ, we obtain model surfaces that fit the data well, but not so well that the surface is dominated by noise artifacts. This general approach of controlling an ill-conditioned inversion for noise artifacts is known as *regularization*.

The penalty function used in this study is the generalized Tikhonov regularizer of the form

$$S(\hat{J}, B) = \sum_{i=1}^{N} \sum_{j=1}^{M_i} w_i c_{ij} \left(\hat{J}_{ij} - \hat{J}_{\rm avg} \right)^2 , \tag{2.2}$$

here $\hat{J}_{\rm avg}$ is the average value of $\hat{J}_{ij}$ over all the patches on the surface. The coefficient $c_{ij} = 1$ if $J_{ij} < \hat{J}_{\rm avg}$, while $c_{ij} = B$ if $\hat{J}_{ij} \geq \hat{J}_{\rm avg}$, where $B > 1$ is the *bias parameter*. B is introduced so as to bias the solution towards exhibiting dark spots on a background photosphere of nearly uniform brightness by making the penalty for a patch being brighter than average B times larger than for being darker than average by the same amount (see Harmon & Crews (2000) for further discussion of the bias parameter). The w_i are latitude-dependent weighting factors which counter the tendency for spots in the reconstructions to appear at the sub-Earth latitude. This tends to occur because a spot near the sub-Earth point on the stellar surface has a larger projected area than a spot of the same size farther away, so that a smaller spot centered at the sub-Earth latitude will produce the same modulation amplitude in the light curve as a larger one at a different latitude. Since a smaller spot results in a smaller value of the penalty function S, it will be favored by the algorithm. To mitigate this, w_i is made proportional to the difference between the maximum and minimum values of the product of the projected area and the limb darkening for patches in the $i^{\rm th}$ band. Note that when multiplied by the patch specific intensity in the outward direction,

Table 2.1. Rms Deviations between Observed and Reconstructed Light Curves (magnitudes) of KIC 5110407

Angle of Inclination	Mean	Median	Minimum	Maximum	Deviation, σ
30°	0.0020	0.0020	0.0012	0.0038	0.0004
45°	0.0018	0.0017	0.0010	0.0028	0.0003
60°	0.0017	0.0017	0.0010	0.0027	0.0003
75°	0.0016	0.0016	0.0009	0.0026	0.0003

this difference determines the amount of light curve modulation associated with a patch, so patches that because of their latitudes have a lesser ability to modulate the light curve are associated with a smaller penalty for deviating from the average brightness by a given amount.

The general procedure for inverting a light curve using LI is as follows. The input parameters are the estimated goal root-mean-squared (rms) noise σ in the photometry expressed in terms of magnitude differences (see Table 2.1), the estimated spot and photosphere temperatures $T_{\rm spot}$ and $T_{\rm phot}$, and the inclination angle i of the rotation axis to the line of sight. As described in Harmon & Crews (2000), two copies of a root-finding subroutine are used in concert so as to find the values of λ and B such that the rms variation between the light curve of the reconstructed surface and the data light curve is equal to σ, and the ratio of the brightness of the darkest "spot" patch on the surface to the average patch brightness (used as a proxy for the photosphere brightness) is equal to the spot-to-photosphere brightness ratio implied by $T_{\rm spot}$ and $T_{\rm phot}$.

In practice, it is best to invert for a range of assumed values of the photometric noise so as to produce a set of solutions. It is found that the reconstructed surface begins to show very obvious noise artifacts over a small range of assumed noise levels (typically randomly distributed bright and dark patches; see Harmon & Crews, 2000, for more detail). The "effective" noise level is that at which obvious noise artifacts begin to appear. The "best" solution is chosen to be one for which the assumed noise

exceeds the "effective" noise by a small amount to avoid artifacts.

In this study, we assign a photospheric temperature of $T_{\rm phot}$ = 5200 K, with a $\Delta T = T_{\rm phot} - T_{\rm spot}$ = 1000 K (based upon findings of Berdyugina, 2005). We used the logarithmic limb-darkening coefficients for the *Kepler* bandpass ($e = 0.7248$, $f = 0.1941$) reported by Claret & Bloemen (2011, equivalent to the ϵ and δ used in Harmon & Crews (2000)) for a star with $T_{\rm eff}$ = 5250 K, $\log g$ = 4.0, and [Fe/H] = -0.2. We did not interpolate due to uncertainties in the values provided by the *Kepler Input Catalog*. Because the angle of inclination of KIC 5110407 is unknown, we consider four possible angles of inclination: $i = 30°, 45°, 60°$, and $75°$, where i is the angle between the rotation axis and the line of sight. Inversions failed for $i = 15°$.

Before undertaking light curve inversions, we inspected the light curve for evidence of binarity. A power spectrum showed no strong coherent peak from ellipsoidal modulation that would have indicated the presence of a close companion; for this work, we assume KIC 5110407 is a single star or a widely-separated binary. The equatorial rotational velocity, assuming the radius given by Brown et al. (2011) and the period used in this study (see details below), can be estimated as $v \approx 32$ km s^{-1}, which will not significantly distort the shape of the star. Because of this, we assume the star can be modeled as a sphere. We note that $v \sin i$ can fall in the range 16 km s^{-1} $\leq v \sin i \leq$ 31 km s^{-1} for the four angles of inclinations we consider here. A future precise measurement of $v \sin i$ would restrict the allowed range of inclination angles and lead to less ambiguous surface inversions.

Lastly, we adopt a characteristic rotation period of the star estimated from the Fourier transform of its light curve and refined by identifying a stably moving spot in Quarter 5 for $i = 60°$ (i.e. its movement in longitude was roughly constant over time). The approximate rotation period of this spot was assigned to the star, P = 3.4693 days, which is consistent with the value given by Street et al. (2005). With the period assignment made, the reference spot will remain stationary in longitude on the surface

of the star, while spots that do not remain stationary in longitude indicate possible differential rotation.

2.6 Results

A total of 172 single-rotation-cycle light curves with four values of i were inverted with LI. As discussed in the previous section, the rms deviations between observed and reconstructed light curves were chosen to be as low as possible while avoiding noise artifacts in the inversions. Typical final rms deviations are $\sim$1.7 millimag and a detailed record for all angles of inclination can be found in Table 2.1. The rms values for $i = 30^\circ$ are slightly higher than for the other angles of inclination, a possible indication that the true inclination of the source is higher than this value. For an example of light curve fits and the resulting surface for each angle of inclination, see Figure 2.2; additional surfaces are available in the Appendix A. Nine single-rotation-cycle light curves were omitted from our study due to insufficient phase coverage.

Figure 2.3 shows images from a series of 10 rotational cycles that illustrate the quality of the reconstructions. At the beginning of this series, two spots are seen at different latitudes. Over time, the higher-latitude spot is seen to move past the lower-latitude spot. When the spots get close together, the LI method is unable to discern two separate spots; however, by the end of the series we clearly see the original two spots after they separate. The relative motion of spots at different latitudes in this example suggests differential rotation and is indeed consistent with the complete analysis of the next section.

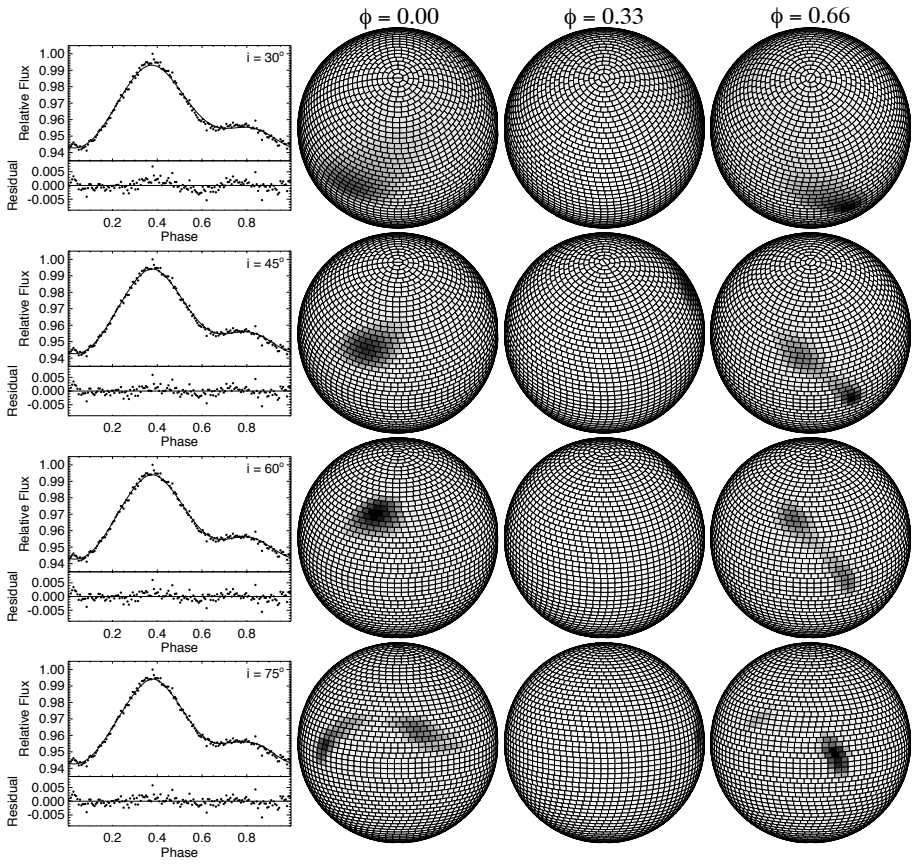

Figure 2.2: Typical light curve chosen to illustrate the variations in the results obtained for different assumed inclinations. The first column compares the observational (diamonds) and reconstructed (line) light curves. Residuals are plotted below the light curves. The next three columns are views of the star at the appropriate inclination at phases 0.00, 0.33, and 0.66. The rows show the results for $i = 30°$, $45°$, $60°$, and $75°$.

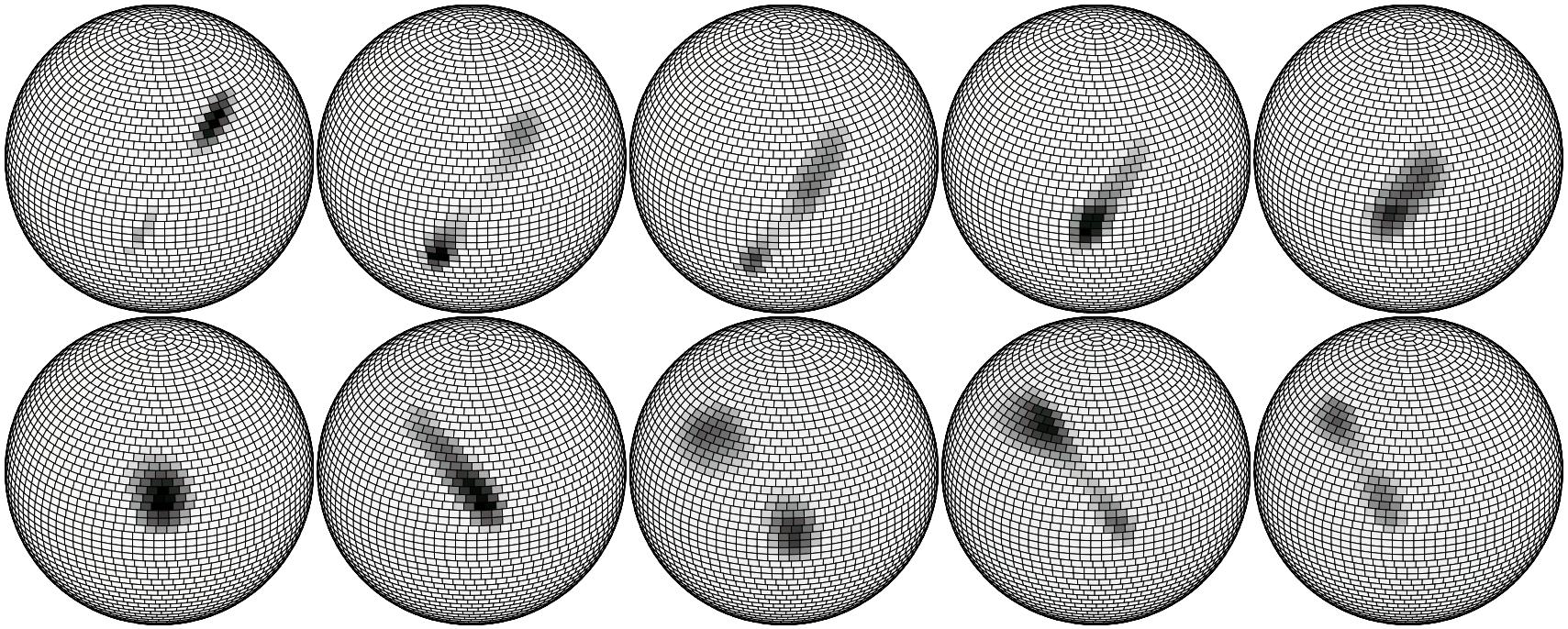

Figure 2.3: Series of sequential reconstructed surfaces that highlight the interaction of spot structures on KIC 5110407. The surfaces are centered on the same latitude and longitude (time increases across the top row from left to right then across the bottom row). The sequential reconstructed surfaces begin with Barycentric Julian Date (BJD) 2455124.43. In this case, a higher-latitude spot "passes" above a lower-latitude spot. When the spots are at similar longitudes, they cannot be resolved, but as time progresses, the spots again move apart.

2.6.1 Spot Properties

In order to quantify spot properties, we developed a method for identifying individual spots based on the surface maps. Note that a single large spot is likely comprised of a complex of smaller spots in one region, and we use the terms "spot" or "spot group" synonymously. For each spot group visually identified in the surface map, the latitude and longitude were determined by finding the centroid of each spot, defined by drawing a circle on the reconstructed stellar surface enclosing the spot and finding the "center of mass" of the patches therein; the "mass" of a patch was defined as the difference between its intensity and the average surface intensity. With a list of spot positions for every rotational cycle, we can carry out analysis of spot lifetimes and measure differential rotation. The average spot lifetime was thirteen rotation cycles ($\approx$ 45 days) across all angles of inclination. The longest-lived spot structure was discernible for more than 42 rotation cycles ($>$ 146 days; $i = 30°$). The spots of KIC 5110407 live on a shorter timescale than that predicted by Strassmeier et al. (1994) for a star exhibiting the observed differential rotation rate (see below).

One basic property of active stars we would like to study is the time evolution of the spot coverage. To determine the model-dependent spot coverage, we defined a patch of the reconstructed surface as part of a spot if the patch is darker than 95% of the average patch intensity. In general, the spots seen in the image reconstructions have sharply defined boundaries making our criterion both reasonable and robust (see Harmon & Crews, 2000). Our estimate of the percentage of the surface covered in spots is dependent upon the assumed angle of inclination of the rotation axis. For a lower inclination, the projected area of the spots tends to vary less over a rotation cycle, requiring larger spots to produce a given amplitude of the brightness variations in the light curve. Across all of the angles of inclinations we used, there is a minimum of approximately 1% of the surface covered in spots (see Figure 2.4). At no point in our observations is there a rotation cycle when KIC 5110407 is completely free of

spots. We see the spot coverage vary on timescales of a few rotation periods as the one or two dominant spots change intensities. Note that our spot coverage estimates represent lower limits because there may be isolated small spots below our detection threshold or polar spots. Since spots located near the poles do not introduce rotational modulation and are missed in our analysis, the LI algorithm as used here does not account for secular changes in the star's brightness due to polar spots that might be seen as long-term flux variations.

Next, we analyze the relative motions of the observed spots based on the inferred latitudes and longitudes. In this analysis, we included only the spots that satisfied the following criteria: (1) the spot must be present on the surface for six or more rotation periods and (2) the spot must show no evidence of interaction with another spot (for example, an instance of two spots combining into one spot is not accepted, but two spots moving by each other is accepted). In order to weight measurements of each spot by longevity and to account for possible latitudinal drift, each spot lifetime was divided into sets of surface inversions consisting of six sequential rotational periods (with the exception of the last set of rotations extending up to eleven periods). The longitudes of these spots are then plotted versus time, appearing in Figure 2.5. In this plot, a positive slope indicates a shorter rotation period compared to the reference period 3.4693 days; a negative slope indicates a longer rotation period. These slopes are suggestive of spots at lower and higher latitudes than the reference spot, respectively; however, there are spots that deviate from this overall pattern, which likely reflects uncertainties in our method rather than renegade spot behavior. Armed with a rotational period for each spot, we can search for trends as a function of spot latitude. Broken down by assumed inclination angle, Figure 2.6 shows the observed rotational rate versus inferred latitude location for each spot. For inversions based on a single observing bandpass, such as those presented here, there is heightened uncertainty in

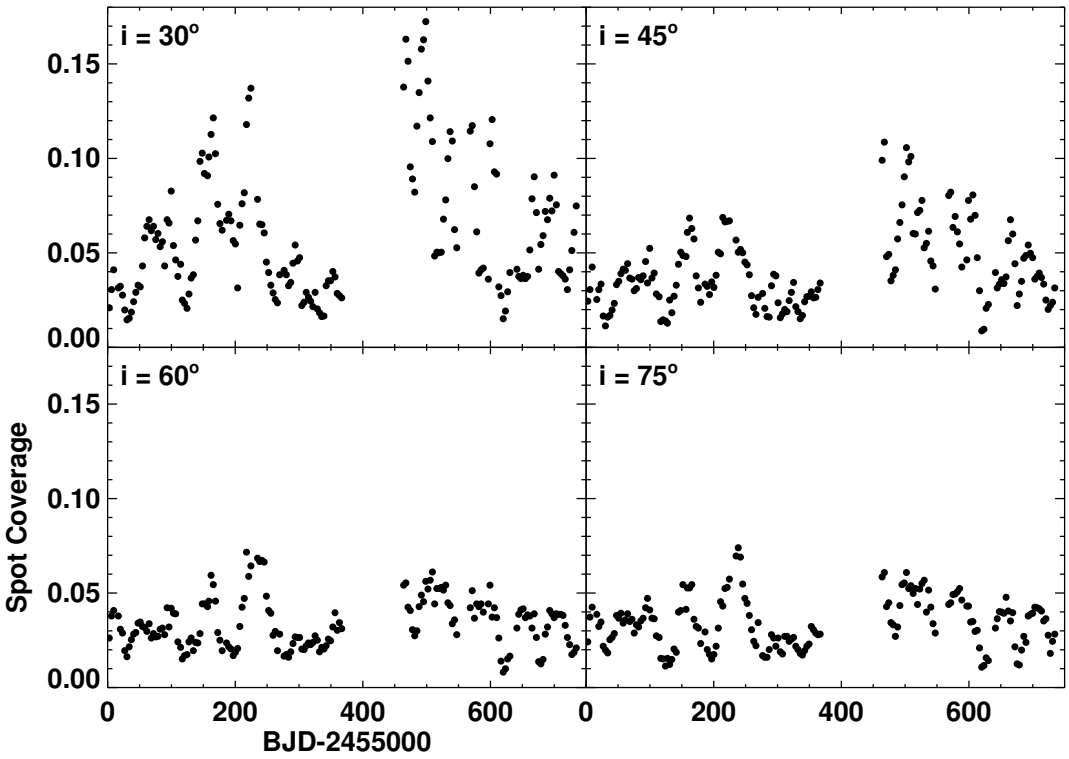

Figure 2.4: Time dependence of the fraction of the stellar surface area covered by spots is presented with each panel representing a different angle of inclination. This assumes that there are no polar spots or spots on the hidden rotation pole never visible from *Kepler*. A minimum spot coverage of approximately 1% occurs for all angles of inclination. The highest spot coverage occurs for $i = 30°$, which also has the poorest agreement between observed and reconstructed light curves (see Table 2.1). The spot coverages for $i = 60°$ and $i = 75°$ are nearly in agreement. The abscissa is presented as a modified Barycentric Julian Date.

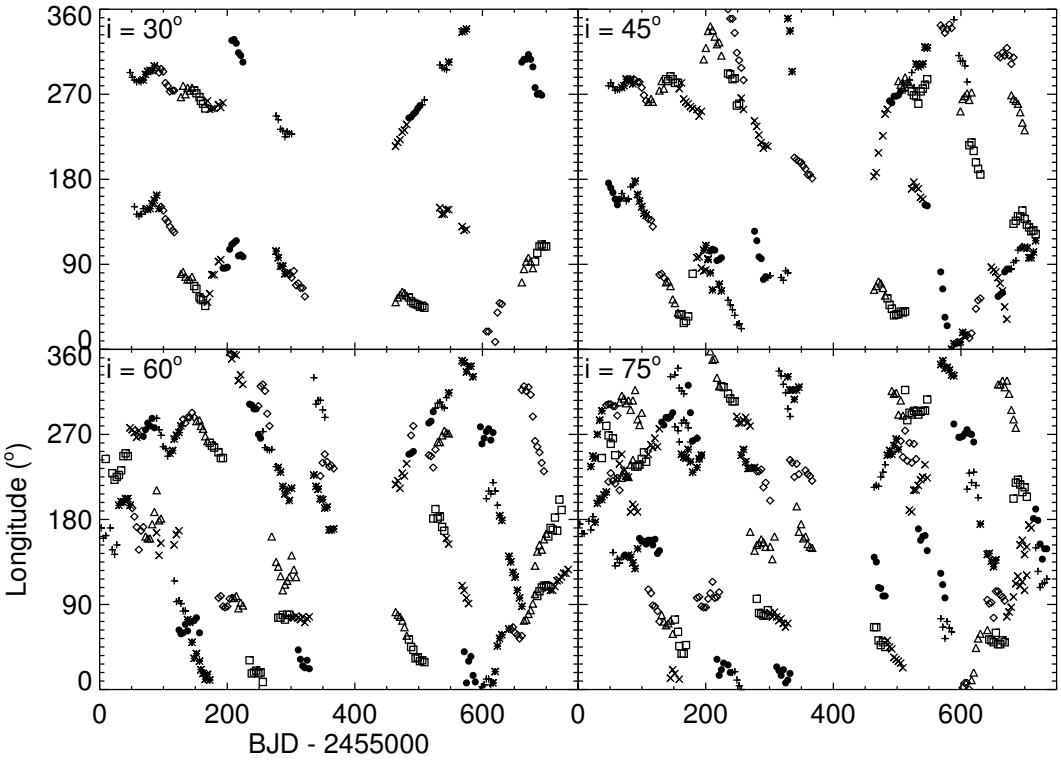

Figure 2.5: Longitude (in degrees) for the spots of KIC 5110407 are plotted versus time. The plot shows systemic drifts and lifetimes for each spot presented. Each panel represents a different angle of inclination, and each symbol represents a different spot. The same symbol separated by a temporal gap applies to a different spot. The abscissa is presented as a modified Barycentric Julian Date.

the absolute latitude of a given spot.[2] However, as shown by Roettenbacher et al. (2011), the reconstructions do reliably preserve relative latitudes, i.e. the difference in latitude between two spots is more accurate than the mean latitude. With this caveat in mind, we proceed to estimate the level of differential rotation observed in KIC 5110407.

[2]Multi-color observations allow better latitude determination by taking advantage of the known wavelength-dependence of limb-darkening effects (see extensive discussion and simulations by Harmon & Crews, 2000).

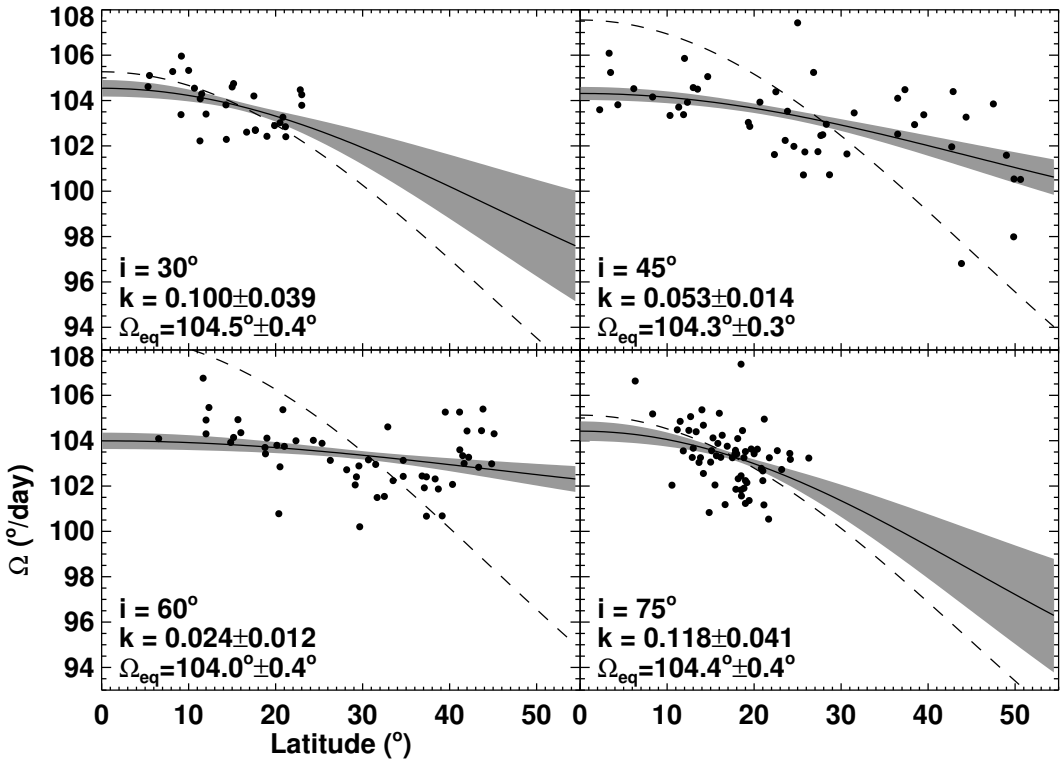

Figure 2.6: Spot rotation rates in degrees of longitude per day for KIC 5110407 (from Figure 2.5) are plotted against the average latitude of the spot over its lifetime. Each panel represents a different angle of inclination. The differential rotation law from Henry et al. (1995) is applied to each set of data. With a solid line, we plotted the mean fit to the differential rotation law $\Omega(\theta) = \Omega_{\rm eq}(1 - k\sin^2\theta)$, where k is the differential rotation parameter as described in the text (the grey regions represent 1-σ errors on our fit). The differential rotation parameter for the Sun is $k = 0.19$; the mean fit with this parameter is plotted in each panel with a dashed line. Applying this solar model overestimates the amount of observed differential rotation.

Henry et al. (1995) presented the relation for differential rotation of

$$\Omega(\theta) = \Omega_{\rm eq}(1 - k\sin^2\theta), \tag{2.3}$$

where θ is the spot latitude, Ω is the stellar rotational angular frequency, $\Omega_{\rm eq}$ is the stellar rotational angular frequency at the equator, and k is the differential rotation coefficient. Henry et al. (1995) give a solar value of $k = 0.19$ representing differential rotation from the equator to mid-latitudes where most sunspots are observed.

We applied Equation 2.3 to the data from each of the angles of inclination as shown in Figure 2.6, using bootstrap sampling to estimate uncertainties. Not surprisingly, we found that the differential rotation parameter, k, depends on the assumed angle of inclination. An angle of inclination $i = 75^\circ$ showed the strongest differential rotation with a differential rotation parameter of $k = 0.118 \pm 0.041$, while $i = 60^\circ$ showed the weakest differential rotation $k = 0.024 \pm 0.012$. For each inclination, we also fit a model using the scaled solar value of k and confirmed that it overestimates the amount of differential rotation, as shown with dashed lines in Figure 2.6. No matter which inclination we consider, we find a level of differential rotation consistently smaller than observed on the Sun. We will discuss this further in Section 2.7.

2.6.2 Flares

In addition to analyzing the spots, we found seventeen stellar flares during our observing period that increased the stellar flux by more than 1%. While these flares had to be removed before inverting the light curves, we compiled their statistics in Table 2.2. For each of these flares, the associated *Kepler* target pixel file was examined for background source contamination. The flare events occur on the same pixels as the stellar light curve, leading to the assumption that the flares are associated with the activity on KIC 5110407 and not due to instrument transients or a nearby source.

Table 2.2. Timing and Strength of Flares of KIC 5110407

Barycentric Julian Date of Flare (BJD - 2455000)	Peak Flare Intensity above Stellar Intensity (in percent)	Phase of Flare	Phase of Light Curve Minimum	Phase of Light Curve Maximum
35.03	2.13	0.365	0.618	0.984
62.32	1.10	0.234	0.517	0.122
87.65	1.66	0.537	0.572	0.131
186.96	1.88	0.162	0.567	0.243
215.93	3.04	0.507	0.035	0.624
235.38	1.55	0.119	0.207	0.732
235.81	17.94	0.243	0.207	0.732
277.47	1.32	0.247	0.629	0.276
280.56	1.28	0.142	0.701	0.265
303.72	1.98	0.815	0.936	0.385
311.66	9.22	0.107	0.036	0.590
324.14	1.28	0.699	0.075	0.747
338.55	1.25	0.852	0.357	0.982
349.39	5.18	0.980	0.644	0.090
466.32	1.38	0.682	0.717	0.381
485.61	2.29	0.241	0.071	0.777
518.15	1.19	0.623	0.447	0.900

Figure 2.7 shows the largest flares (17.9% and 9.2%, respectively) observed along with the corresponding surface maps at the time of the flare. In both cases, the largest spot features are oriented toward *Kepler*.

Based on the fact that the brightest flares occurred when the strong starspots faced the observer, we inspected the full list of flares for further evidence of a correlation between flare timing and orientation of the dominant spot group. We compared spot location to flare timing (see Table 2.2, also for the time of minimum and maximum light curve intensity). The median difference in rotation phase between the flare event and the nearest minimum of the light curve was 91°, consistent with the expectation of 90° for uncorrelated events. Indeed, a Kolmogorov-Smirnov test gave a 96% probability that the relative timing between these events was drawn from a uniform distribution. This lack of correlation is consistent with the flare study of Hunt-Walker et al. (2012). For Quarters 2-9, we conclude most flares do not originate in the strongest spot group but rather come from small spot structures or polar spots that are not detected by our LI method. More data will be needed to see if the strongest flares (>5%) tend to come from the strongest spot group, an attractive

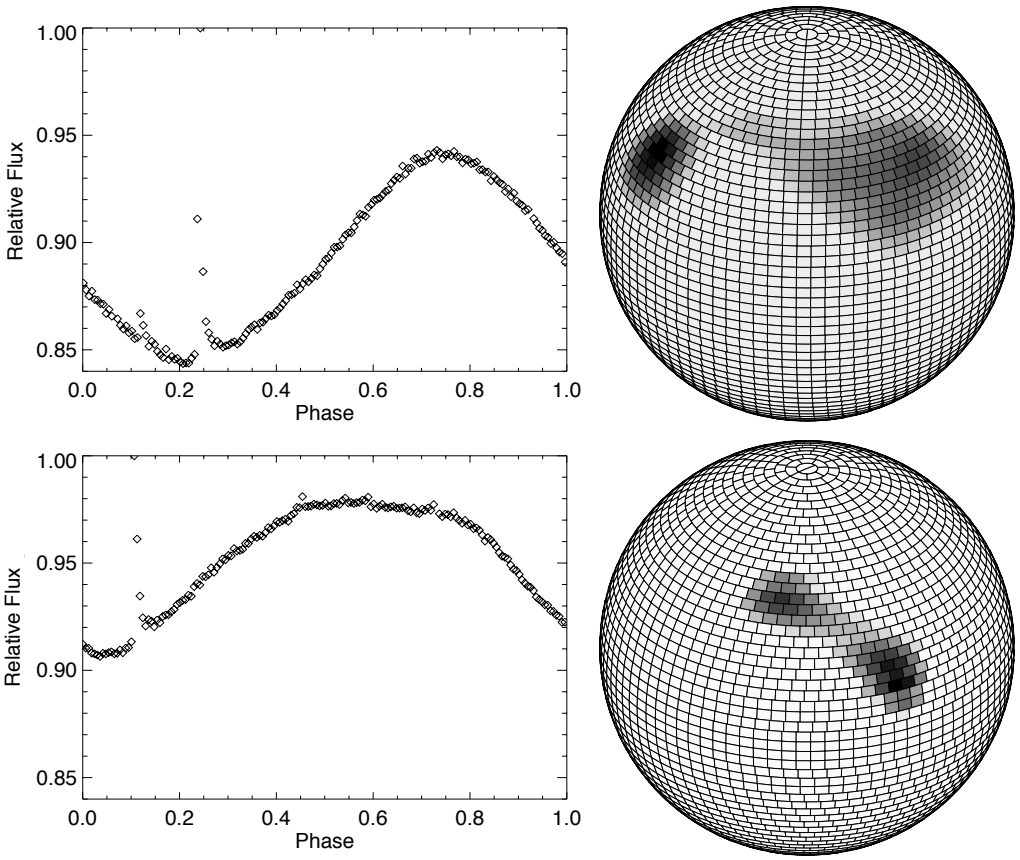

Figure 2.7: Light curves of largest flares in the observed in this data set are presented with the appearance of the surface (for $i = 60°$) at the time of the flare. For both cases, the large spot structure was facing *Kepler*. Although this is the case for the two strongest flares, we do not see correlation between spot location and flare timing when considering the full set of seventeen flares.

hypothesis since the strong magnetic fields needed for the strongest flare may only be present in most enhanced regions of field concentration.

We understand that this analysis is simple and neglects the detailed geometry of active regions, such as the relative location of plages and faculae with respect to cool spots. Furthermore, inclination effects will tend to wash out correlations if a cool spot is always viewable on the surface. Perhaps with a larger dataset, these effects can be modeled and an improved analysis can be pursued in the future.

Lastly, we note an unusual concentration of flares in Quarters 4 and 5 and an usually quiet period of 200 days without any flares during Quarters 7-9. We counted the number of flares greater than 1% of mean flux to be 3, 0, 3, 7, 3, 0, and 0 flares in Quarters 2, 3, 4, 5, 7, 8, and 9, respectively. If we restrict to only the three brightest flares $> 5\%$, one occurred in Q4 and two in Q5, with zero strong flares occurring in the other quarters. The high-quality *Kepler* light curves offer the first possibility to link starspot evolution with flaring statistics in the context of a long-term stellar magnetic cycle. Given the relatively small number of flares detected to date, we postpone any firm conclusions until a longer temporal baseline of observations is available.

2.6.3 Flares in the Full *Kepler* Light Curve

For follow-up using the complete *Kepler* light curve of KIC 5110407, we measured the phase difference between the occurrence of the flare and the light curve minimum. Figure 2.8 shows the strength of each flare (in percent flux above the stellar flux) plotted against the phase difference between the minimum of the light curve and the time of the flare. The small flares ($< 5\%$) show no correlation in their timing. These flares could be associated with the spots observed on KIC 5110407, unresolved spots below our resolution, or the spotless photosphere. The strongest flares are correlated with the position of the largest starspots facing *Kepler*.

In Figure 2.9, we plot the number of flares in each *Kepler* quarter. The error bars

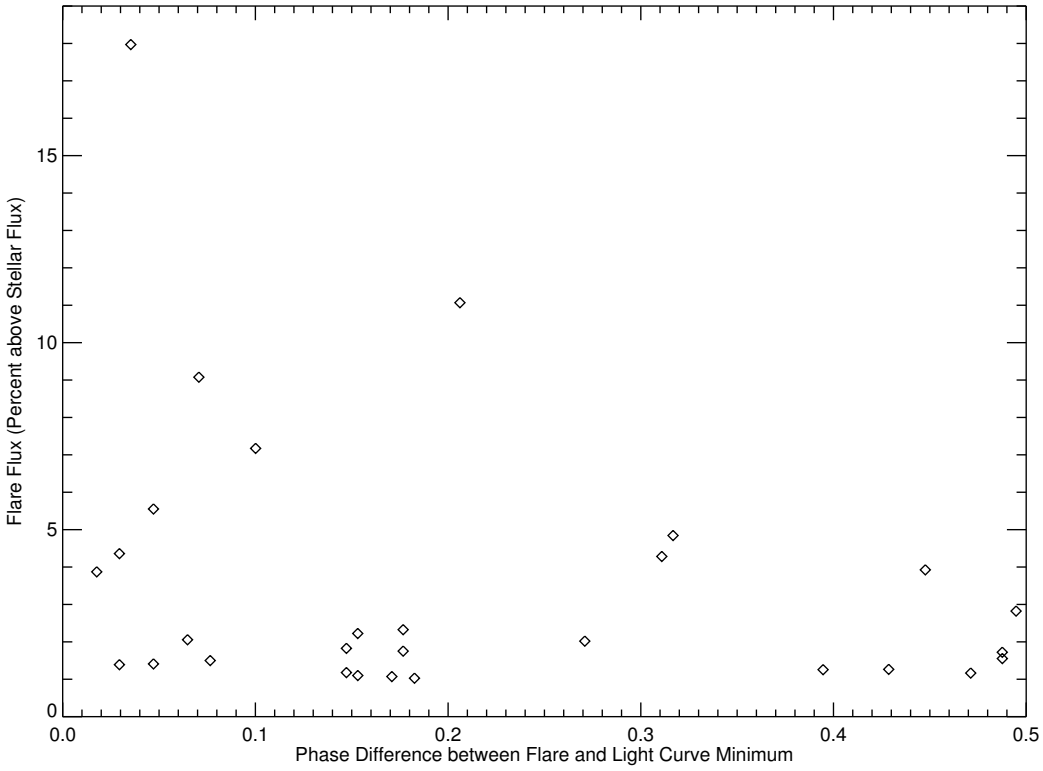

Figure 2.8: Flare strength plotted against the phase difference between the minimum of the light curve and the peak of the flare. The small flares (percent of flux above the stellar flux $< 5\%$) show no correlation to the presence of large spot structures. The strongest flares are correlated with the largest starspots.

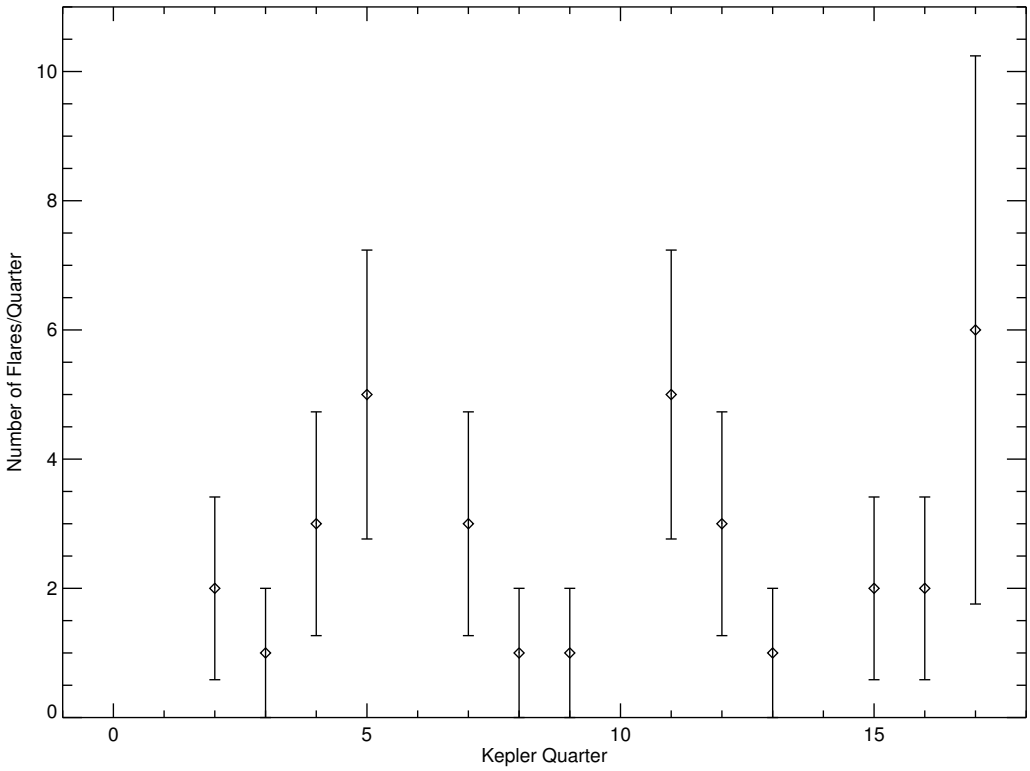

Figure 2.9: Distribution of flares of KIC 5110407 during each *Kepler* quarter, with Poisson errors. The quarters with no detections are all quarters for which *Kepler* did not observe KIC 5110407. A potential activity cycle can be noted, but the failure of *Kepler* in Q17 prohibits the confirmation of a cycle.

account only for Poisson statistics ($\sigma_{N_{\rm flare}} = \sqrt{N}$). The quarters with no flares are all quarters for which KIC 5110407 was not observed (in the cases of Q6, 10, and 14, the star fell on a detector that previously stopped functioning). If the enhanced activity seen in Q5 and 11 is an indicator of the presence of a magnetic activity cycle, we expected to see another peak in Q17. Unfortunately, in Q17, *Kepler* experienced a failure that ended data-taking operations after one-third of the quarter. In what exists of Q17 data, two flares were detected. Here we extrapolate the flare rate for the entire quarter. Although the rate of flares in Q17 is promising, we cannot verify the existence of an activity cycle in the flares of KIC 5110407.

2.7 Summary and Conclusions

The unique combination of high-precision photometry, 30-minute cadence, and nearly continuous temporal coverage makes the *Kepler* satellite a critical resource for stellar astrophysics including the study of magnetic activity. To date, the variability of stars in the *Kepler* light curves has begun to be systematically characterized (e.g., Basri et al., 2011; Harrison et al., 2012, through operational Quarters 2 and 5, respectively). While these works take a bird's eye view of the *Kepler* dataset, only a few papers have focused on individual active stars for detailed studies of spot evolution in the way that we have here.

Frasca et al. (2011) recently analyzed the *Kepler* light curve of a young solar analogue, KIC 8429280, coupled with better stellar parameters determined through ground-based spectroscopy. The authors used an analytic model of at least seven long-lived spots to fit the light curves for each star. The spot properties were used to quantify the level of differential rotation ($k = 0.05$). To further spot studies, Fröhlich et al. (2012) applied the same analytic techniques to two other young solar analogues (KIC 7985370 and KIC 7765135; $k = 0.07$ for both stars). Using a technique similar to ours, Savanov (2011a) showed evidence of spot evolution in two *Kepler* planet-candidate stars, KOI 877 and KOI 896. Savanov (2011b) found a potential correlation between minima in light curve amplitude and a switch in active longitudes of KIC 8429280, the same target as Frasca et al. (2011, with the same initial *Kepler* data set). The spots of this *Kepler* target moved and evolved rather significantly, including in relative size, over the length of the observation (138 days). A change in the most active longitude occurs when one spot's effect on the light curve outgrows the other, which they conclude occurred three times during their data set. Additionally, Savanov (2011b) conclude that KIC 8429280 exhibits spot motions too small to quantify as differential rotation. Savanov & Dmitrienko (2011, 2012) discussed fully-convective spotted M dwarf *Kepler* stars. There were minor motions

indicating differential rotation on only one of their targets (KIC 2164791; Savanov & Dmitrienko, 2012). For their efforts with KIC 2164791, with an unknown i, they modeled their surfaces with $i = 30°$ and $i = 60°$. For their work, their target, the surface was dominated by a single spot and changes in inclination did not impact their results, aside from spot coverage.

Numerical simulations of young solar analogues should make predictions that can be tested through Kepler studies of active stars. In Hall (1991), the author used the photometric variability of 277 potentially spotted stars to show that k decreases as stellar rotation period decreases. Recently, Hotta & Yokoyama (2011) presented a theoretical study finding that stars with angular velocity greater than the Sun should exhibit weaker differential rotation than the Sun. In a different recent theoretical study, Küker et al. (2011) increased the rotation rate of the Sun to a period of 1.3 days to model a young solar analog. Their new period changes the k parameter of the Sun to 0.02. In fact, we report here weaker differential rotation in KIC 5110407 than in the Sun, in line with the conclusions of Hotta & Yokoyama (2011) that differential rotation limits to the Taylor-Proudman state for solar-type stars with rotational periods of a few days.

In conclusion, KIC 5110407 is an active, rapidly-rotating, K-type star in the *Kepler* field. Using a non-linear light curve inversion algorithm, we presented evidence of spot evolution and differential rotation by tracing the motions of spots over time. We found a level of differential rotation consistent with some recent mean-field theory that predicts stars with rapid rotation should have weaker differential rotation than the Sun (Hotta & Yokoyama, 2011). We also showed evolution in spot coverage and flares, which with more data could be used to determine an activity cycle. The flares of KIC 5110407 reveal no evidence of correlation between their timing and vicinity to the dominant spot group, except perhaps for the brightest flares.

The diverse stellar population in the *Kepler* field lends itself to studies of active

stars, providing insight into the fundamental impact of magnetic fields in stellar evolution. Our analysis here serves as a test of using the LI method in analyzing the magnetic activity of a spotted star with *Kepler* photometry. When applied to a larger sample of spotted stars over a longer span of time, LI will reveal key features of the stellar dynamo for stars over a range of mass, age, and rotation rates.

CHAPTER III

Imaging Starspots of *Kepler* Object of Interest KOI-1003 with Light-curve Inversion

3.1 Preface

This chapter is intended for publication with collaborators Stephen R. Kane, John D. Monnier, and Robert O. Harmon. In addition to the work that appears here, an analysis of the nature of the companion will be included when the work is submitted for publication. A section appears at the end of this chapter describing that work.

For my part in this project, I obtained the *Kepler* light curves and removed the cotrending basis vectors to prepare the data for these works. I removed the flares from the light curve and prepared the individual rotation periods for the application of Light-curve Inversion (LI). I applied LI to each light curve for a variety of inclination angles and determined the best rms value for each. I determined the location and size of each starspot, analyzing spot coverage and evolution. I am working on determining the orbital parameters of the system derived from averaged and isolated eclipses. I created all of the figures (except 3.4 and 3.5) and tables (except 3.2) for these works, as well as wrote the majority of the paper (with particular assistance from collaborators for the portion on target disposition and periodic signatures).

3.2 Abstract

Using the high-precision photometry from the *Kepler* mission, thousands of systems hosting stellar and planetary companions have been detected. The disposition of the companion is not always straightforward and can be contaminated by systematic and stellar influences on the light curves. We perform a detailed analysis of the eclipsing *Kepler* system KOI-1003 ($P_{\rm orb} = 8.361$ days) to better determine the type of companion. Additionally, we map the star's spotted surface by inverting the star's long cadence *Kepler* light curve spanning Q2-17 ($P_{\rm rot} = 8.231$ days, 164 rotations). The signatures of two strong starspots persist on the stellar surface and affect the depth of the eclipses.

3.3 Introduction

The high-precision, nearly-continuous photometry obtained by the *Kepler* satellite overcame the limitations of ground-based photometry to allow for unprecedented analyses of many stellar systems. Working toward the primary goal of the mission, the number of known and candidate exoplanets has dramatically increased through the analysis of *Kepler* photometry (e.g., Borucki et al., 2011a,b; Batalha et al., 2013), but the unprecedented photometry has also provided a wealth of information for stellar astrophysics, including asteroseismology, stellar evolution, and stellar activity.

For low-mass stars, starspots are the result of magnetic fields stifling the convection in the outer layers (e.g., Strassmeier, 2009). Using *Kepler* photometry, starspots have been studied with spot modeling (e.g., Frasca et al., 2011; Fröhlich et al., 2012) and light-curve inversion (e.g., Savanov & Dmitrienko, 2011, and Chapter II) techniques to produce surface maps of evolving spot structures.

In the *Kepler* Input Catalog, a plethora of stars exhibit variable light curves (Basri et al., 2010, 2011, 2013), many of which are likely the result of starspots' rotational

modulation. KOI-1003 (KIC 2438502, 2MASS J19211869+3743362) is one such star with rapidly-changing features attributed to starspot evolution. In addition to the variable spot signature, KOI-1003 exhibits primary and secondary eclipses. Past studies of the old ($\sim$ 8 Gyr; Chaboyer et al., 1999) open cluster NGC 6791 included KOI-1003 as a member with a photometric period refined to 8.3141 days from ground-based photometry (Mochejska et al., 2002, 2005) but did not establish the system as eclipsing.

In Section 3.4, we present the *Kepler* observations of KOI-1003. In Section 3.5, we briefly discuss the stellar parameters and disposition of the target. In Section 3.6, we discuss the periodic signatures in the light curve. We discuss the spot models and persistent spots in Section 3.7. We conclude in Section 3.8 with a discussion of our findings. In Section 3.9 we discuss the next steps and preliminary results of a detailed analysis of the eclipses of KOI-1003. We include Appendix B of surface reconstructions of all 164 epochs analyzed.

3.4 Observations

The primary star of KOI-1003 was observed by the *Kepler* space telescope (Borucki et al., 2010; Koch et al., 2010) nearly continuously in *Kepler* Quarters 2−17 as a target of the exoplanet and Guest Observer programs.

For the long cadence light curve, we removed cotrending basis vectors (CBVs) from the *Kepler* simple aperture photometry using the *kepcotrend* tool of the PyKE software package (Still & Barclay, 2012). The CBVs used depended upon the quarter and are found in Table 3.1 (see also Figures 3.1 and 3.2). After removing the systematic effects, the remaining activity is assumed to be the effects of the eclipse, white-light flares, and starspots.

For the complete CBV-removed *Kepler* light curve (Q2 − 17) we stitch the light curves together by a simple median-division. We folded the data over the orbital

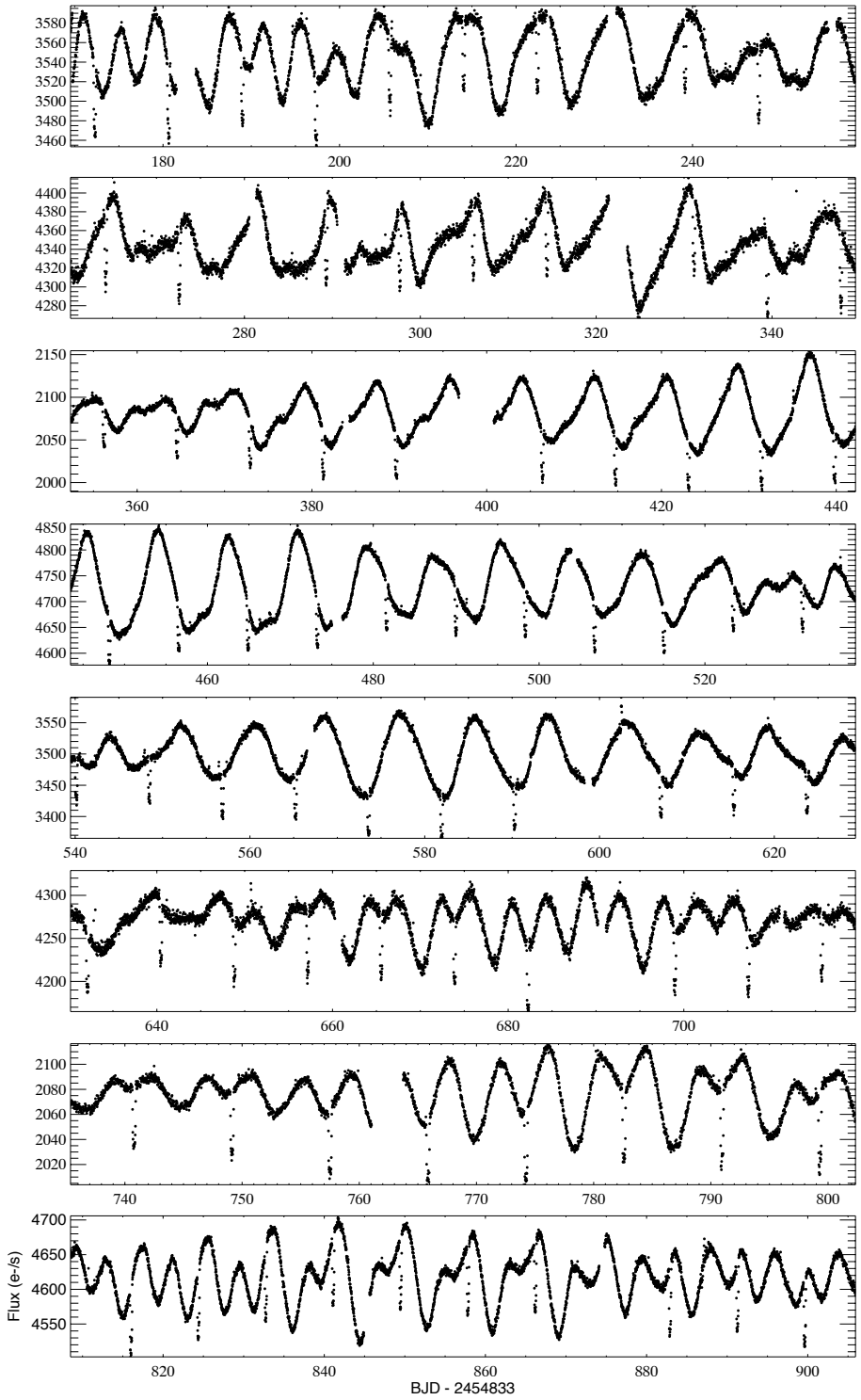

Figure 3.1: Light curves of KOI-1003 for Q2−9 with CBVs removed (top panel is Q2 with the quarter increasing down the page). Each point is a single long cadence data point. The panels are scaled to each quarter. For more details, see Section 3.4.

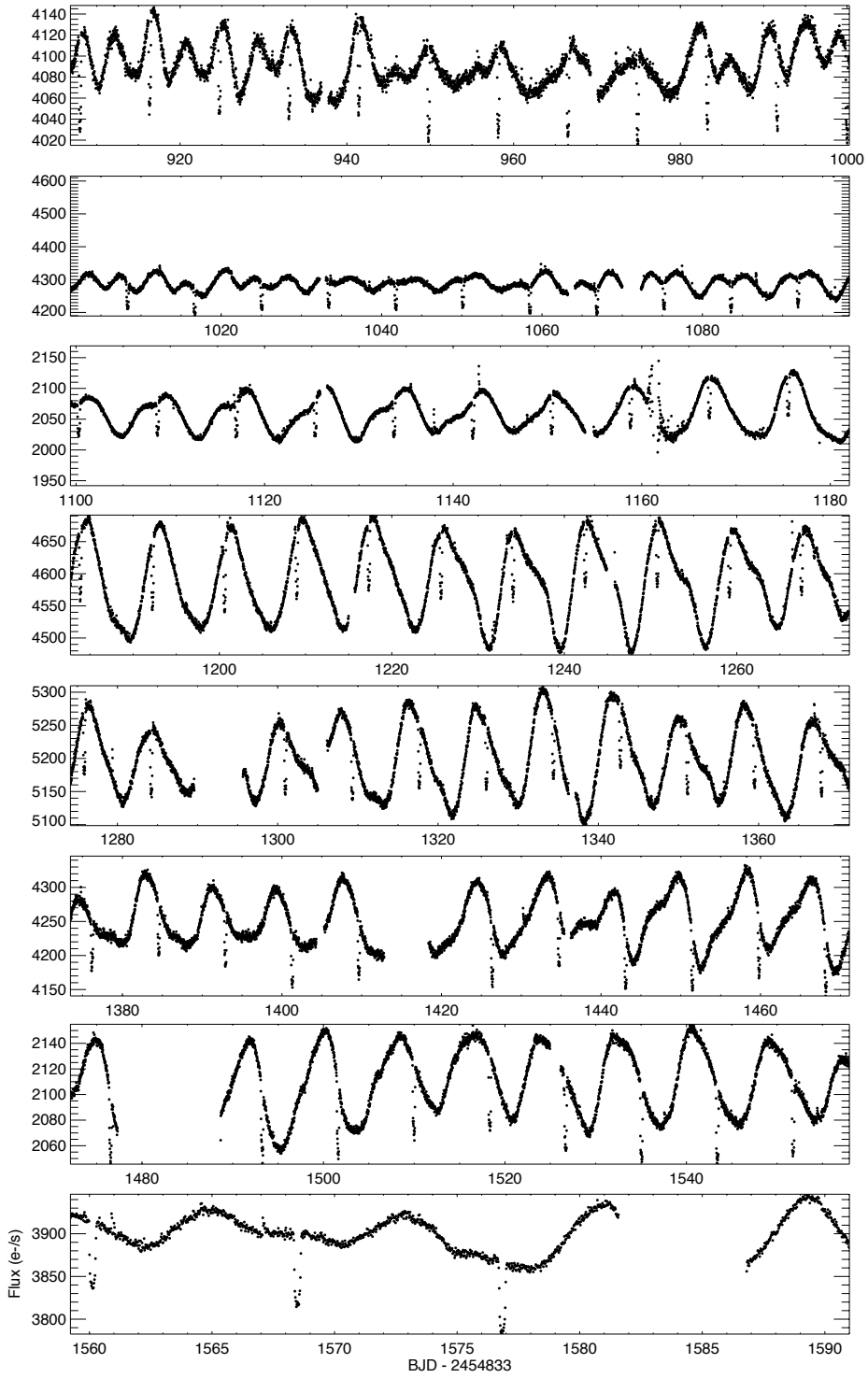

Figure 3.2: Light curves of KOI-1003 for Q10−17 with CBVs removed (top panel is Q10 with the quarter increasing down the page). The plots are as in Figure 3.1.

Table 3.1. CBVs Applied to KOI-1003

Quarter Number	Number of CBVs Used
2	5
3	3
4	2
5	3
6	3
7	3
8	2
9	3
10	2
11	2
12	2
13	2
14	3
15	2
16	3
17	2

period ($P_{\rm orb} = 8.360613 \pm 0.000003$ days, $T = 172.2652 \pm 0.0003$, where T is the transit epoch with BJD -2454833) averaging within 150 phase bins (see Figure 3.3). The large-amplitude quasi-sinusoidal modulation is likely due to starspots consistently appearing at a similar longitude, a so-called "active longitude".

The prominent eclipse that triggered *Kepler* Object of Interest classification of the system is located at phase 0.00. The secondary eclipse is located at phase 0.57. Because this eclipse does not occur exactly half of an orbit from the primary eclipse, the orbit must be eccentric. We estimate the system's eccentricity to be $e \sim 0.11$.

3.5 Stellar Parameters and Disposition of System

KOI-1003 is listed in the *Kepler* Input Catalog as an early K-type star with temperature $T_{\rm eff} \sim 5200$ K, $\log g \sim 4.5$, and metallicity [Fe/H] ~ -0.1 (Brown et al., 2011). Mochejska et al. (2002) name KOI-1003 as a member of NGC 6791 (labeling the star as NGC 6791 KR V54). KOI-1003 is located outside of the core of the cluster and is identified as a member of the cluster due to proximity as velocities to confirm membership have not been obtained.

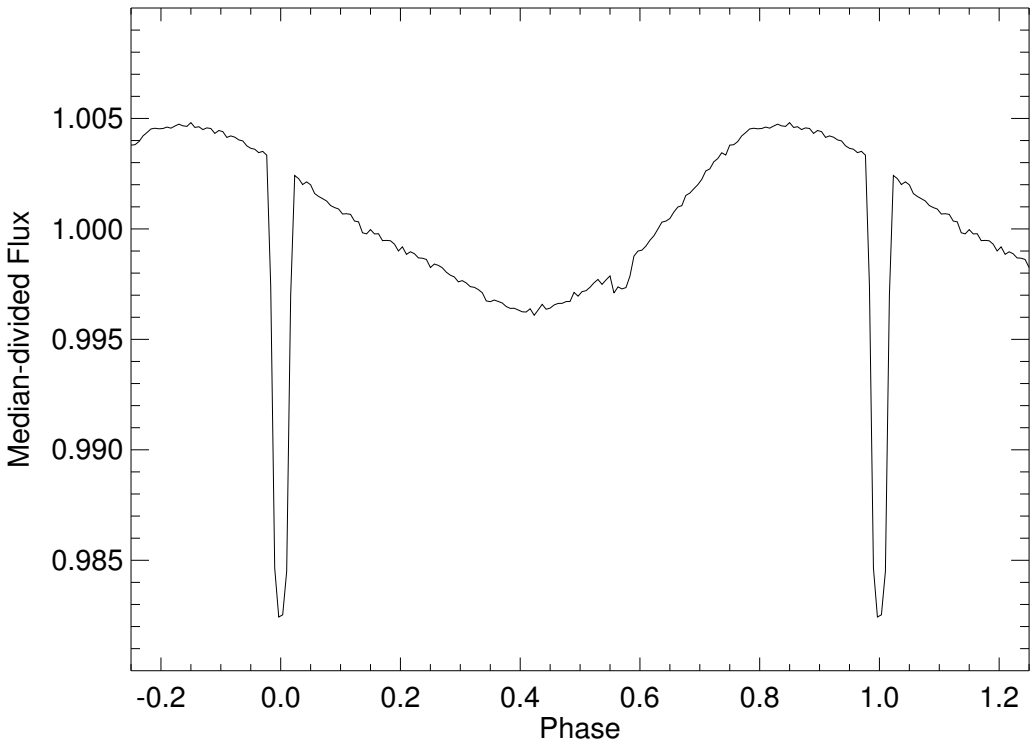

Figure 3.3: Folded and binned light curves of KOI-1003 for the *Kepler* passband. Each data point is an average of data points falling in 150 evenly-spaced bins from a folded light curve using the data from the full *Kepler* light curve (Q2-17). A primary eclipse is observed at phase 0.00 with a secondary eclipse at phase 0.57.

3.5.1 Disposition of KOI-1003

The disposition of KOI-1003 has changed several times over the course of *Kepler* observations. In Borucki et al. (2011b), the star was first listed as a *Kepler* candidate in the Q0−2 data release. The object retained a disposition of "candidate" in the Q1−6 data release (Batalha et al., 2013), but Burke et al. (2014) changed the disposition of the object to "not dispositioned." According to the NASA Exoplanet Archive[1], the "cumulative" *Kepler* data release modified the disposition to "false positive" and the subsequent Q1−16 data release changed the disposition back to "not dispositioned."

The Q1−16 Data Validation Report (DVR) for this system[2] indicates that there are two major causes of the disposition discrepancies: the presence of a secondary eclipse and an apparent offset of the PSF centroid compared with out-of-transit observations. These centroid offsets are generally inside the 3σ radius of confusion for the weighted mean offset, with the exception of quarters Q5, Q9, and Q13. The *Kepler* spacecraft rotates 90° every 90 days, completing an entire rotation at each of these quarters with centroid offsets, which results in the target star falling on the same pixels of the same detector. Examination of the pixel mask used for these quarters shows that there are no detected nearby stars that are causing the significant centroid offsets described in the DVR. However, the fit location of the Pixel Response Function (PRF) always falls in the same pixel for these anomalous quarters (Column 149, Row 925, Module 10, Channel 29). This pixel is not listed in the pre-launch bad pixel map (Douglas Caldwell, private communication), however this list is known to be incomplete.

The presence of nearby, unresolved stars can often be an additional source of confusion for *Kepler* due to the relatively large pixel size ($3.98'' \times 3.98''$). As such, high

[1] `http://exoplanetarchive.ipac.caltech.edu/`

[2] `exoplanetarchive.ipac.caltech.edu//data/KeplerData/002/002438/002438502/dv/kplr002438502-20130815195353_dvr.pdf`

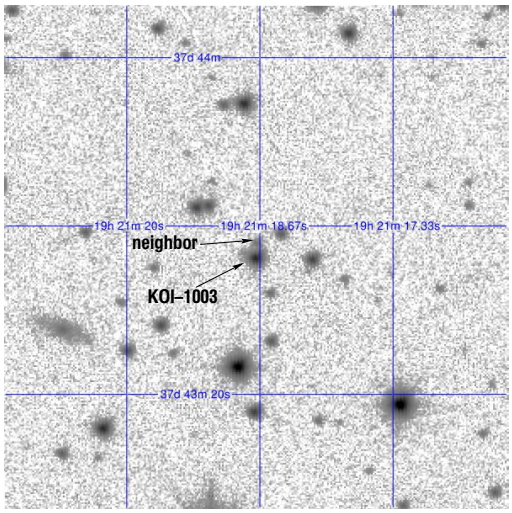

Figure 3.4: J-band UKIRT image of the KOI-1003 field. The star KOI-1003 is labeled in the center of the frame. A potential source of contamination is the neighboring star directly above KOI-1003.

spatial resolution of the field surrounding *Kepler* candidates forms a major component of *Kepler* follow-up activities (e.g., Adams et al., 2012, 2013). We investigated the possibility of contamination from close stellar neighbors using publicly available J-band images from the United Kingdom Infrared Telescope (UKIRT) survey[3]. Figure 3.4 shows a $1' \times 1'$ field centered on the host star KOI-1003 ($J = 14.68$). Slightly above KOI-1003 is a faint neighboring star, which falls within the same *Kepler* photometric aperture. Simple aperture photometry of the stars shows that the flux received by the neighboring star is $\sim 2\%$ of that received by KOI-1003. Thus the neighboring star has a negligible effect on the subsequent analysis.

3.6 Periodic Signatures

To determine the significant periodic signatures present in the KOI-1003 time series photometry we used a weighted Lomb-Scargle (L-S) Fourier analysis, similar to that described by Kane et al. (2007). To stitch the individual quarter light curves together, we divide the median of each quarter after the CBVs have been removed

[3]`http://www.jach.hawaii.edu/UKIRT/`

Table 3.2. Most significant periodogram peaks for KOI-1003

Period (days)	Fourier Power
8.300704	11840.6
8.23101044	8094.8
8.49922562	4095.7
8.69150448	3138.0
8.37158775	2844.8
8.42367744	2748.9
8.12051201	1820.9
8.57097054	1571.7
7.95241308	1567.1
8.6151247	1539.7

(see Section 3.4).

The resulting periodogram is shown in Figure 3.5. The use of long cadence (29.4 minute) data produces a Nyquist frequency of 24.48 days^{-1} and does not overwhelm the periodogram. The dominant power in the Fourier spectrum lies in a region between 7.5 and 9 days (see Figure 3.5 inset) and contains the ten most powerful peaks in the periodogram (see Table 3.2). These peaks likely represent spot activity at different latitudes over the course of *Kepler* observations. The orbital period of the companion (8.36 days) is not among these periods as the Fourier analysis is optimized toward detection of sinusoidal rather than transit signatures. We select the second-strongest period of 8.23 days for the rotation period used in our spot models since it more likely represents the rotation period of a strong spot closer to the equator than the spot associated with the strongest period (assuming differential rotation in the same sense as the Sun).

3.7 Spot Models for KOI-1003

Light-curve inversion techniques can be employed to reconstruct stellar surfaces through the analysis of the shape of the light curves. As spots form and disappear, the modulations in the light curves change, often from one rotation cycle to the next (e.g., Chapter II). Light-curve inversion methods use regularization procedures to determine

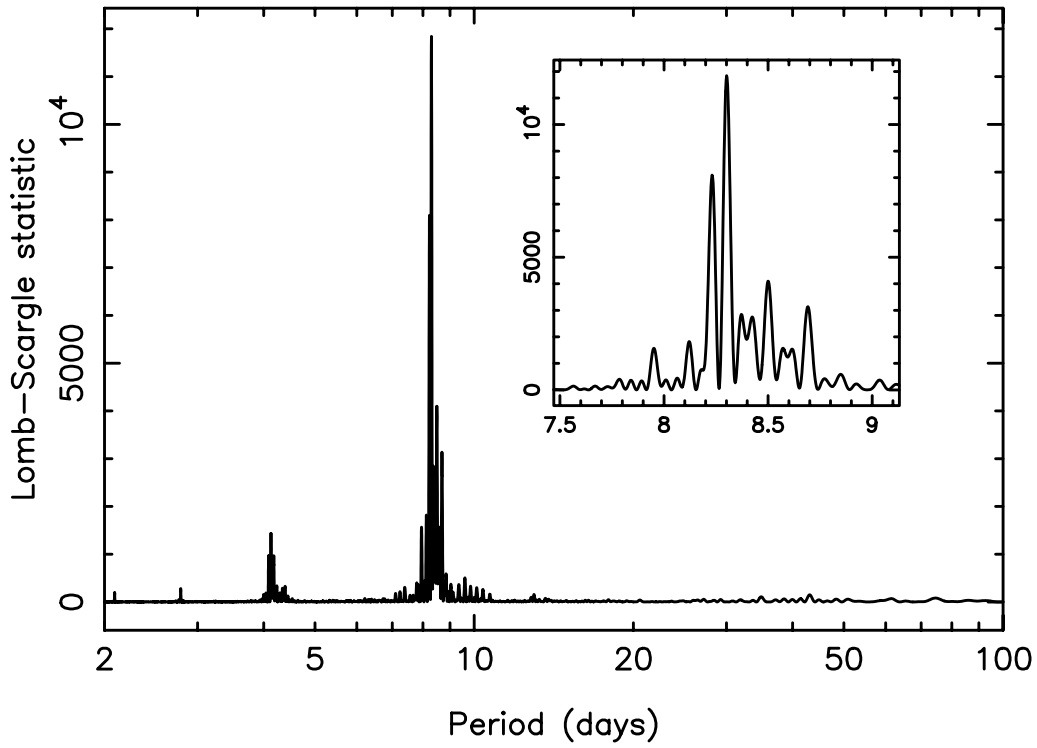

Figure 3.5: Weighted L-S periodogram of *Kepler* Q2−17 photometry. The inset panel shows the detailed Fourier power structure around the potential rotation period of the primary star.

a unique solution for each light curve. Here, we use Light-curve Inversion (LI), a well-tested algorithm for surface reconstructions (tested against simulation and Doppler imaging data, Harmon & Crews, 2000; Roettenbacher et al., 2011, respectively). LI makes no *a priori* assumptions of spot shape, number, or size, but takes as input the estimated root-mean-square noise, σ (expressed in magnitude units), the estimated photospheric and spot temperatures $T_{\rm phot}$ and $T_{\rm spot}$, and the angle of inclination i of the rotation axis to the line of sight. Limb darkening coefficients are also provided and are based upon the estimated $T_{\rm phot}$ and stellar parameters.

The stellar parameters for KOI-1003 include an effective temperature $T_{\rm eff} \sim 5200$ K, surface gravity $\log g \sim 4.5$, and metallicity [Fe/H] ~ -0.1 from Brown et al. (2011). Using an analysis of starspot and photosphere temperatures from Berdyugina (2005), we estimated the difference between the photosphere and the spot to be approximately 1300 K, which gives $T_{\rm spot} \sim 3900$ K. For limb darkening coefficients, we used the logarithmic coefficients provided by Claret et al. (2013) for a 5200 K star with $\log g = 4.5$ and [Fe/H] $= 0$: $e = 0.7369$ and $f = 0.1359$. Although the system is eclipsing, the angle of inclination of the stellar rotation axis is unknown. Therefore, we considered five angles of inclination: $i = 30°, 45°, 60°, 75°$, and $90°$. We neglect $i = 0°$ because this is a pole-on star and there will be no periodic, rotational modulations. $i = 15°$ is neglected because the resulting inversions were qualitatively very different from those for the other inclinations, since the small inclination leads to little modulation unless the spots are unrealistically large.

As the light curve of KOI-1003 shows evidence of both starspots and flares, we have removed the data containing flares. We additionally removed the data for the primary and secondary eclipses. The light curve free of systematic *Kepler* variations (due to CBVs), eclipses, and flares leaves only the features we believe to be the result of cool starspots. The light curves were then divided into light curves with the length of a single rotation period. The data were binned into fifty bins of equal length in

Table 3.3. KOI-1003 Starspot Rotation Periods

Inclination (°)	Low-longitude Spot Slope (°/day)	Period (day)	High-longitude Spot Slope (°/day)	Period (day)
30	-1.21 ± 0.16	8.259	-2.42 ± 0.21	8.287
45	-1.24 ± 0.17	8.260	-2.59 ± 0.22	8.291
60	-1.35 ± 0.19	8.262	-2.67 ± 0.23	8.293
75	-1.21 ± 0.16	8.259	-2.38 ± 0.24	8.286
90	-1.31 ± 0.17	8.261	-2.56 ± 0.23	8.290

order to reduce computation time.

The light curves for individual rotation periods were inverted using LI. The resultant surface reconstructions of these inversions are included in Appendix B. To analyze the starspots, we identify surface patches as being a starspot patch when the intensity of the patch is darker than 95% of the average patch intensity. We calculate the weighted average latitude and longitude, as well as the number of patches in the starspot. We note that the latitude information obtained from the inversions is not reliable, as limited latitude information can be retrieved from a single photometric band.

3.7.1 Persistent Starpots

To understand the motion of the starspots, we plot starspot longitude against time (assigning to the entire rotation the time of the first data point in the light curve) in Figure 3.6. For each inclination, we see that there are two distinct spots that slowly change in longitude, suggesting that the starspots are rotating around the surface more slowly than the stellar rotation. To determine the rate of starspot rotation, we find the slope of the two regions where the spots are distinct, between BJD 2455318.64382 and 2455828.94975. The slopes (°/period) and the associated rotation periods are found in Table 3.3.

The two prominent spot structures appear to have begun (in our observations) as

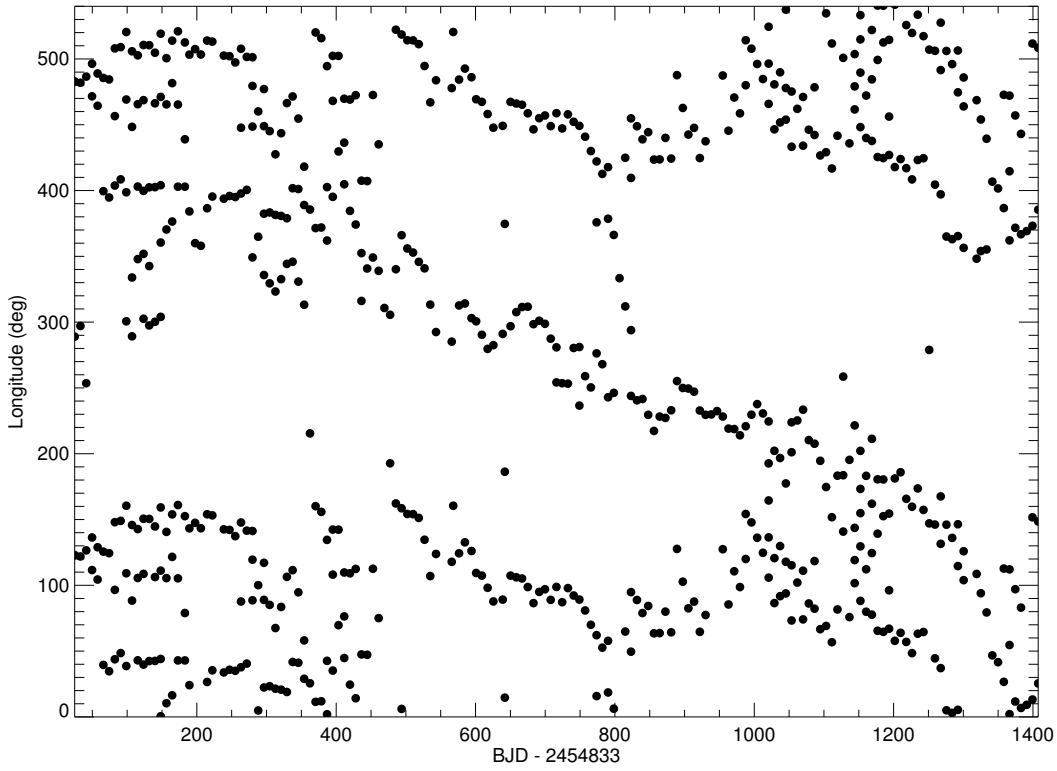

Figure 3.6: Longitude of starspots of KOI-1003 plotted against time. This sample plot is for the longitudes of the surface inversions for $i = 60°$, which has starspots with rotation periods most closely matching the strongest peak in Figure 3.5.

a close structure, separated, and again approaching each other over the course of the *Kepler* light curve. Because of distinct slopes, the starspots appear to be located at different latitudes.

Because these two spot structures are very strong and continuously present, we expect their periods to be present in our period search. Comparing the periods predicted in Table 3.3 to those periods detected in Figure 3.5 and listed in Table 3.2, we find that the periods are not the strong peaks. We note that the low-latitude spot for all inclinations does not move across the surface in a linear way suggesting that the spot is changing latitude. Because of this, we do not expect to see a period exactly matching the low-latitude spot's rotation period. The chosen rotation period for the star is likely tied to the motion of this starspot. The high-latitude spot has more linear trend suggesting that the rotation period of this starspot would be present in Table 3.2. The rotation period for the high-latitude spot most closely matches the strongest peak present (8.30 days). Deviations from this period could be due to the interaction of the starspots or inclination estimate.

3.8 Discussion

The disposition of KOI-1003 has changed several times, flagging the system alternately as a potential planet-hosting star and an eclipsing binary. Significant factors in the inconsistent categorization are variations in the sensitivity of the pixels that the star fell upon during different *Kepler* quarters. The presence of starspots and their location with respect to the timing of the eclipse can also impact the depth.

We determined that the orbital period of the secondary is well-matched with the rotation period of the primary star ($P_{\rm orb} - P_{\rm rot} \approx 0.13$ days, or 1.6% of $P_{\rm orb}$). The system is likely evolving into a synchronized, circular orbit. The system has a predicted age of 8 Gyr (Chaboyer et al., 1999) with $T_{\rm eff} \sim 5200$ K and $\log g \sim 4.5$ (Brown et al., 2011), consistent with a low-mass, main sequence star. Walter (1949)

and Zahn & Bouchet (1989), among others, have shown evidence that binary systems with $P_{\rm orb} \lesssim 10$ days will synchronize while on the main sequence, suggesting KOI-1003 was previously much more eccentric. In order for this near-synchronization to occur, the tidal forces of the primary and secondary would need to be significant, suggesting that the secondary is actually a stellar companion

3.9 Further Work

While the classification of KOI-1003 has been undetermined, we investigate the stellar properties and primary eclipses to better classify the system. The mass-radius relation of exoplanets has been studied on numerous occasions, with simple correlations described by Kane & Gelino (2012) and Weiss & Marcy (2014). However, a size of $\sim 1\ R_{\rm J}$ has considerable ambiguity (stretching well into the brown dwarf regime) as to the nature of the companion without a mass measurement (Baraffe et al., 2008, 2010). The derived radius of the companion depends upon the radius of the host star. According to the NASA Exoplanet Archive, the radius of the host star is $0.823^{+0.259}_{-0.084}\ R_{\odot}$. Using the preliminary depth calculation of $\sim 2\%$, we derive a companion radius of $\sim 1.5 R_{\rm J}$. Although this radius is consistent with a giant planet of low density (e.g., Anderson et al., 2010) there is sufficient uncertainty in the overall companion properties that it cannot be claimed as such without additional constraints, which are difficult to obtain given the star's $K_p = 16.209$.

In order to improve the radius measurement, we are working on modeling the eclipse (isolated from starspots) using the transit-fitting algorithm EXOFAST (Eastman et al., 2013). With the detection of the primary and secondary eclipses, estimates for effective temperature, surface gravity, and metallicity we will be able to place constraints on the radius and orbital elements.

CHAPTER IV

Detecting the Companions and Ellipsoidal Variations of RS CVn Primaries: I. σ Geminorum

4.1 Preface

This chapter is adapted from work of the same title appearing in the Astrophysical Journal, Volume 807, 23 (Roettenbacher et al., 2015c). This work is coauthored by John D. Monnier, Gregory W. Henry, Francis C. Fekel, Michael H. Williamson, Dimitri Pourbaix, David W. Latham, Christian A. Latham, Guillermo Torres, Fabien Baron, Xiao Che, Stefan Kraus, Gail H. Schaefer, Alicia N. Aarnio, Heidi Korhonen, Robert O. Harmon, Theo A. ten Brummelaar, Judit Sturmann, Laszlo Sturmann, and Nils H. Turner. The paper is adapted and partially reproduced here under the non-exclusive rights of republication granted by the American Astronomical Society to the paper authors.

For this work, I collected most of the interferometric data, reducing all of it. I combined the interferometric detections with radial velocity curves to determine the orbital parameters. Using those parameters, I made a model light curve for the system without spots using Eclipsing Light Curve (ELC). With the ELC model, I compared a folded and binned observational light curves to identify ellipsoidal variations and

measure gravity darkening. I also showed that the active longitudes long believed to be on the surface of σ Gem to be those ellipsoidal variations detected. I have created all of the figures and tables in this chapter, as well as written nearly all of the text (with the exception of some of the details of the radial velocity measurements).

4.2 Abstract

To measure the properties of both components of the RS CVn binary σ Geminorum (σ Gem), we directly detect the faint companion, measure the orbit, obtain model-independent masses and evolutionary histories, detect ellipsoidal variations of the primary caused by the gravity of the companion, and measure gravity darkening. We detect the companion with interferometric observations obtained with the Michigan InfraRed Combiner (MIRC) at Georgia State University's Center for High Angular Resolution Astronomy (CHARA) Array with a primary-to-secondary H-band flux ratio of 270 ± 70. A radial velocity curve of the companion was obtained with spectra from the Tillinghast Reflector Échelle Spectrograph (TRES) on the 1.5-m Tillinghast Reflector at Fred Lawrence Whipple Observatory (FLWO). We additionally use new observations from the Tennessee State University Automated Spectroscopic and Photometric Telescopes (AST and APT, respectively). From our orbit, we determine model-independent masses of the components ($M_{\rm A} = 1.28 \pm 0.07\ M_{\odot}$, $M_{\rm B} = 0.73 \pm 0.03\ M_{\odot}$), and estimate a system age of 5 ∓ 1 Gyr. An average of the 27-year APT light curve of σ Gem folded over the orbital period ($P = 19.6027 \pm 0.0005$ days) reveals a quasi-sinusoidal signature, which has previously been attributed to active longitudes 180° apart on the surface of σ Gem. With the component masses, diameters, and orbit, we find that the predicted light curve for ellipsoidal variations due to the primary star partially filling its Roche lobe potential matches well with the observed average light curve, offering a compelling alternative explanation to the active longitudes hypothesis. Measuring gravity darkening from

the light curve gives $\beta < 0.1$, a value slightly lower than that expected from recent theory.

4.3 Introduction

RS Canum Venaticorum (RS CVn) stars are spotted, active binary systems exhibiting photometric and Ca H and K variability (Hall, 1976). Often tidally-locked, these systems are composed of an evolved primary star (giant or subgiant) and a subgiant or dwarf companion (Berdyugina, 2005; Strassmeier, 2009). With active binaries, not only is there potential to determine the component masses and system evolutionary history but also to understand the magnetic field interactions through active longitudes, particular longitudes 180° apart with persistent, long-lived starspots (Berdyugina & Tuominen, 1998; Berdyugina, 2005).

Observing the magnetic phenomena of rapidly-rotating evolved stars also sheds light on the magnetic activity of rapidly-rotating young stars, such as T Tauri stars. Both T Tauri and RS CVn systems have starspots analogous to sunspots—cool starspots resulting from stifled convection in the outer layers of the stars due to strong magnetic fields (Petrov, 2003; Berdyugina, 2005).

σ Geminorum (σ Gem, HD 62044, HIP 37629, HR 2973) is an RS CVn system known to exhibit starspots, often ascribed to "active longitudes" (e.g., Hall et al., 1977; Henry et al., 1995). The system has been characterized as a single-lined spectroscopic binary (Herbig & Spalding, 1955) with a K1III primary (Roman, 1952). The orbital period of σ Gem is slightly longer than the primary star's rotation period derived from the fastest rotating spots ($P_{\rm orb} = 19.60$ days, $P_{\rm rot,min} = 19.47$ days; Kajatkari et al., 2014).

Because of its large starspots, σ Gem is a frequent target for understanding starspot evolution. Eberhard & Schwarzschild (1913) first reported σ Gem as active due to fluctuations in the Ca H and K lines as the star rotated. Decades later,

Hall et al. (1977) identified photometric variations suggesting starspots ($\Delta V \sim 0.07$). Initial models of the surface of σ Gem often showed the surface with two starspots oriented on opposite sides of the primary star (Fried et al., 1983). Berdyugina & Tuominen (1998) emphasize that, due to tidal locking, the starspots are located such that one spot constantly faces the companion and the other spot is 180° offset. The majority of spot models applied to light curves of σ Gem consist of two spots on a spherical star (Eker, 1986; Strassmeier et al., 1988; Oláh et al., 1989; Henry et al., 1995; Jetsu, 1996; Padmakar & Pandey, 1999; Kajatkari et al., 2014). Doppler images have suggested the surface is covered with a larger number of smaller spots (Hatzes, 1993; Kővári et al., 2001, 2014).

To understand the binary system, we present our analysis of the first detections of the companion in our interferometric and radial velocity data sets, as well as photometric data. In Section 4.4, we describe the observations for our data sets. In Section 4.5, we discuss our analysis of the data sets, including the first astrometric and spectroscopic detections of the companion star and orbital parameters. In Section 4.6, we present evolutionary constraints and a Hertzsprung-Russell (H-R) diagram. In Section 4.7, we discuss our analysis of the photometric data set, including detected ellipsoidal variations and measured gravity darkening. In Section 4.8, we present the conclusions of our study of σ Gem. Appendix C includes sample interferometric observables, and Appendix D emphasizes that the previously named active longitudes are actually ellipsoidal variations.

4.4 Observations

4.4.1 Interferometry

We obtained interferometric data with Georgia State University's Center for High-Angular Resolution Astronomy (CHARA) Array. The CHARA Array is a Y-shaped

Table 4.1. Calibrators for σ Geminorum

Calibrator Name	Calibrator Size (mas)	Source	UT Date of Observation
HD 37329	0.71 ± 0.05	Bonneau et al. (2006)	2012 Nov 8
HD 50019 (θ Gem)	0.81 ± 0.06	Bonneau et al. (2006)	2012 Nov 7, 8, 25
HD 63138	0.65 ± 0.04	MIRC calibration	2011 Dec 8; 2012 Nov 8
HD 69897 (χ Cnc)	0.73 ± 0.05	Bonneau et al. (2006)	2012 Nov 7, 24, 25

array of six 1-m class telescopes with non-redundant baselines varying from 34- to 331-m located at Mount Wilson Observatory, California (ten Brummelaar et al., 2005). Using all six telescopes and the Michigan InfraRed Combiner (MIRC; Monnier et al., 2004, 2006), we obtained H-band ($1.5 - 1.8$ μm) data (eight channels across the photometric band with $\lambda/\Delta\lambda \sim 40$) on UT 2011 Nov 9 and Dec 7, 8, 9; 2012 Nov 7, 8, 21, 22, 24, 25 and Dec 4, 5.

We made detections of the companion in the data from UT 2011 Dec 8; 2012 Nov 7, 8, 24, and 25. The remaining nights of observation had insufficient uv coverage due to poor seeing or short observation lengths, leaving the companion undetected. We reduced and calibrated these data with the standard MIRC pipeline (see Monnier, 2007; Monnier et al., 2012; Zhao et al., 2009; Che et al., 2011, for pipeline details). We used at least one calibration star for each night of data (see Table 4.1). For sample interferometric observables, see Appendix C.

4.4.2 Radial Velocity

To constrain the spectroscopic orbit for σ Gem, we utilized three independent sets of radial-velocity data: two sets of single-lined velocities for the primary, and a new set of double-lined velocities for both components of the binary.

One set of the radial velocity measurements for the primary star was published in Massarotti et al. (2008). These 39 data points were obtained with two identical CfA Digital Speedometers (Latham, 1992) on the 1.5-m Wyeth Reflector (Oak Ridge Observatory) and 1.5-m Tillinghast Reflector (Fred Lawrence Whipple Observatory)

telescopes (2003 December 30 − 2007 June 5).

From 2012 October 1 − 2015 January 9, using the Tillinghast telescope with the Tillinghast Reflector Échelle Spectrograph (TRES; Fűrész, 2008), we were able to make fifteen detections of the secondary spectra for the first time. We add 0.14 km s^{-1} to these sets of radial velocities to account for these data being reported on the CfA native system (Stefanik et al., 1999, note the correction is inaccurately stated as a subtraction in this reference).

The additional radial velocity data set consists of 43 spectrograms of the primary star of σ Gem taken between 2009 January 12 − 2014 December 1 with the Tennessee State University 2-m automatic spectroscopic telescope (AST), fiber-fed échelle spectrograph, and a CCD detector at Fairborn Observatory, Arizona (Eaton & Williamson, 2004, 2007). At first, the detector was a 2048 × 4096 SITe ST-002A CCD with 15 μm pixels. Eaton & Williamson (2007) discussed the reduction of the raw spectra and wavelength calibration. Those échelle spectrograms have 21 orders that cover the wavelength range 4920–7100 Å with an average resolution of 0.17 Å, corresponding to a resolving power of 35000 at 6000 Å. Those spectra have a typical signal-to-noise value of 30.

In the summer of 2011 the AST SITe CCD and its dewar were retired and replaced with a Fairchild 486 CCD, a 4096 × 4096 array of 15 μm pixel, that is housed in a new dewar. With the new CCD the wavelength coverage ranged from 3800 to 8600 Å. The resolution was reduced slightly to 0.24 Å or a resolving power of 25000 at 6000 Å. These more recent spectra have signal-to-noise ratios of about 70.

Fekel et al. (2009) provided an extensive general description of velocity measurement of the Fairborn AST spectra. In the case of σ Gem, we measured a subset of 63 lines from our solar-type star line list that covers the 4920–7120 Å region. Because the lines of σ Gem have significant rotational broadening, we fit the individual lines with a rotational broadening function. The Fairborn velocities are on an absolute

scale. A comparison of our unpublished measurements of several IAU standard stars with those determined by Scarfe et al. (1990) indicates that the Fairborn Observatory velocities from the SITe CCD have a small zero-point offset of -0.3 km s^{-1}. Velocities from the Fairchild CCD spectra have a slightly larger zero-point offset of -0.6 km s^{-1} relative to those of Scarfe et al. (1990).

4.4.3 Photometry

We used differential photometry of the primary star of σ Gem and a comparison star from the Tennessee State University T3 0.4-m Automated Photometric Telescope (APT) located at Fairborn Observatory, Arizona. For details on the observational procedure and photometers see Henry (1999) and Fekel et al. (2005).

The differential Johnson B and V light curves cover 1987 November 21 − 2015 March 13 (see Figure 4.1). Subsets of these data were analyzed by Henry et al. (1995) and Kajatkari et al. (2014).

4.5 Orbital Elements

In order to derive the astrometric orbit of σ Gem, we searched for the companion with model fitting. We modeled the system with the resolved primary star and an unresolved secondary. We allowed the primary radius along the major axis, primary major-to-minor axis ratio, primary major axis position angle, primary-to-secondary flux ratio, and secondary position to vary. During the fitting, we weighted the data such that the separate observables (squared visibilities, closure phases, and triple amplitudes) contributed to the final χ^2 with equal weight. The parameter errors for the primary star size and the primary-to-secondary flux ratio were based on the epoch-to-epoch variation, while the relative positional error of the secondary compared to the primary were based on the residuals to the orbit fit (see discussion on orbit fitting).

The coordinates of the detections on five nights (UT 2011 Dec 8; 2012 Nov 7, 8,

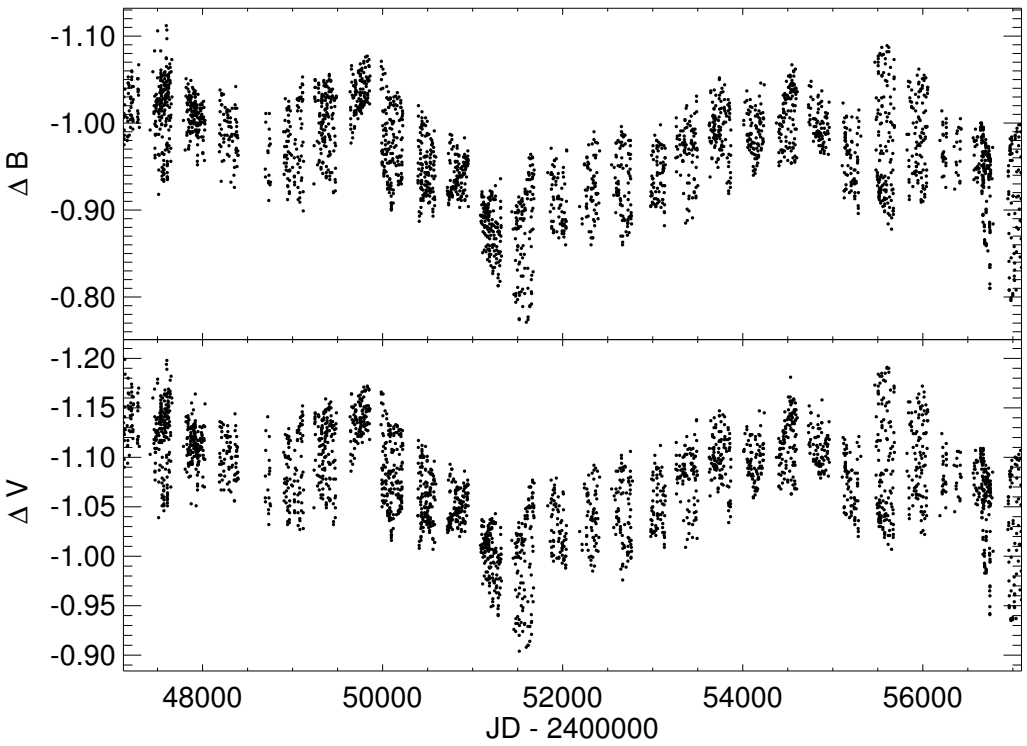

Figure 4.1: Johnson B and V differential magnitudes of σ Gem acquired over 28 observing seasons from 1987 − 2015 with the T3 0.4-meter APT at Fairborn Observatory in southern Arizona.

24, and 25 are listed in Table 4.2). The H-band flux ratio for the primary star to the secondary is 270 ± 70. In addition to detecting the secondary star, we measured the uniform disk diameter of the primary to be $\theta_{\rm UD,A} = 2.335 \pm 0.007$ mas (limb-darkened disk diameter $\theta_{\rm LD,A} = 2.417 \pm 0.007$ mas) with a major-to-minor axis ratio of 1.02 ± 0.03. Our measurements are slightly larger than those in the CHARM2 catalog (uniform disk diameter of $\theta_{\rm UD,A} = 2.18 \pm 0.05$ mas, limb-darkened disk diameter of $\theta_{\rm LD,A} = 2.31 \pm 0.05$ mas; Richichi et al., 2005).

To determine the binary orbit, we simultaneously fit our interferometric and radial velocity data with Monte Carlo realizations. The five interferometric points are as described above, and we present the scaled error bars of the major and minor axis in Table 4.2 to give our fit a total $\chi^2 = 1.00$. For the radial velocity data we combine the Massarotti et al. (2008, adding 0.14 km s^{-1} to account for the values reported on the CfA native system), new CfA data, and the AST data to fit simultaneously with the astrometry. The radial velocity errors are similarly scaled ($\rm rms_{CfA,A} = 0.84$ km s^{-1}, $\rm rms_{AST,A} = 0.3$ km s^{-1}, $\rm rms_{CfA,B} = 3.8$ km s^{-1}).

Using the complete radial velocity data sets, we find an eccentricity of $e = 0.014 \pm 0.004$, consistent with slightly eccentric orbits reported by Harper (1935), Pourbaix et al. (2004), and Massarotti et al. (2008). However, Luyten (1936), Batten et al. (1978), and Dümmler et al. (1997) reported a circular orbit. To investigate this discrepancy, we used the APT light curve to eliminate the primary star's radial velocity data that were obtained when σ Gem presented starspots ($\Delta V > 0.04$), as these could cause shifts in the velocities (e.g., Saar & Donahue, 1997). The remaining primary star radial velocity data obtained when σ Gem did not exhibit large starspots from the Massarotti et al. (2008)/CfA data set span 2006 December 6 − 2007 June 5, and those from the AST data set span 2009 January 12 − June 4. Using the primary star's truncated data set with 42% of the Massarotti et al. (2008)/CfA and 33% of the AST

Table 4.2. Detections for the companion of σ Geminorum with respect to the primary

UT Date	JD −2400000	Separation (mas)	Position Angle (°)[a]	Error Ellipse Major Axis (mas)[b]	Error Ellipse Minor Axis (mas)[b]	Error Ellipse Position Angle (°)[a]	Reduced χ^2
2011 December 08	55903.95	2.83	19.1	0.30	0.09	80	4.4
2012 November 07	56238.97	4.32	8.6	0.04	0.03	280	2.8
2012 November 08	56239.86	4.68	359.7	0.13	0.06	300	2.1
2012 November 24	56256.00	2.03	39.0	0.08	0.06	30	1.5
2012 November 25	56256.95	3.12	21.6	0.05	0.04	320	1.7

Note. — These detections give an H-band ($1.5-1.8$ μm) flux ratio for σ Gem primary to secondary of 270 ± 70. The uniform disk fit for the primary star is $\theta_m athrm UD, A = 2.335 \pm 0.006$ mas (limb-darkened disk diameter $\theta_{\rm LD,A} = 2.417 \pm 0.006$ mas) with a 1.02 ± 0.03 major-to-minor axis ratio.
[a]East of North
[b]Scaled error bars to ensure a total $\chi^2 = 1.00$ as described in Section 3.2.

epochs removed, we find the orbit is consistent with a circular orbit, $e = 0.002 \pm 0.002$, and we adopt a circular orbit for the rest of this chapter.

Requiring eccentricity $e = 0$ and the argument of periastron for the primary $\omega = 0°$ the simultaneous Monte Carlo realizations gave the orbital parameters and their 1-σ errors listed in Table 4.3. The visual orbit is illustrated in Figure 4.2, and the radial velocity curve is presented in Figure 4.3. We use the conventions presented by Heintz (1978), where the argument of periastron, ω, and the time of nodal passage (maximum recessional velocity), T_0, are defined by the primary star's orbit. The ascending node, Ω, is independent of definition, being equivalent with respect to either the primary or secondary star.

Our orbital parallax, $\pi = 25.8 \pm 0.4$ mas can be compared with the Hipparcos parallax of 26.68 ± 0.79 mas (ESA, 1997). As an unresolved binary with a variable component, σ Gem does not exhibit the photocenter shifts found to be troublesome for measuring binary system parallax with Hipparcos (ESA, 1997; Halbwachs & Pourbaix, 2005). Assuming that the secondary is negligibly bright, the semi-major axis of the photocentric orbit of the primary is at most 1.71 mas wide, which is at the limit of detectability (Pourbaix, 2002) for Hipparcos. Combining Hipparcos data and our visual orbit, the parallax is 26.4 ± 0.8 mas, consistent with our orbital parallax. For our subsequent analysis, we adopt our higher-precision orbital parallax, $\pi = 25.8 \pm 0.4$ mas.

With a circular orbit and $P_{\rm orb} \sim P_{\rm rot}$ (e.g., Kajatkari et al., 2014), we expect σ Gem to have aligned rotational and orbital axes. Given our orbital and stellar parameters, we can calculate the obliquity of the system. Comparing our calculated value of $v \sin i = (2\pi R_1 / P_{\rm orb}) \times \sin i = 24.8 \pm 0.4$ km s^{-1} with the observational rotational velocity of $v \sin i = 26.7 \pm 0.5$ km s^{-1} (from the TRES spectra), we find that the calculation is smaller than the observational value. This discrepancy could be attributed to the estimate of microturbulence or the presence of the large spot

Table 4.3. Orbital and Stellar Parameters of σ Geminorum

Measured Parameters	Value
semi-major axis, a (mas)	4.63 ± 0.04
eccentricity, e	0
inclination, i (°)	107.7 ± 0.8
argument of periastron, ω (°)[a]	0
ascending node, Ω (°)	1.2 ± 0.8
period, $P_{\rm orb}$ (days)	19.6027 ± 0.0005
time of nodal passage, T_0 (HJD)[b]	2453583.98 ± 0.03
velocity semi-amplitude, $K_{\rm A}$ (km s^{-1})	34.62 ± 0.08
velocity semi-amplitude, $K_{\rm B}$ (km s^{-1})	60 ± 2
system velocity, γ (km s^{-1})	43.41 ± 0.08
uniform disk diameter, $\theta_{\rm UD,A}$ (mas)	2.335 ± 0.007
limb-darkened disk diameter, $\theta_{\rm LD,A}$ (mas)[c]	2.417 ± 0.007
primary major-to-minor axis ratio	1.02 ± 0.03
H-band flux ratio, primary to secondary	270 ± 70
orbital parallax, π (mas)	25.8 ± 0.4
distance, d (pc)	38.8 ± 0.6
Derived Parameters	
average primary radius, $R_{\rm A}$ ($R_\odot$)[d]	10.1 ± 0.4
primary luminosity, $L_{\rm A}$ ($L_\odot$)	39 ± 2
primary surface gravity, $\log g_{\rm A}$ (cm/s^2)	2.54 ± 0.02
primary mass, $M_{\rm A}$ ($M_\odot$)	1.28 ± 0.07
secondary mass, $M_{\rm B}$ ($M_\odot$)	0.73 ± 0.03
system age (Gyr)	5 ∓ 1
Literature Parameters	
primary effective temperature, $T_{\rm eff,A}$ (K)[e]	4530 ± 60
primary metallicity (iron), Fe/H[f]	0.0

Note. — [a]Radial velocity convention for primary with respect to the center of mass.
[b]Time of maximum recessional velocity of the primary star.
[c]We applied a 3.5% correction from uniform to limb-darkened disk diameter. This is equivalent to a limb-darkening coefficient $\alpha = 0.27$.
[d]Using limb-darkened disk diameter.
[e]$T_{\rm eff,A}$ is an average of temperatures given by Głębocki & Stawikowski (1979); Poe & Eaton (1985); Stawikowski & Głębocki (1994); O'Neal et al. (1996); Kővári et al. (2001); Massarotti et al. (2008). The 1-σ error is the standard deviation of these values.
[f][Fe/H] = −0.02 (Mallik, 1998); approximated as [Fe/H]= 0.00.

structures on the surface of σ Gem during the TRES observations instead of a small, non-zero obliquity.

4.6 Masses and Hertzsprung-Russell Diagram

Using our complete orbital fit, we obtain model-independent masses $M_{\rm A} = 1.28 \pm 0.07\ M_\odot$ and $M_{\rm B} = 0.73 \pm 0.03\ M_\odot$. With the stellar parameters of the primary star (including $T_{\rm eff,A} = 4530 \pm 60$ K, see Table 4.3) and the primary-to-secondary

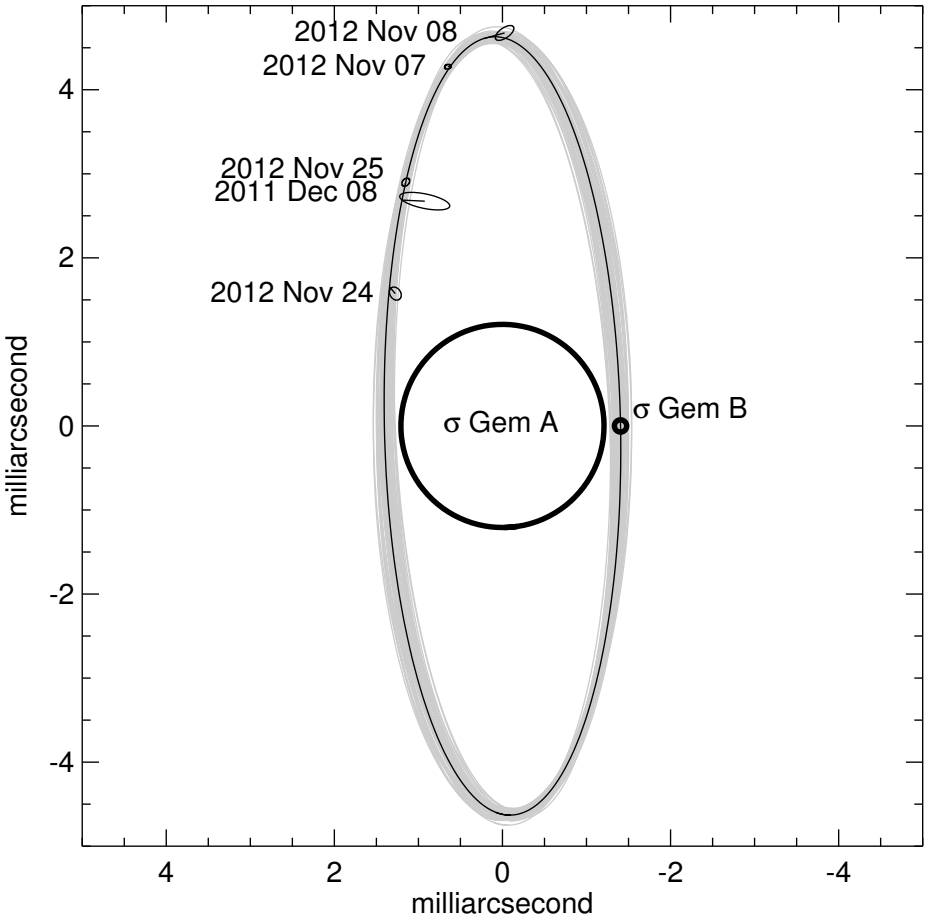

Figure 4.2: Visual orbit for the prototypical RS CVn system σ Gem with our observed stellar primary radius (thick black line, σ Gem A) and our dates of companion detection and their locations on the orbit (black error ellipses). The predicted radius of the companion star, σ Gem B, is plotted for scale with the small thick black circle. The orbits of fifty Monte Carlo realizations are presented as the light gray orbits. Black lines connect the center of the detection error ellipse to the expected point in the best-fit orbit, which is overlaid in black (given in Table 4.3 with 1-σ errors). At the southernmost point in the orbit, the secondary star is moving toward the observer. Note: axis units are milliarcseconds (mas) with north upwards and east to the left.

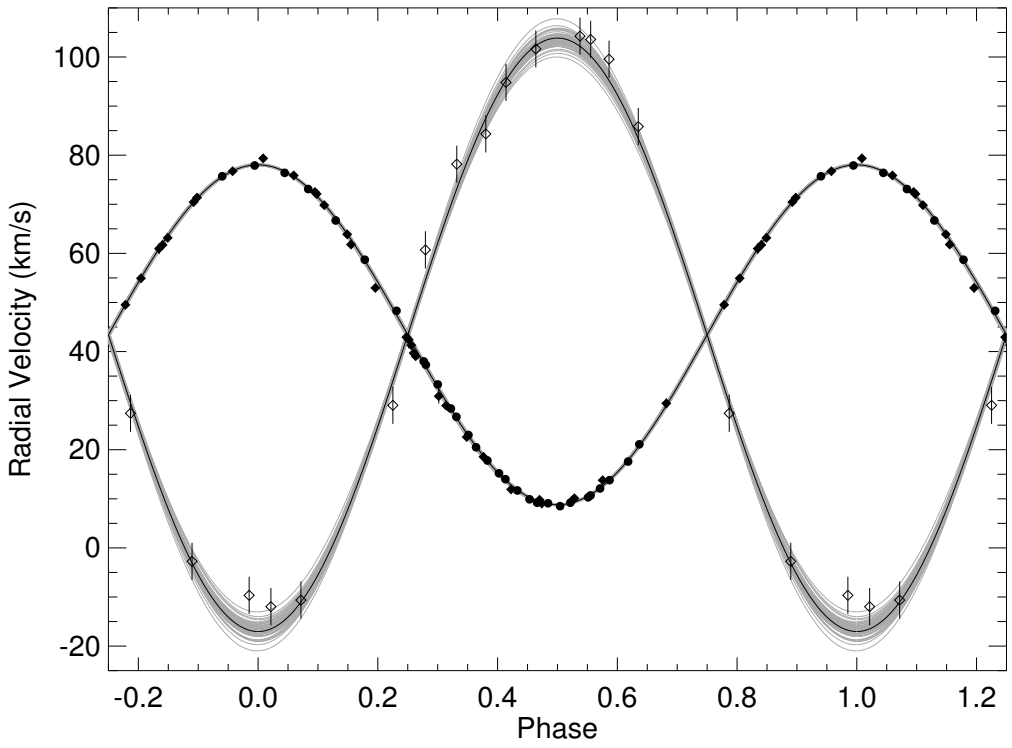

Figure 4.3: Radial velocity curves of σ Gem. The filled diamonds represent our sample of measured observations from Massarotti et al. (2008)/CfA, and the filled circles are the AST observations. Both data sets are restricted to those data points obtained with no starspots present (see Section 4.5). 1-σ errors in velocity are presented unless the error is smaller than the diamonds and circles. The radial velocity curves of fifty Monte Carlo realizations are presented as the light gray orbits. The radial velocity for the best orbital parameters is overlaid in black. Similarly, the open diamonds represent CfA radial velocity data for the secondary star with 1-σ error bars. The light gray orbits are fifty Monte Carlo realizations with the best orbital parameters overlaid in black. See Table 4.3 for orbital parameters with 1-σ errors.

H-band flux ratio detected using the CHARA/MIRC data (270 ± 70), we are able to constrain the parameters (luminosity, temperature, and radius) of the secondary star. We use the flux ratio and NextGen stellar atmospheres (Hauschildt et al., 1999) to constrain the stellar flux to calculate a range of luminosities for reasonable effective temperatures ($4000 - 4700$ K) for a 0.73 ± 0.03 $M_{\odot}$ main sequence star (see Figure 4.4). We obtain a range of luminosities ($0.11 - 0.15$ $L_{\odot}$) and radii ($0.70 - 0.59$ $R_{\odot}$). We note that our analysis predicts a primary-to-secondary Johnson V-band flux ratio of 290 assuming $T_{\rm eff,B} = 4500$ K), which is not in agreement with the flux ratio given by the spectroscopic 519 nm light ratio (~ 70 primary-to-secondary). In order for our flux ratios to be in agreement, the secondary star would have $T_{\rm eff,B} = 6400$ K, which is not consistent with the spectroscopic observations, nor with a main-sequence star given the location on the H-R diagram. We cannot rule out the effect of starspots on the discrepant flux ratios as these were not accounted for when interferometrically detecting the companion and the spot features present during the interferometric and spectroscopic observations differ as evidenced in the APT light curve. Additionally, Prato et al. (2002) and Lehmann et al. (2013) also reported discrepancies between TODCOR-reported flux ratios and their expected values. Therefore, we use only the H-band flux ratio.

We plot the location of the components of σ Gem on an H-R diagram, as well as the corresponding evolutionary tracks. We use Dartmouth stellar evolution tracks (Fe/H $= 0.0$, α/Fe $= 0.0$, PHOENIX-based models; Dotter et al., 2008) for the interpolated model masses ($M_{A,\rm model} = 1.28 \pm 0.07$ $M_{\odot}$, $M_{B,\rm model} = 0.73 \pm 0.03$ $M_{\odot}$). Our primary falls nearly on the 1.28 $M_{\odot}$ evolutionary track with an estimated temperature of 4530 ± 60 K (Głębocki & Stawikowski, 1979; Poe & Eaton, 1985; Stawikowski & Głębocki, 1994; O'Neal et al., 1996; Kővári et al., 2001; Massarotti et al., 2008). The range of locations for the secondary on the H-R diagram passes through the main sequence for a star of 0.73 $M_{\odot}$. We find an age of the system of 5 ∓ 1 Gyr. Based

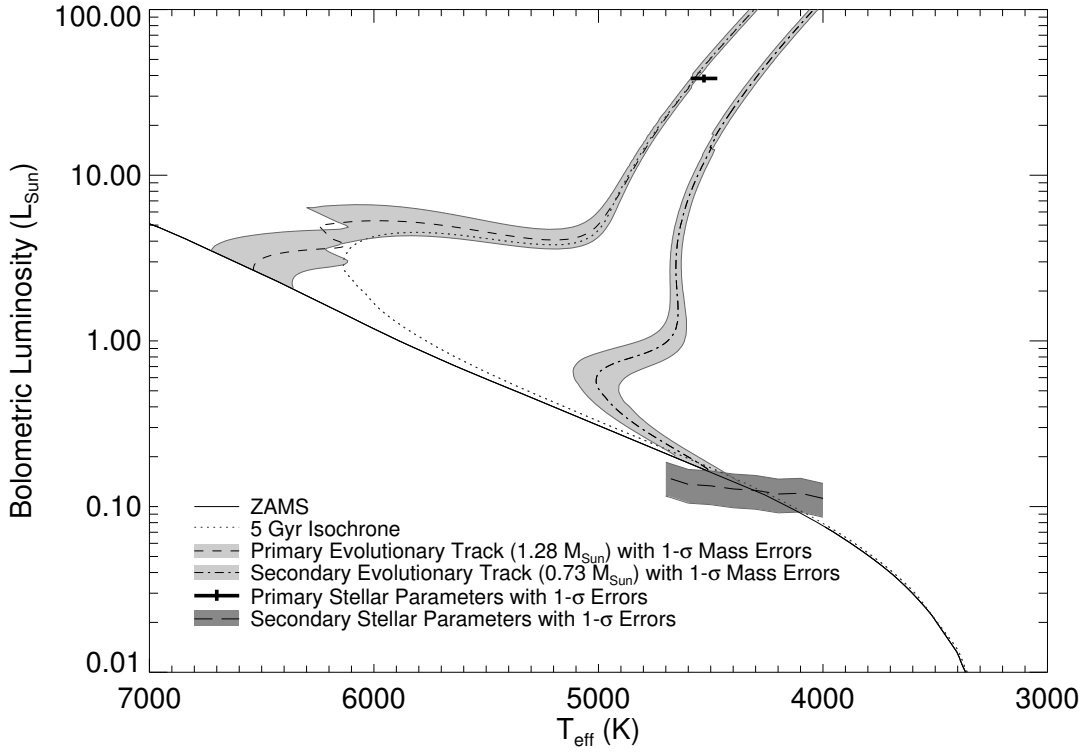

Figure 4.4: H-R diagram for σ Gem. The dashed and dot-dashed lines are the main sequence and post-main sequence evolutionary tracks for 1.28 $M_{\odot}$ and 0.73 $M_{\odot}$ stars with $[Fe/H] \sim 0.0$, respectively (Dotter et al., 2008). The gray regions represent our 1-σ mass errors ($M_{\rm A} = 1.28 \pm 0.07\ M_{\odot}; M_{\rm B} = 0.73 \pm 0.03\ M_{\odot}$) with the solid black line representing the zero age main sequence. The dotted line is a 5 Gyr isochrone (PHOENIX; Dotter et al., 2008). The measured location of the primary with 1-σ errors is indicated by the plus sign. The region where the companion could be located given our flux ratio and reasonable temperature estimates is indicated with the long-dashed line (with 1-σ errors in luminosity).

upon the masses and age of the stars, we suggest that the primary star was a late F-type star while on the main sequence, but is now a K giant. The secondary star is a main-sequence early K star.

4.7 Ellipsoidal Variations and Gravity Darkening

Henry et al. (1995) and Kajatkari et al. (2014) previously published subsets of the APT light curve data for starspot modeling and measuring differential rotation. Both studies emphasized the presence of active longitudes on opposite sides of σ Gem to explain the quasi-sinusoidal variation appearing at half of the orbital period.

We removed long-term trends, folded the APT photometry over the orbital period ($P_{\rm orb} = 19.6027$ days), and binned the data (0.025 in phase). The resultant Johnson B and V light curves are presented in Figure 4.5. The quasi-sinusoidal trend observed in the averaged light curves suggests the possibility of ellipsoidal variations due to distortions of the primary star partially filling its Roche lobe potential. With a Roche lobe radius of 16.5 $R_{\odot}$, we obtain $R_1/R_{\rm L} = 0.61$ (Eggleton, 1983).

We used the light-curve-fitting software package Eclipsing Light Curve (ELC; Orosz & Hauschildt, 2000) to model the ellipsoidal variations using our orbital parameters with no free parameters (gravity darkening assumed to be $\beta = 0.08$; Lucy, 1967, see Figure 4.5). The characteristics of the ellipsoidal variations with this model as compared to the light curve of σ Gem indicate that the long-term signature likely is indeed due to ellipsoidal variations, in contrast to previous suggestions that the periodicity at $P_{\rm orb}/2$ is due to active longitudes aligned with the orbit (e.g., Henry et al., 1995; Jetsu, 1996; Berdyugina & Tuominen, 1998; Kajatkari et al., 2014; Kővári et al., 2014). We note that rotation periods derived from the analysis of the light curve (e.g., Kajatkari et al., 2014) suggest the star is rotating slightly faster than the orbital period, further supporting our identification of ellipsoidal variations in σ Gem. It should be noted that removing the effect of ellipsoidal variations from the

light curve does not eliminate all starspot signatures (See Appendix D).

The ELC model fit of ellipsoidal variations can be improved to better match our data. We modeled the system again with no free parameters except for the gravity darkening coefficient, β for $T_{\rm eff} \propto g^{\beta}$ (von Zeipel, 1924), as Espinosa Lara & Rieutord (2012) recently suggested $\beta \sim 0.21$ for convective stars, substantially higher than the canonical $\beta \sim 0.08$ (Lucy, 1967) value assumed in our fixed-parameter fit. Although our average light curve is still contaminated by some residual spot modulation, we find that $\beta = 0.02 \pm 0.02$ with error bars determined by bootstrapping over observing seasons of the 27 years of observation in the APT light curve. This value strongly rules out $\beta > 0.1$ for this system (see Figure 4.5).

4.8 Conclusions

In this work, we have made the first visual detections of the secondary star of σ Gem using interferometric and spectroscopic observations. We establish the first visual orbit by combining the interferometric detections with radial velocity data. The determination of orbital parameters has allowed for model-independent mass determinations ($M_{\rm A} = 1.28 \pm 0.07\ M_{\odot}, M_{\rm B} = 0.73 \pm 0.03\ M_{\odot}$).

Folded and binned photometric data have shown evidence of ellipsoidal variations, gravitational distortions of the primary star caused by the close companion. The light curve is comparable to light curve models created only from stellar and orbital parameters (assuming no starspots). Although the ellipsoidal variations are only a small effect, the primary star of σ Gem is not spherical, partially filling its Roche lobe potential and having a surface temperature gradient. Our establishment of ellipsoidal variations offers a compelling alternative explanation to the previously purported detections of active longitudes, starspots on either side of the primary star (Henry et al., 1995; Jetsu, 1996; Berdyugina & Tuominen, 1998; Kajatkari et al., 2014; Kővári et al., 2014).

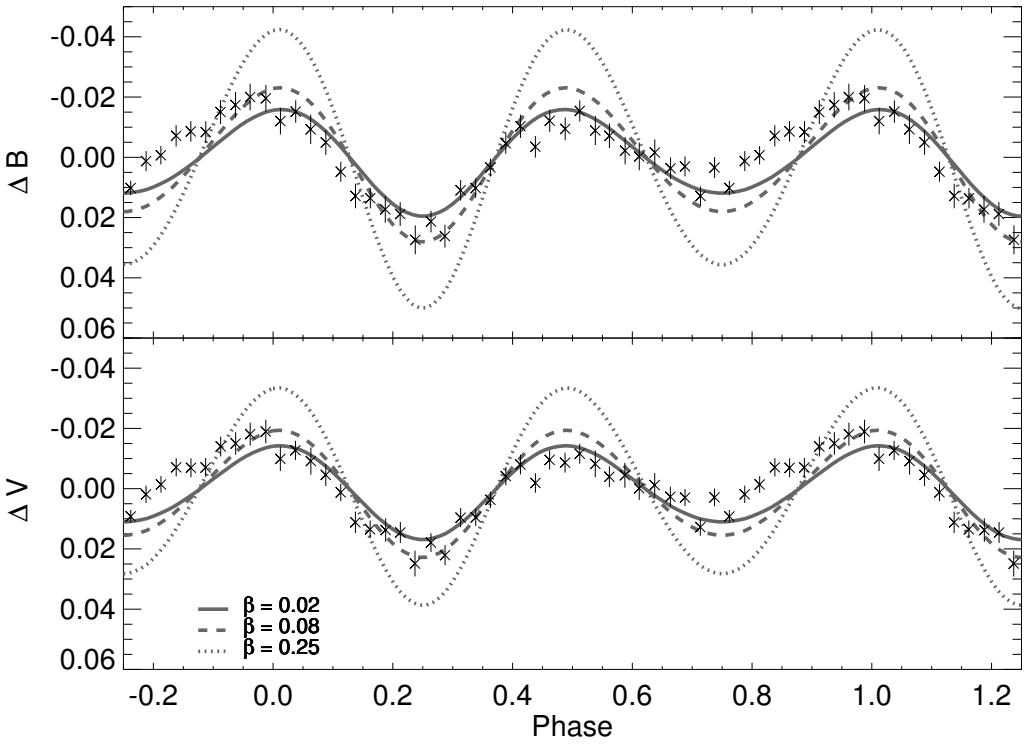

Figure 4.5: Differential folded and binned light curves of σ Gem for B and V magnitudes plotted with error bars from the binning. Each data point is an average of data points spanning 0.025 in phase from the complete light curve folded on the orbital period. The quasi-sinusoidal signature of the averaged light curve is due to ellipsoidal variations caused by the primary star partially filling its Roche lobe potential. The lines represents the ELC models for ellipsoidal variations with the gravity darkening coefficient $\beta = 0.02, 0.08$, and 0.25, where $\beta = 0.02 \pm 0.02$ is the best fit to the binned light curves.

Our new orbital elements along with the folded light curve also allow for measurements of gravity darkening. We find that $\beta = 0.02 \pm 0.02$, a value of gravity darkening lower than suggested by theory (Lucy, 1967; Espinosa Lara & Rieutord, 2011, 2012).

CHAPTER V

Detecting the Companions and Ellipsoidal Variations of RS CVn Primaries: II. *o* Draconis, a Candidate for Recent Low-Mass Companion Ingestion

5.1 Preface

This chapter is adapted from work of the same title appearing in the Astrophysical Journal, Volume 809, 159 (Roettenbacher et al., 2015a). This work is coauthored by John D. Monnier, Francis C. Fekel, Gregory W. Henry, Heidi Korhonen, David W. Latham, Matthew W. Muterspaugh, Michael H. Williamson, Fabien Baron, Theo A. ten Brummelaar, Xiao Che, Robert O. Harmon, Gail H. Schaefer, Nicholas J. Scott, Judit Sturmann, Laszlo Sturmann, and Nils H. Turner. The paper is adapted and partially reproduced here under the non-exclusive rights of republication granted by the American Astronomical Society to the paper authors.

For this work, I collected the interferometric data, reducing all of it. I combined the interferometric detections with radial velocity curves to determine the orbital parameters. Using those parameters, I made a model light curve for the system without spots using Eclipsing Light Curve (ELC). With the ELC model, I compared

a folded and binned observational light curves to identify ellipsoidal variations and measure gravity darkening. I also estimated the actual rotation period of *o* Dra by removing the ellipsoidal variations from the light curve. I have created all of the figures and tables in this chapter, as well as written nearly all of the text (with the exception of some of the details of the radial velocity measurements).

5.2 Abstract

To measure the stellar and orbital properties of the metal-poor RS CVn binary *o* Draconis (*o* Dra), we directly detect the companion using interferometric observations obtained with the Michigan InfraRed Combiner at Georgia State University's Center for High Angular Resolution Astronomy (CHARA) Array. The H-band flux ratio between the primary and secondary stars is the highest confirmed flux ratio (370 ± 40) observed with long-baseline optical interferometry. These detections are combined with radial velocity data of both the primary and secondary stars, including new data obtained with the Tillinghast Reflector Échelle Spectrograph on the Tillinghast Reflector at the Fred Lawrence Whipple Observatory and the 2-m Tennessee State University Automated Spectroscopic Telescope at Fairborn Observatory. We determine an orbit from which we find model-independent masses and ages of the components ($M_{\rm A} = 1.35 \pm 0.05\ M_{\odot}$, $M_{\rm B} = 0.99 \pm 0.02\ M_{\odot}$, system age $= 3.0 \mp 0.5$ Gyr). An average of a 23-year light curve of *o* Dra from the Tennessee State University Automated Photometric Telescope folded over the orbital period newly reveals eclipses and the quasi-sinusoidal signature of ellipsoidal variations. The modeled light curve for our system's stellar and orbital parameters confirm these ellipsoidal variations due to the primary star partially filling its Roche lobe potential, suggesting most of the photometric variations are not due to stellar activity (starspots). Measuring gravity darkening from the average light curve gives a best-fit of $\beta = 0.07 \pm 0.03$, a value consistent with conventional theory for convective envelope stars. The primary star

also exhibits an anomalously short rotation period, which, when taken with other system parameters, suggests the star likely engulfed a low-mass companion that had recently spun-up the star.

5.3 Introduction

RS Canum Venaticorum (RS CVn) stars are active binary systems with Ca H and K and photometric variability (Hall, 1976). The components of these close binary systems are typically an evolved giant or subgiant primary star with a subgiant or main sequence companion (Berdyugina, 2005; Strassmeier, 2009).

In close binary systems, the stars experience changes in energy and angular momentum, circularizing the orbit due to forces from the aspherical mass distributions of the (partially) Roche-lobe-filling primary stars (Zahn, 1977). Observations of open clusters have shown a transition period, the range of orbital periods between the longest circular orbit and the shortest eccentric orbit, which monotonically increases with cluster age (Mazeh, 2008, and references therein). Observations and predictions have shown that stars with orbital periods $P_{\rm orb} \lesssim 10$ days will have circularized while on the main sequence, regardless of spectral type (e.g., Walter, 1949; Koch & Hrivnak, 1981; Zahn & Bouchet, 1989). As stars evolve off of the main sequence and cool while becoming subgiants and giants, circularization is expected for stars with periods $P_{\rm orb} \lesssim 100$ days (e.g., Mayor & Mermilliod, 1984; Claret, 2009). Therefore, RS CVn systems with orbital periods longer than 100 days are likely to retain primordial non-zero eccentricities.

The single-lined RS CVn system *o* Draconis (omicron Draconis, *o* Dra, 47 Dra, HD 175306, HIP 92512, HR 7125; G9III; Herbig & Spalding, 1955; Young & Koniges, 1977; Walter, 1985; Strassmeier et al., 1989) has a previously-measured orbital period of $P_{\rm orb} \sim 138$ days with a non-zero eccentricity of $e \sim 0.1$ (e.g., Young, 1921; Lucy & Sweeney, 1971; Massarotti et al., 2008). The primary star of *o* Dra rotates faster

than would be expected from tidal synchronization (e.g. Głębocki & Stawikowski, 1988; Massarotti et al., 2008).

To achieve this rapid rotation, the primary star must have increased its angular momentum. One possibility is that the primary star engulfed a nearby companion, an event that would have had a strong impact on the primary star and its subsequent evolution. This evolution could shed light on the future of the Solar System as the Sun expands to ingest planets (e.g., Schröder & Connon Smith, 2008). To investigate this hypothesis, we aim to better determine o Dra's stellar parameters (e.g., Basri et al., 1985; Gurzadyan & Cholakyan, 1995) and thereby resolve the binary system's history.

To advance our understanding of o Dra, we present the first detections of the low luminosity companion with six nights of interferometric data and the companion's first radial velocity detections. We describe these data sets along with radial velocity and photometric data of the primary star in Section 5.4. We detail the analysis of observations with resultant orbital parameters in Section 5.5. We describe the analysis of our photometry, show the detected ellipsoidal variations and eclipses, and measure gravity darkening of the primary component in Section 5.6. We show our results on an Hertzsprung-Russell (H-R) diagram and discuss the system's evolution in Section 5.7. Finally, we present the conclusions of our study of o Dra in Section 5.8. Appendix E contains sample interferometric observables.

5.4 Observations

5.4.1 Interferometry

We obtained interferometric data at Georgia State University's Center for High-Angular Resolution Astronomy (CHARA) Array. The CHARA Array is a Y-shaped array of six 1-m class telescopes with non-redundant baselines varying from 34- to 331-

m located at Mount Wilson Observatory, California (ten Brummelaar et al., 2005). Using all six telescopes and the Michigan InfraRed Combiner (MIRC; Monnier et al., 2004, 2006; Che et al., 2011), we obtained H-band ($1.5-1.8$ μm) data (eight channels across the photometric band with $\lambda/\Delta\lambda \sim 40$) on UT 2012 May 9, 11, 12 and June 6, 8, 17, 18; 2014 May 25, 26, 27, June 29, 30, and July 1.

We detected the faint companion in the data from UT 2012 May 9, 12; 2012 June 17, 18; and 2014 May 26, 27. The nights of observation without detections of the companion had insufficient uv coverage due to poor seeing, short observation lengths, or observations during eclipse leaving the companion undetected. We reduced and calibrated these data with the standard MIRC pipeline (see Monnier, 2007; Zhao et al., 2009; Monnier et al., 2012, for pipeline details). We used at least two calibration stars for each night of data (see Table 5.1).

Three of our seven calibrators are A stars, which were revealed to be oblate due to rapid rotation during our analysis and required more information for calibration. Each of the stars were calibrated with a non-oblate star when possible, but some nights of observation required the use of other oblate stars. HD 185395 (θ Cyg) was used on 2012 June 17 to calibrate HD 192696 (33 Cyg) and HD 184006 (ι Cyg). On nights when HD 185395 was not available (2012 June 8 and 18), HD 192696 and HD 184006 were used to calibrate each other. HD 192696 was used to calibrate HD 106591 (δ UMa) on 2012 May 9, 11, and 12). The calibrated visibilities were fit to models of oblate stars to determine the mean uniform disk diameter, major-to-minor axis ratio, and position angle of the major axis (east of north), the mean values of which are in the footnotes of Table 5.1.

5.4.2 Radial Velocity

We combined three radial velocity data sets of the primary star and one set for the secondary to further constrain our orbit of o Dra.

Table 5.1. Calibrators for *o* Draconis

Calibrator Name	Calibrator Size (mas)[a]	Source	UT Date of Observation
HD 106591 (δ UMa)	oblate[b]	MIRC calibration	2012 May 9, 12
HD 125161 (ι Boo)	0.49 ± 0.03	Bonneau et al. (2006)	2012 May 9, 12
HD 138852	1.00 ± 0.06	Bonneau et al. (2006)	2014 May 26
HD 184006 (ι Cyg)	oblate[c]	MIRC calibration	2012 Jun 17, 18; 2014 May 26, 27
HD 185264	0.80 ± 0.06	Bonneau et al. (2006)	2014 May 26, 27
HD 185395 (θ Cyg)	0.73 ± 0.02	White et al. (2013)	2012 Jun 17
HD 192696 (33 Cyg)	oblate[d]	MIRC calibration	2012 May 9, 12, Jun 17, 18

Note. — [a] Some calibration stars are rapidly rotating and distorted from spherical. They were modeled as H-band uniform ellipses for calibration. For each star we list the H-band uniform disk mean diameter (mas), major-to-minor axis ratio, and position angle of the major axis (°, east of north).
[b] $\theta_{\rm UD,mean} = 0.78 \pm 0.02$, major/minor $= 1.29 \pm 0.05$, $\rm PA_{maj} = 113 \pm 5°$
[c] $\theta_{\rm UD,mean} = 0.72 \pm 0.02$, major/minor $= 1.29 \pm 0.04$, $\rm PA_{maj} = 92 \pm 4°$
[d] $\theta_{\rm UD,mean} = 0.56 \pm 0.02$, major/minor $= 1.41 \pm 0.09$, $\rm PA_{maj} = 115 \pm 6°$

Three radial velocities published in Massarotti et al. (2008) were obtained with the CfA Digital Speedometer on the Wyeth Reflector at the Oak Ridge Observatory (Harvard, MA; 2004 September 1− 2005 April 14). Two radial velocities also published in Massarotti et al. (2008) were obtained with the CfA Digital Speedometer on the Tillinghast Reflector at the Fred L. Whipple Observatory (Mount Hopkins, AZ; 2006 June 14 − 2007 September 21). Six additional radial velocities (2012 May 9 − 2012 October 10) for the primary star were taken with the Tillinghast Reflector Échelle Spectrograph (TRES) at the Tillinghast Reflector.

With the Tennessee State University 2-m Automatic Spectroscopic Telescope (AST) at Fairborn Observatory, AZ, we have determined radial velocities from 86 spectrograms of the primary of *o* Dra taken between 2007 October 11 − 2014 October 28 and 19 measurements of the companion radial velocity (2012 October 10 − 2014 October 28). See Fekel et al. (2009) and Chapter IV for details on these observations.

We additionally include 18 archival radial velocities of the primary star from Young (1921, 1902 July 15 − 1920 August 9).

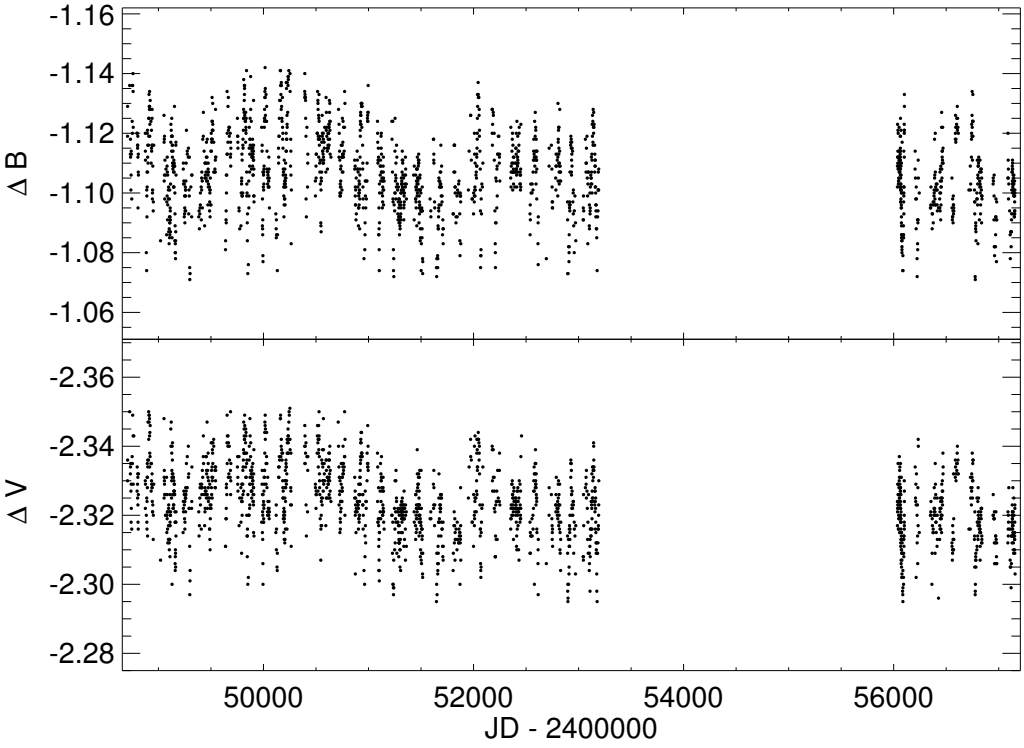

Figure 5.1: Johnson B and V differential magnitudes of o Dra acquired over 23 years from 1992 − 2015 with the T3 0.4-meter APT at Fairborn Observatory in southern Arizona.

5.4.3 Photometry

o Dra has been monitored since 1992 with Tennessee State University's T3 0.4-m Automatic Photometric Telescope (APT) at Fairborn Observatory. Our observations span over 23 years from 1992 March 24 − 2015 May 13, but with a gap during 2005−2011 (see Figure 5.1). Our Johnson B and V measurements of o Dra were made differentially with respect to the comparison star HD 175511 (HIP 92594; B9; see Figure 5.2) and the check star HD 176408 (K1III). Details of the robotic telescopes and photometers, observing procedures, and data analysis techniques can be found in Henry (1999) and Fekel et al. (2005).

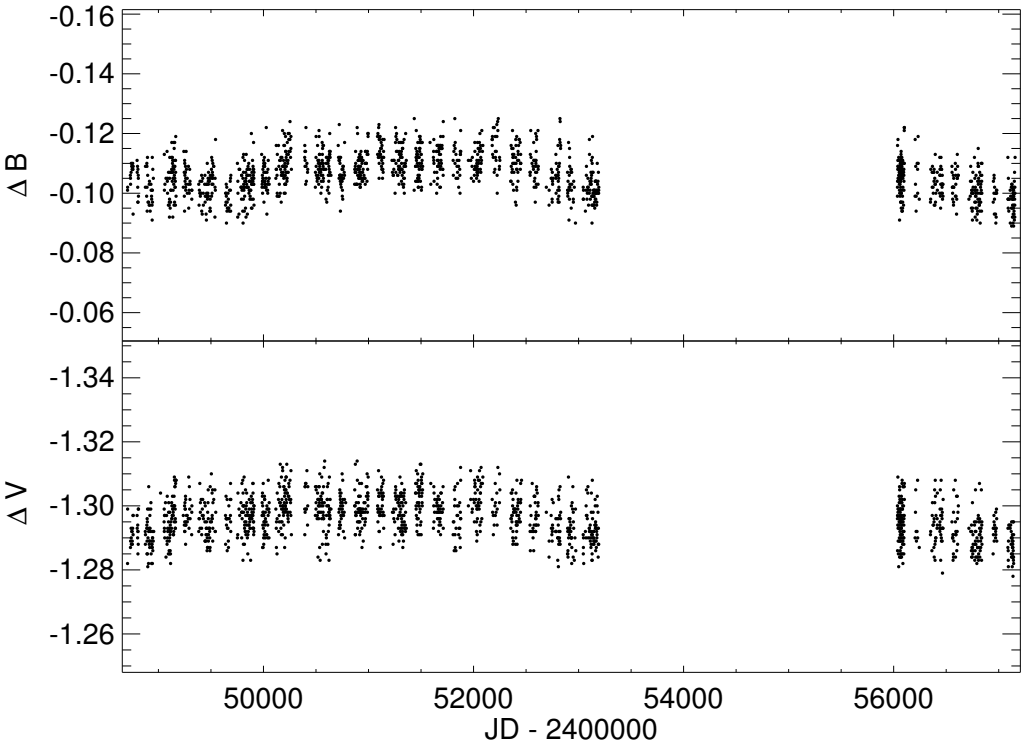

Figure 5.2: Johnson B and V differential magnitudes of comparison star HD 175511 (with the check star 48 Dra).

5.4.4 High-Resolution Spectroscopy

We use high-resolution spectra of o Dra covering the spectral range of 3700−7300 Å obtained at the Nordic Optical Telescope (NOT) with the FIES high resolution échelle spectrograph. In the current work, the 1.3 arcsec fiber giving a resolving power ($\lambda/\Delta\lambda$) of 67000 was used. The exposure time for each spectrum was 180 s and resulted in a typical signal-to-noise ratio of 500 per resolution element (four pixels) at 6420 Å. The observations were carried out at thirteen epochs between 2012 April 17 − August 15. All the spectra were reduced with the dedicated FIES reduction software FIEStool.

5.5 Orbital Elements and Masses

Using model fitting for the location of the unresolved secondary star with respect to the resolved primary star, we directly detected the companion of o Dra. Our models allow the primary star's major axis and major-to-minor axis ratio, primary-to-secondary H-band flux ratio, and the secondary's position to vary. During the fitting for the companion we weighted the closure phases ten times more strongly in the final χ^2 than the squared visibilities and triple amplitudes in order to better identify asymmetries in the system to detect the faint companion (the detection of the companion is not sensitive to the factor of 10; see Figures E.1 − E.4 in Appendix E). Errors for the primary star's size and shape and the primary-to-secondary H-band flux ratio are based on the individual epochs. The positional errors of the location of the secondary are error ellipses based upon the shape of the χ^2 surface used to detect the companion.

The coordinates of the secondary detections on six nights (UT 2012 May 9, 12; June 17, 18; and 2014 May 26, 27) are listed in Table 5.2. We measured the H-band uniform disk diameter of the primary star to be $\theta_{\rm UD,A} = 2.115 \pm 0.007$ mas (limb-

darkened disk $\theta_{\mathrm{LD,A}} = 2.189 \pm 0.007$, obtained by assuming a limb darkening power law exponent $\alpha = 0.27$) with a major-to-minor axis ratio of 1.01 ± 0.03. The H-band flux ratio for the primary star to the secondary is 370 ± 40, the highest confirmed binary flux ratio measured with long-baseline optical interferometry (RT Aur has an unconfirmed H-band flux ratio of $\sim$ 450:1, measured by MIRC at the CHARA Array; Gallenne et al., 2015).

Table 5.2. Detections for the companion of o Draconis with respect to the primary

UT Date	JD −2400000	Separation (mas)	Position (°)[a]	Error Ellipse Major Axis (mas)[b]	Error Ellipse Minor Axis (mas)[b]	Error Ellipse Position Angle (°)[a]	Reduced χ^2
2012 May 09	56056.97	6.52	23.1	0.06	0.04	340	1.3
2012 May 12	56059.95	6.36	23.7	0.05	0.03	60	1.5
2012 June 17	56095.87	3.71	203.1	0.04	0.03	310	1.6
2012 June 18	56096.82	3.96	202.3	0.02	0.02	330	1.5
2014 May 26	56803.87	6.03	202.5	0.07	0.05	20	0.9
2014 May 27	56804.85	6.04	202.0	0.16	0.04	330	1.1

Note. — These detections give an H-band ($1.5 - 1.8$ μm) primary-to-secondary flux ratio for o Dra A to B of 370 ± 40. The uniform disk fit for the primary star is 2.115 ± 0.007 mas (limb-darkened disk 2.189 ± 0.007) with a 1.01 ± 0.03 major-to-minor axis ratio.
[a]East of North
[b]Scaled error bars to ensure a reduced $\chi^2 = 1.00$ as described in Section 5.5.

We calculate the orbital parameters of the binary by simultaneously fitting our interferometric and radial velocity data with Monte Carlo realizations. For our six interferometric points we present the error ellipses of the major and minor axis in Table 5.2 scaled to give our fit a reduced $\chi^2 = 1.00$. The radial velocity errors are similarly scaled to require $\chi^2 = 1.00$ ($\mathrm{rms}_{\mathrm{CfA,A}} = 0.39\,\mathrm{km\,s^{-1}}$, $\mathrm{rms}_{\mathrm{AST,A}} = 0.22\,\mathrm{km\,s^{-1}}$, $\mathrm{rms}_{\mathrm{AST,B}} = 1.6$ km s^{-1}, $\mathrm{rms}_{\mathrm{Young,A}} = 2.2$ km s^{-1}).

The simultaneous radial velocity and astrometry Monte Carlo realizations of the orbit gave the orbital parameters and their 1-σ errors listed in Table 5.3. The orbit is represented in Figure 5.3 with the radial velocity curve in Figure 5.4. We use the conventions presented by Heintz (1978), where the argument of periastron, ω, follows the radial velocity orbit convention (the primary star with respect to the center of mass), which is different from the visual orbit convention (the secondary star with respect to the primary). The position angle of the ascending node (E of N), Ω, is independent of definition being equivalent with respect to either the primary or secondary star.

Our double-lined and visual orbit confirms previous analyses of orbital period and non-zero eccentricity (e.g., Young, 1921; Lucy & Sweeney, 1971), while highlighting new evidence that the system is eclipsing ($i = 89.6 \pm 0.3°$). We determine the masses of the stars to be $M_{\mathrm{A}} = 1.35 \pm 0.05\ M_{\odot}$ and $M_{\mathrm{B}} = 0.99 \pm 0.02\ M_{\odot}$; the implications to system evolution will be discussed in Section 5.7. Our orbit gives a parallax of $\pi = 9.36 \pm 0.10$ mas, a value consistent with van Leeuwen (2007, $\pi = 9.54 \pm 0.21$ mas) but about 2-σ from the original Hipparcos reduction ($\pi = 10.12 \pm 0.43$ mas; ESA, 1997), confirmed by Pourbaix & Boffin (2003, $\pi = 10.27 \pm 0.42$ mas). Adopting the spectroscopic orbit presented here, the resulting Hipparcos parallax becomes $\pi = 10.15 \pm 0.43$ mas (Dimitri Pourbaix, private communication). The origin of the 2-σ discrepancy in parallax measurements is not well-understood; for our purposes in later sections, we proceed with our derived value of $\pi = 9.36 \pm 0.10$ mas.

Table 5.3. Orbital and Stellar Parameters of o Draconis

Measured Parameters	Value
semi-major axis, a (mas)	6.51 ± 0.03
eccentricity, e	0.158 ± 0.003
inclination, i (°)	89.6 ± 0.3
argument of periastron, ω (°)[a]	293.0 ± 0.6
ascending node, Ω (°, E of N)	22.9 ± 0.2
period, $P_{\rm orb}$ (days)	138.444 ± 0.003
time of periastron passage, T (HJD)	2454983.0 ± 0.2
velocity semi-amplitude, $K_{\rm A}$ (km s^{-1})	23.42 ± 0.05
velocity semi-amplitude, $K_{\rm B}$ (km s^{-1})	32.0 ± 0.4
system velocity, γ (km s^{-1})	-20.77 ± 0.04
H-band uniform disk diameter, $\theta_{{\rm UD},A}$ (mas)	2.115 ± 0.007
H-band limb-darkened disk diameter, $\theta_{{\rm LD},A}$ (mas)[b]	2.189 ± 0.007
primary major-to-minor axis ratio	1.01 ± 0.03
B-band flux ratio, primary-to-secondary	60 ± 20
V-band flux ratio, primary-to-secondary	130 ± 80
H-band flux ratio, primary-to-secondary	370 ± 40
rotational velocity, $v \sin i$ (km s^{-1})	16.0 ± 0.5
Derived Parameters	
orbital parallax, π (mas)	9.36 ± 0.10
distance, d (pc)	106.8 ± 1.1
primary radius, $R_{\rm A}$ ($R_\odot$)[c]	25.1 ± 0.3
primary luminosity, $L_{\rm A}$ ($L_\odot$)	220 ± 30
primary surface gravity, $\log g_{\rm A}$ (cm/s^2)	1.769 ± 0.007
primary mass, $M_{\rm A}$ ($M_\odot$)	1.35 ± 0.05
primary rotation period, $P_{\rm rot}$ (days)[d]	79 ± 3
secondary radius, $R_{\rm B}$ ($R_\odot$)	1.0 ± 0.1
secondary luminosity, $L_{\rm B}$ ($L_\odot$)	1.3 ± 0.2
secondary surface gravity, $\log g_{\rm B}$ (cm/s^2)	4.43 ± 0.09
secondary mass, $M_{\rm B}$ ($M_\odot$)	0.99 ± 0.02
secondary temperature, $T_{{\rm eff},B}$ (K)	6000^{+400}_{-300}
system age (Gyr)	3.0 ∓ 0.5
Literature Parameters	
primary effective temperature, $T_{{\rm eff},A}$ (K)[e]	4430 ± 130
primary metallicity, Fe/H[f]	-0.5

Note. — [a]Radial velocity convention for primary with respect to the center of mass.
[b]We applied a 3.5% correction from uniform to limb-darkened disk diameter, which is consistent with a limb-darkening power law exponent of $\alpha = 0.27$.
[c]Using limb-darkened disk diameter.
[d]Assuming $i_{\rm rot} = i_{\rm orb}$.
[e]$T_{{\rm eff},A}$ is an average of temperatures given by Christian & Janes (1977); Głębocki & Stawikowski (1977); Rutter & Schrijver (1987); Głębocki & Stawikowski (1988); McWilliam (1990); Luck (1991); Pourbaix & Boffin (2003); Böhm-Vitense (2004); Massarotti et al. (2008); Soubiran et al. (2010); McDonald et al. (2012). The 1-σ error is the standard deviation of these values.
[f][Fe/H] is approximated in stellar evolution models based upon values given by McWilliam (1990); Massarotti et al. (2008); Soubiran et al. (2010).

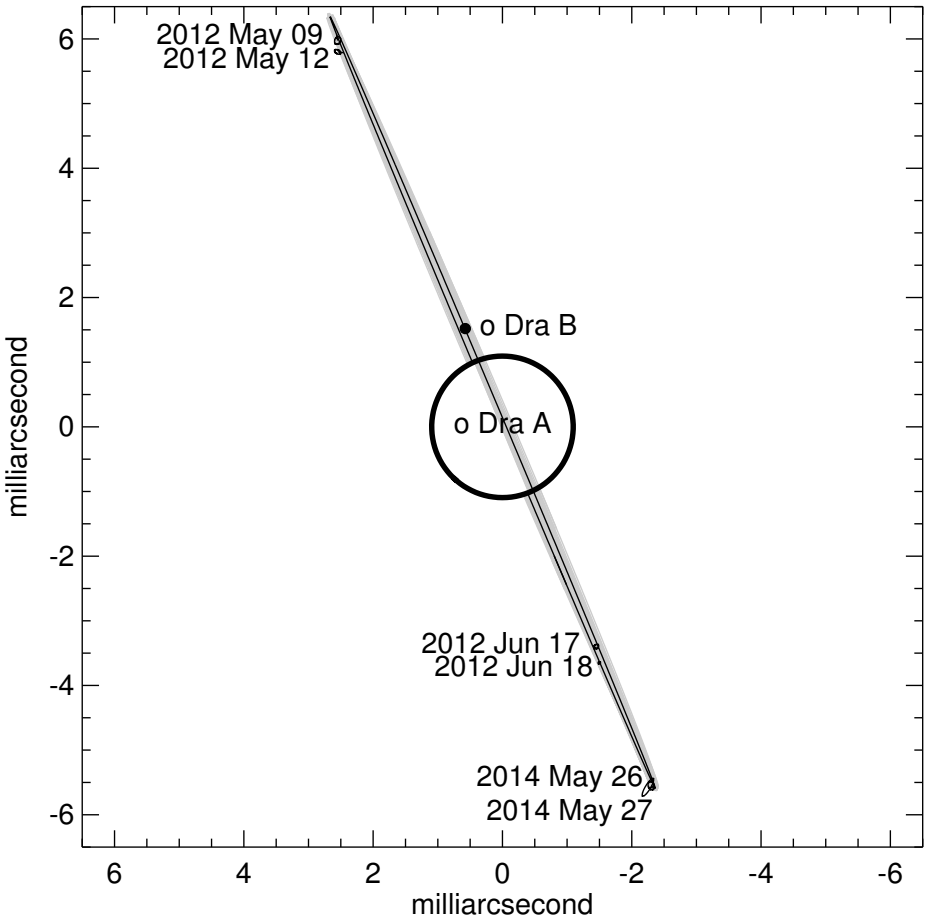

Figure 5.3: Visual orbit of the RS CVn system *o* Dra with our dates of companion detection and their locations on the orbit (black error ellipses). The observed stellar radius of the primary star is plotted with a thick black line (*o* Dra A). The radius of the companion star, *o* Dra B, for the best-fit temperature of 6000 K is plotted as the small black circle. The light gray orbits represent fifty Monte Carlo realizations. Black lines connect the center of the detection error ellipse to the expected point in the best-fit orbit, which is overlaid in black (given in Table 5.3 with 1-σ errors). At the southernmost point in the orbit, the secondary star is moving toward the observer. Note: the axis units are milliarcseconds (mas) with north upwards and east to the left.

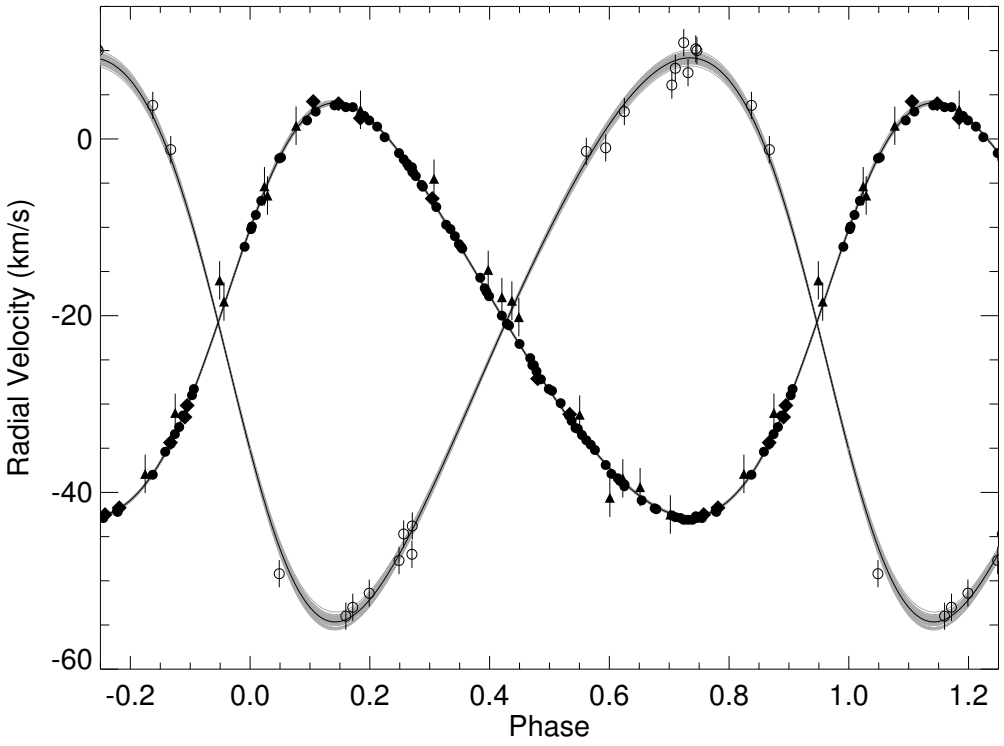

Figure 5.4: Radial velocity curves of the components of o Dra. The filled symbols represent measurements of the primary star. The filled diamonds represent observations from Massarotti et al. (2008)/CfA. The filled circles are the AST observations. The filled triangles are observations from Young (1921). 1-σ errors in velocity are plotted unless the error is smaller than the symbols. Similarly, the open circles represent AST radial velocity data for the secondary star with 1-σ error bars. The gray orbits are fifty Monte Carlo realizations (dark gray for the primary star and light gray for the secondary star) with the best-fit orbital parameters overlaid in black. See Table 5.3 for orbital parameters with 1-σ errors.

5.6 Light Curve Models and Ellipsoidal Variations

A previous study, Strassmeier et al. (1989), suggested *o* Dra has photometric variations up to $\Delta V \sim 0.01$ mag. Other indications of activity include chromospheric Ca H and K emission and variation (Young & Koniges, 1977; Simon & Fekel, 1987; Strassmeier et al., 1988). Hall & Persinger (1986) reported a possible rotation period of $P_{\rm rot} = 54.6$ days from photometric observations. Using our NOT spectra, we can determine the value of $v \sin i$. We modeled the Fe 6421 Å line with a variety of $v \sin i$ models from Castelli & Kurucz (2004) with $T_{\rm eff,A} = 4530$ K, $\log g_{\rm A} = 1.77$, [Fe/H]$= -0.5$, microturbulence $\xi_{\rm m} = 1.4$ km s^{-1}, and macroturbulence $\xi_{\rm M} = 6$ km s^{-1}. The resultant value is $v \sin i = 16 \pm 0.5$ km s^{-1} when combined with our observed primary radius and orbital inclination (assuming $i_{\rm orb} = i_{\rm rot}$) gives $P_{\rm rot,A} = 79 \pm 3$ days.

We investigate the APT Johnson B and V differential light curves for evidence of starspots. We removed long-term variations ($\Delta V \sim 0.02$) that may be attributed to axisymmetric spot structures or polar spot structures. We folded the adjusted light curves over the orbital period ($P_{\rm orb} = 138.444$ days) and binned the data (0.01 in phase). The resultant Johnson B and V light curves are presented in Figure 5.5. The quasi-sinusoidal trend observed in the averaged light curves suggests ellipsoidal variations due to distortions of the primary star partially filling its Roche lobe potential ($R_{\rm L} = 60.8\ R_{\odot}$, $R_A/R_{\rm L} = 0.42$; e.g., Chapter IV). Both light curves clearly show an eclipse (phase ~ 0.95) and evidence of a weak eclipse (phase ~ 0.40). Comparing the timing of the eclipses to the radial velocity curve and visual orbit, we see that the deeper eclipse is associated with the secondary star moving behind the primary star, revealing that the secondary star is hotter than the primary star.

The secondary eclipse provides flux ratios for Johnson B and V bands (60 ± 20 and 130 ± 80, respectively). Using the H- and B-band flux ratios, we are able to constrain the temperature of the companion star. We use NextGen stellar atmospheres (Hauschildt et al., 1999) restricted to the bandpasses with the size and tem-

perature of the primary star to determine the secondary star's effective temperature ($T_{\rm eff,B} = 6000^{+400}_{-300}$ K), radius ($R_{\rm B} = 1.0 \pm 0.1\ M_{\odot}$), luminosity ($L_{\rm B} = 1.3 \pm 0.2\ L_{\odot}$), and surface gravity ($\log g_{\rm B} = 4.43 \pm 0.09$ (cm s^{-2})).

To model the observed ellipsoidal variations, we used the light-curve-fitting software package Eclipsing Light Curve (ELC; Orosz & Hauschildt, 2000). ELC accurately accounts for the star's ellipsoidal shape which changes as the companion star moves along its eccentric orbit. We begin by modeling the light curves with no free parameters. We assume that the orbital and rotational axes are aligned ($i_{\rm orb} = i_{\rm rot}$, $P_{\rm rot} = 79$ days), although our results are not sensitive to the assumed $P_{\rm rot}$. We assume gravity darkening to be $\beta = 0.08$ (Lucy, 1967). The ellipsoidal variations from the modeled light curves agree remarkably well with the observed light curve of o Dra confirming that the coherent quasi-sinusoidal signature is due to ellipsoidal variations (see Figure 5.5).

The long-term variations, ellipsoidal variations, and eclipses account for much of the large changes in the light curves, suggesting that the previously identified starspots (e.g., Hall & Persinger, 1986; Strassmeier et al., 1989) were instead observations of a combination of these effects. Additionally, the absorption lines of the NOT spectra do not show clear evidence of rotationally-modulated temperatures due to starspots (see Figure 5.6).

However, weak spot signatures are occasionally still visually present after removing the eclipse and ellipsoidal variation model from the observed light curve. To determine a rotational period based on the spot signature, we perform a power spectrum analysis in which we sampled the light curve on a grid of one-day spacing (inserting 0.0 on days without data). We found the strongest signature comes from a period of $P_{\rm rot} = 75$ days (see Figure 5.7), slightly smaller than the estimated 79-day period based upon $v \sin i$. While $P_{\rm rot} = 75$ days is within 2σ from the spectroscopically determined rotation period, this small difference could be attributed to differential

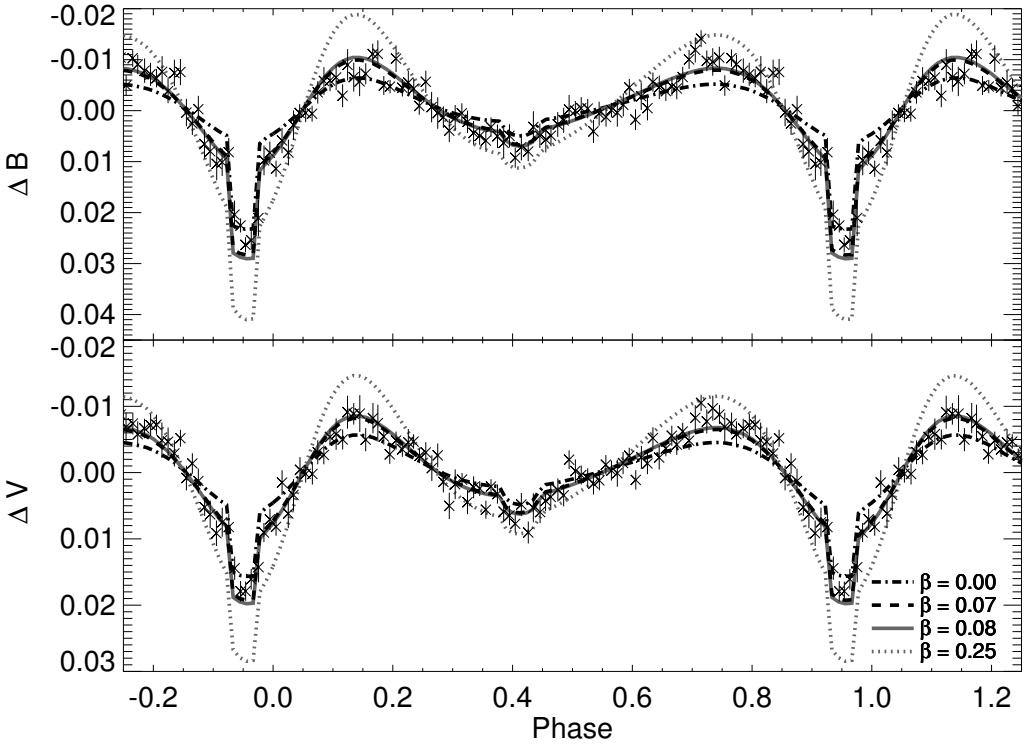

Figure 5.5: Differential folded and binned light curves of o Dra for B and V magnitudes plotted with error bars from the binning. Each data point is an average of data points spanning 0.01 in phase from the complete light curve folded on the orbital period. The quasi-sinusoidal signature of the averaged light curve is due to ellipsoidal variations caused by the primary star partially filling its Roche lobe potential. The lines represent the ELC models for ellipsoidal variations with the gravity darkening coefficient $\beta = 0.00$, 0.07, 0.08, and 0.25, where $\beta = 0.07 \pm 0.03$ is the best fit to the binned light curves.

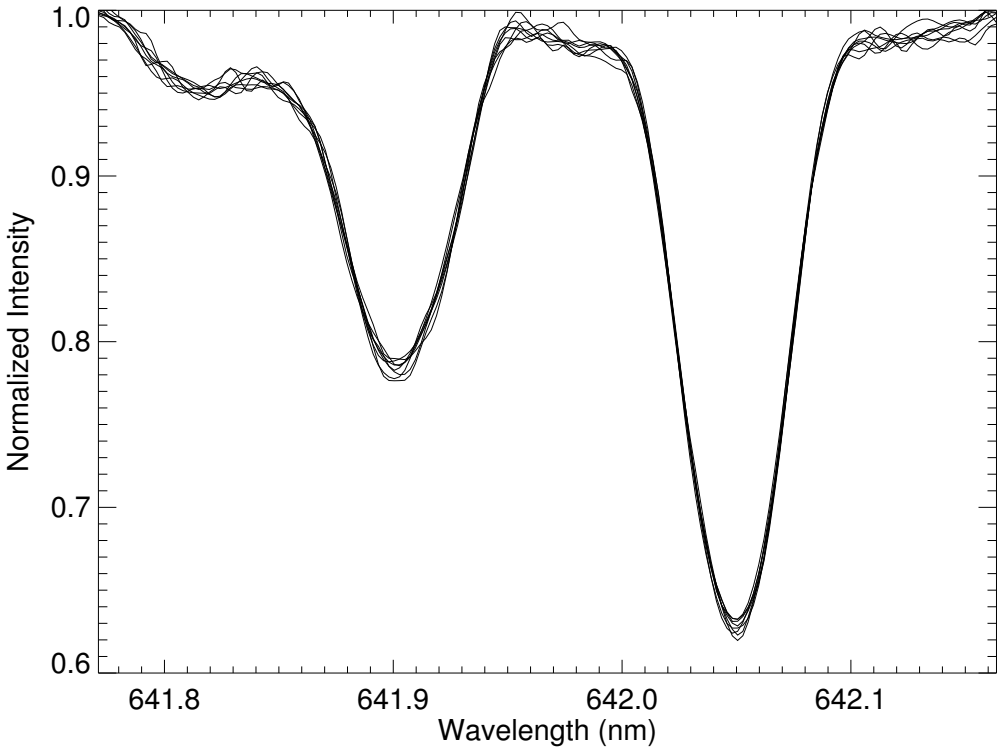

Figure 5.6: Portion of the *o* Dra spectrum containing two Fe I (6419 and 6421 Å) lines. Eight spectra are over-plotted spanning JD 2012 April 17 − August 15, approximately two rotation periods. Starspots moving across the stellar surface will manifest as features moving through some absorption lines. While the lines deviate from Gaussian profiles, throughout the rotation of *o* Dra, the absorption line cores do not vary in a periodic way, suggesting a featureless surface.

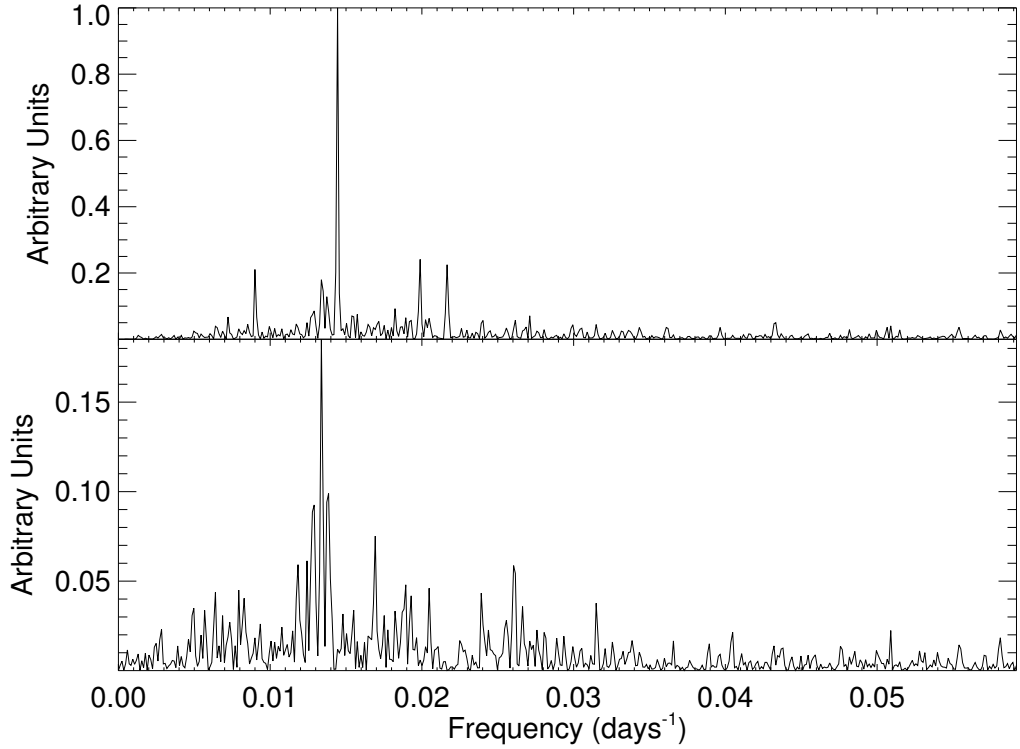

Figure 5.7: Power spectrum of the Johnson B light curve of o Dra. In the top panel, power spectrum of the B light curve with the long-term trend removed shows a peak at half the orbital period (69.2 days), consistent with the signature of ellipsoidal variations. In the bottom panel, the power spectrum of the B light curve with the long-term trend, eclipses, and ellipsoidal variations removed shows a peak at 75 days.

rotation, often seen with RS CVn stars (Strassmeier, 2009).

Because the starspots are relatively weak, they do not strongly contaminate the phase-averaged light curve of o Dra, providing an opportunity for precision analysis. Using ELC, we measured the level of gravity darkening by modeling the system with no free parameters except the gravity darkening coefficient, β from $T_{\rm eff} \propto g^{\beta}$ (von Zeipel, 1924). We found that the best-fit gravity darkening coefficient for o Dra is $\beta = 0.07 \pm 0.03$ (errors from bootstrapping over observational seasons), similar to recent findings of Djurašević et al. (2006, $\beta = 0.06 \pm 0.01$) and Chapter IV ($\beta < 0.1$). These measurements are consistent with the canonical value $\beta \sim 0.08$ from Lucy

(1967), but differs from an alternative value $\beta \sim 0.21$ from Espinosa Lara & Rieutord (2012).

5.7 Hertzsprung-Russell Diagram and Evolutionary History

To understand why o Dra has $P_{\rm rot} < P_{\rm orb}$, we investigate the evolution of the present stellar components. We plot the location of the components of o Dra on an H-R diagram (see Figure 5.8) using our measured stellar parameters determined from our orbit and flux ratios. We include the zero-age main sequence and Dartmouth stellar evolutionary tracks (Fe/H $= -0.5$, α/Fe $= 0.0$, PHOENIX-based models, Dotter et al., 2008) for interpolated model masses ($M_{A,\rm model} = 1.35 \pm 0.05\ M_{\odot}$, $M_{B,\rm model} = 0.99 \pm 0.02\ M_{\odot}$).

Our primary star detection falls on the 1.35 $M_{\odot}$ evolutionary track with an estimated temperature of 4430±130 K (Christian & Janes, 1977; Głębocki & Stawikowski, 1977; Rutter & Schrijver, 1987; Głębocki & Stawikowski, 1988; McWilliam, 1990; Luck, 1991; Pourbaix & Boffin, 2003; Böhm-Vitense, 2004; Massarotti et al., 2008; Soubiran et al., 2010; McDonald et al., 2012). The detection of the secondary with 1-σ errors cross the main sequence of the expected evolutionary track, but at the upper limit of our temperature range ($T_{{\rm eff},B} = 6000^{+400}_{-300}$ K). Our system age estimate most strongly depends upon the mass of the primary star; for the primary mass ($M_{A,\rm model} = 1.35 \pm 0.05\ M_{\odot}$), we determine an age of the system of 3.0 ∓ 0.5 Gyr.

We can use our knowledge of the evolutionary state of o Dra to investigate three possible explanations why the rotational period is faster than its orbital period. First, we conclude that the star could not have evolved right off of the main sequence. The rotational velocity is more rapid than expected (~ 3 km s^{-1}) for the evolution of a 1.35 $M_{\odot}$, early F main sequence star (based upon initial rotational periods of ~ 2 days and main-sequence radius of $\sim 2\ R_{\odot}$; Nielsen et al., 2013; Boyajian et al., 2012b). Another component of the system must have imparted some angular momentum.

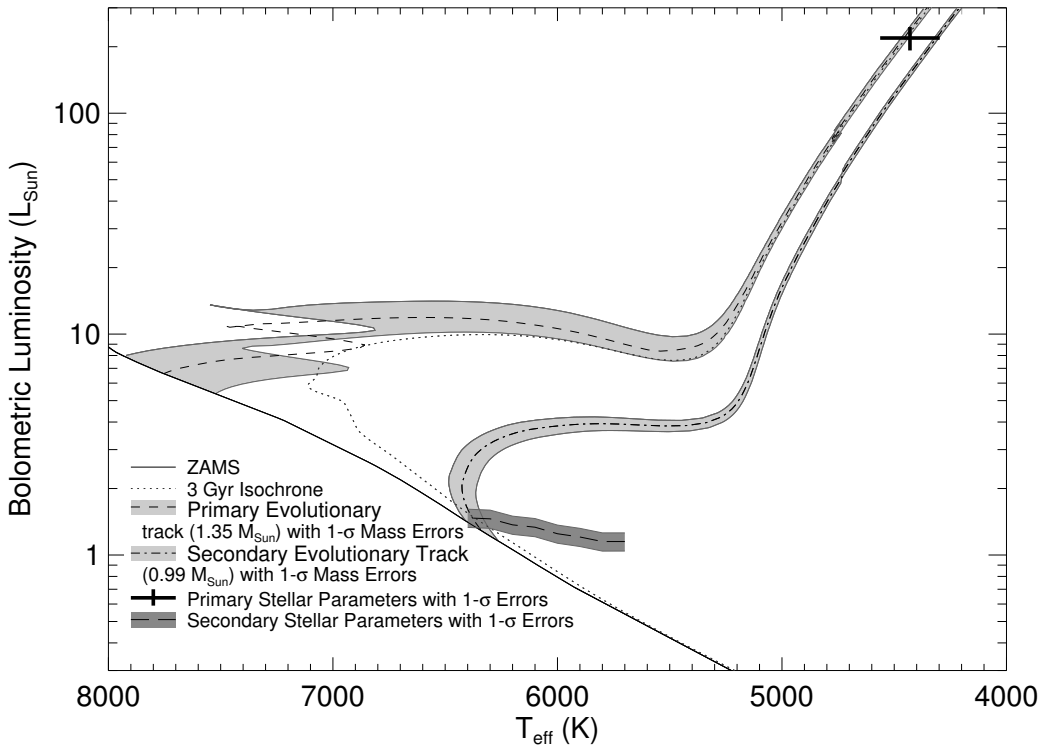

Figure 5.8: H-R diagram for o Dra. The dashed and dot-dashed lines are the main sequence and post-main sequence evolutionary tracks for 1.35 $M_{\odot}$ and 0.99 $M_{\odot}$ stars with $[Fe/H] \sim -0.5$, respectively (Dotter et al., 2008). The gray regions represent our 1-σ mass errors with the solid black line representing the zero age main sequence. The dotted line is a 3 Gyr isochrone (PHOENIX; Dotter et al., 2008). The measured location of the primary with 1-σ errors is indicated by the plus sign. The companion location is indicated with the long-dashed line (with 1-σ errors in luminosity).

Second, secondary stars can spin-up primary stars faster than the orbital period in the case of eccentric orbits. Pseudosynchronous orbits are those that have the rotation of the star synchronized with the periastron passage of the secondary star (Hut, 1981). *o* Dra has a predicted pseudosynchronous rotation period of $P_{\rm ps} = 123.3 \pm 2.3$ days (Hall, 1986), which is much longer than our observed rotational period. Thus, the known companion of *o* Dra could not have spun up the system to its current rotational period.

Third, a now-unseen companion could have spun-up the primary star. Because the secondary star has a mass of $M_{\rm B} = 0.99 \pm 0.02\ M_{\odot}$, the two objects that merged would have to have a significant difference in mass, otherwise the secondary star would be more evolved than the primary. With the primary and secondary stars falling on the same isochrone, the component that merged into the primary must have been only a small fraction of primary mass so as to not significantly affect its evolution. In order be consistent with rotational velocity observations, sufficient angular momentum would need to be imparted by the merging component to spin-up the $\sim 1.04\ M_{\odot}$ convective envelope of the $1.35\ M_{\odot}$ primary star[1]. Unfortunately, the rotation period of the star when the companion was engulfed is unknown and the primary star could have since slowed. While we cannot accurately estimate the mass of the consumed companion, we find from angular momentum arguments that the companion could range in mass from a giant planet to a low-mass star. If a low-mass companion were initially present in the system at 0.1 AU, it would be dynamically stable with the system's stellar components on the timescale of the system age, 3 Gyr, but would be engulfed by the primary star as the evolving stellar radius approached the companion's orbital radius (cf. David et al., 2003).

[1]The mass of the convective envelope was determined using EZ-Web, `http://www.astro.wisc.edu/~townsend/static.php?ref=ez-web`, R. H. D. Townsend's Web-browser interface of the Evolve ZAMS evolution code (Paxton, 2004)

5.8 Conclusions

In this work, we have made the first visual detections of the secondary star of o Dra using interferometric observations. The H-band primary-to-secondary flux ratio is 370 ± 40, the highest confirmed flux ratio for a binary detected with long-baseline optical interferometry. With the astrometry and radial velocity data for both stars, we establish the first full three-dimensional orbit to determine orbital and stellar parameters.

By folding and binning photometric data, we have shown evidence of ellipsoidal variations, gravitational distortions of the primary star caused by the close companion. The observed light curves are nearly identical to light curve models generated only from stellar and orbital parameters leading to the conclusion that the primary star has ellipsoidal variations, as opposed to long-lived starspots or active longitudes. After removing the model light curve, we observe only weak signs of rotationally-modulated starspots. Additionally, there could be potentially active regions (e.g., axisymmetric spot structures and polar spots) that affect the stellar flux over longer periods of time with a global brightening or dimming. The folded, binned light curve also shows primary and secondary eclipses, which provide flux ratios to help constrain the stellar parameters of the secondary star.

Our new, high-precision orbital elements along with the folded light curve also allow for a measurement of gravity darkening. We find that $\beta = 0.07 \pm 0.03$, a value of gravity darkening consistent with conventional theory (Lucy, 1967) and previous results (Djurašević et al., 2006, Chapter IV).

We have established that the primary star's rapid rotation period could be due to the transfer of angular momentum from a nearby companion. Specifically, a low-mass companion in a 0.1 AU orbit would impart sufficient angular momentum to spin-up the outer stellar layers before being engulfed as the star ascended the giant branch while not dramatically altering the stellar evolution.

CHAPTER VI

Imaging Global Spot Networks on ζ And, a Magnetically-Active Star

6.1 Preface

This chapter is adapted from work of the same title under review for *Nature*. This work is coauthored by John D. Monnier, Heidi Korhonen, Alicia N. Aarnio, Fabien Baron, Xiao Che, Robert O. Harmon, Zsolt Kővári, Stefan Kraus, Gail H. Schaefer, Guillermo Torres, Ming Zhao, Theo A. ten Brummelaar, Judit Sturmann, and Lazslo Sturmann.

For this work, I obtained all of the 2013 observations and reduced all of the nights of data. I attempted to search for the companion of ζ And and was unsuccessful. I worked closely with Prof. Monnier on the ζ And figures included here. I was successful in finding the companion of the calibrator star 37 And. For 37 And, I combined these detections with radial velocity data (single-lined orbit) to measure the system's orbital parameters. Additionally, I made the 37 And figures, the interferometric observation figures, and the data tables, as well as wrote the text.

6.2 Abstract

Astronomers estimate stellar masses and ages from accurate measurements of temperature and luminosity (Torres et al., 2010). These observed properties can be affected by the presence of strong magnetic fields (Stassun et al., 2007). As observed on the Sun, strong magnetic fields stifle convection, creating localized regions of decreased temperatures (Strassmeier, 2009). These "starspots" are notoriously difficult to accurately image on stars besides the Sun using traditional methods, limiting our understanding of their effects on stellar properties. Here we show direct imaging using long-baseline infrared interferometry of a magnetically-active star that exhibits extended dark regions that we interpret as caused by suppressed convection on a global scale. The interferometrically observed large-scale surface darkenings, including a "polar spot," are confirmed here, having been suggested using other less-direct imaging techniques. Our new imaging results definitively establish that strong large-scale magnetic fields in highly active stars can alter their apparent "fundamental" properties and must be accounted for in theories of stellar evolution (Somers & Pinnsoneault, 2015).

6.3 Introduction

To accurately characterize stars with stellar models, measurements of fundamental parameters such as stellar luminosity and effective temperature are used to estimate mass and age (Torres et al., 2010). Previous studies (Stassun et al., 2007; Somers & Pinnsoneault, 2015) have shown that the stellar luminosity and effective temperatures do not uniquely map to mass and age estimates, but rotation and magnetic fields must also be considered. This is important especially for young stars where rotation and stellar activity are both high, likely impacting measurements of stellar parameters (Hillenbrand & White, 2004; Somers & Pinnsoneault, 2015).

Stellar activity can manifest as cool regions of stifled convection where strong magnetic fields prevent efficient energy transport (Berdyugina, 2005). These regions are most easily observed as starspots—large, unresolved groups of small spots, analogous to sunspots. Large spots covering a substantial fraction of the stellar surface have been suggested to cause inflated stellar radii and decreased effective temperatures and luminosities (Somers & Pinnsoneault, 2015). These surface features can be indirectly imaged using techniques such as light curve inversion and Doppler imaging techniques (Kiurkchieva, 1989; Vogt & Penrod, 1983). Light curve inversion reproduces spotted stellar surfaces based on time-series data and can only reproduce structures observed as rotational modulations—structures such as static polar spots are practically invisible to light-curve inversion imaging. Light curve inversion typically reveals only weak relative latitude information for the spots, although this can be improved with the combination of concurrent observations in multiple filters (Harmon & Crews, 2000). A more detailed surface map, both in latitude and longitude, can be obtained with Doppler imaging, which creates surface temperature maps from tracking small changes in absorption lines as starspots rotate in and out of view. Still, this method cannot always distinguish the hemisphere in which the structures are located. In order to confirm the important findings from these methods and to firmly understand global characteristics of activity that can alter stellar radii and effective temperature, a more direct imaging method is required that is immune to these ambiguities.

The nearest magnetically-active stars are too small to be resolved by even our largest telescopes. However, long-baseline interferometry has the potential to image sub-milliarcsecond features on the surfaces of nearby stars. To date, interferometric imaging has been successfully used to confirm the oblateness and gravity darkening of rapidly-rotating stars (Monnier, 2007) and even to image a spotted stellar surface (Parks et al., submitted). To improve the resolution and imaging quality for rotating stars that show strong magnetic activity, we debut here an "imaging-on-a-sphere"

technique that uses interferometer observations from multiple nights to constrain a surface temperature map. This naturally takes advantage of the multiple views we have of starspot structures as they rotate across the disk of the star.

6.4 Observations

We chose the nearby spotted star ζ Andromedae (ζ And, HD 4502) as our prime imaging target. ζ And is an RS CVn binary system, consisting of a K-type cool giant and an unseen lower-mass companion star (Kővári et al., 2007a). Tidal interactions have spun-up the cool primary component, causing unusually strong starspot and magnetic activity (Berdyugina, 2005; Strassmeier, 2009). The system appears tidally-locked with a circular orbit ($e = 0.00$) of period $P_{\rm orb} = 17.769426 \pm 0.00004$ days ($T_{0,\rm HJD} = 2449992.7810 \pm 0.0170$; Fekel et al., 1999). Previous studies have identified the star as an ellipsoidal variable due to the giant primary star partially filling its limiting Roche surface, slightly distorting it from spherical (major-to-minor axis ratio ~ 1.04; Kővári et al., 2007a; Korhonen et al., 2010).

We observed ζ And during observing campaigns of eleven nights spanning UT 2011 Jul 9-22 and fourteen nights spanning UT 2013 September 12-30 (see Table 6.1 and Appendix F) with the Michigan InfraRed Combiner (MIRC) at Georgia State University's Center for High Angular Resolution Astronomy (CHARA) Array on Mount Wilson, CA, USA. CHARA consists of six 1-m telescopes in a Y-shaped configuration with baselines ranging from 34 to 331 m (ten Brummelaar et al., 2005). For the ζ And data, MIRC (Monnier et al., 2004) combined light from all six CHARA telescopes in the H-band (eight channels across $1.5-1.8$ μm for $\lambda/\Delta\lambda \sim 40$), resulting in an angular resolution of $\lambda/2B \sim 0.5$ milliarcseconds. The data were reduced and calibrated with the standard MIRC pipeline (Monnier et al., 2012). We searched without success for evidence of the faint companion in our interferometry data using our proven grid search method (see Chapters IV and V), and could only secure a lower limit of 300:1

Table 6.1. Observation Dates and Calibrators of ζ Andromedae

UT Date	Modified Julian Date (MJD)	Calibrators Used
2011 Jul 9	55751.536	37 And
2011 Jul 10	55752.531	γ Peg
2011 Jul 11	55753.480	37 And
2011 Jul 12	55754.469	γ Peg
2011 Jul 14	55756.478	γ Peg
2011 Jul 16	55758.505	58 Oph
2011 Jul 17	55759.481	γ Peg
2011 Jul 19	55761.475	37 And, γ Peg
2011 Jul 20	55762.517	γ Peg
2011 Jul 21	55763.478	γ Peg, γ Tri
2011 Jul 22	55764.480	γ Peg, γ Tri
2013 Sep 12	56547.449	37 And, γ Tri
2013 Sep 13	56548.426	37 And, γ Tri
2013 Sep 15	56550.392	37 And, γ Peg, γ Tri
2013 Sep 16	56551.365	37 And, γ Peg, γ Tri
2013 Sep 17	56552.345	37 And, γ Tri
2013 Sep 18	56553.359	37 And, γ Peg, γ Tri
2013 Sep 19	56554.407	37 And, γ Peg, γ Tri
2013 Sep 20	56555.365	37 And, γ Peg, γ Tri
2013 Sep 21	56556.403	37 And, γ Tri
2013 Sep 23	56558.403	37 And, γ Tri
2013 Sep 24	56559.343	37 And, γ Peg, γ Tri
2013 Sep 28	56563.367	37 And, γ Tri
2013 Sep 29	56564.357	37 And, γ Tri
2013 Sep 30	56565.334	37 And, γ Tri

on the H-band flux ratio between primary and companion.

6.4.1 Calibration Stars

The twenty-five nights of interferometric data span 2011 July 9-22 and 2013 September 12-30. For these nights of observation we use four calibration stars (37 And, γ Peg, γ Tri, and 58 Oph) interspersed with observations of the target star ζ And. γ Peg, γ Tri, and 58 Oph are modeled as spherical, uniform disk stars (Bonneau et al., 2006) with their parameters included in Table 6.2.

The calibrator 37 And is a recently-discovered binary system (Baron et al., 2014) with primary-to-secondary H-band flux ratio of 80 ± 20. Ordinarily, binary stars make poor calibrators, but 37 And system was observed enough times to determine its orbit precisely and salvage its use for calibrating our primary target ζ And. We detect the companion of 37 And in nineteen nights of data (see Table 6.3) using a grid

Table 6.2. Calibration star uniform disk sizes

Star Name (HD number)	$\theta_{\rm UD}$ (mas)
γ Peg (HD 886)	0.41 ± 0.03
γ Tri (HD 14055)	0.51 ± 0.03
58 Oph (HD 160915)	0.68 ± 0.05

Note. — Uniform disk sizes (H-band) of calibrators used. The uniform disk diameters were obtained with SearchCal (Bonneau et al., 2006)

search for the companion. To constrain orbital parameters, we combined the visual orbit with the primary star's radial velocity curve obtained with archival spectra from the ELODIE high-resolution échelle spectrograph formerly on a 1.93-m telescope at Observatoire de Haute-Provence, France (Moultaka et al., 2004). Figures 6.1 and 6.2 show the system orbit and radial velocity curve and Table 6.4 contains the system orbital parameters. The orbital parameters are used in the MIRC calibration pipeline to account for the effect of the companion of 37 And.

Table 6.3. Binary separation and position angle measurements of 37 Andromedae

UT Date	Modified Julian Date (MJD)	Separation (mas)	Position Angle (° E of N)	Error Ellipse Major Axis (mas)	Error Ellipse Minor Axis (mas)	Error Ellipse Position Angle (°)
2011 Jul 9	55751.492	11.46	217.0	0.13	0.11	300
2011 Jul 12	55754.499	9.09	230.6	0.10	0.08	270
2011 Jul 19	55761.465	6.38	295.4	0.06	0.05	330
2011 Nov 29	55894.159	63.57	143.9	1.82	0.16	340
2013 Sep 12	56547.470	82.28	152.6	0.58	0.15	330
2013 Sep 13	56548.399	82.51	152.7	0.02	0.10	30
2013 Sep 15	56550.340	82.47	152.8	0.81	0.26	350
2013 Sep 16	56551.344	82.73	152.9	1.23	0.27	340
2013 Sep 17	56552.329	82.63	152.9	0.48	0.17	330
2013 Sep 18	56553.250	82.88	153.0	0.95	0.21	340
2013 Sep 19	56554.292	83.06	153.1	0.72	0.27	350
2013 Sep 20	56555.301	83.02	153.2	0.79	0.14	330
2013 Sep 23	56558.416	83.08	153.4	1.01	0.22	340
2013 Sep 24	56559.239	83.29	153.5	0.58	0.23	340
2013 Sep 28	56563.303	83.62	153.7	1.08	0.21	340
2013 Sep 30	56565.276	83.65	153.8	0.83	0.20	340
2014 Aug 19	56888.422	14.45	98.2	0.32	0.18	280
2014 Aug 20	56889.446	15.58	100.8	0.24	0.17	10
2014 Sep 1	56901.412	22.82	116.9	0.11	0.07	300

Table 6.4. Orbital parameters of 37 Andromedae

Parameter	Value
Semimajor axis, a (mas)	46.66 ± 0.06
Eccentricity, e	0.8405 ± 0.0009
Inclination, i (°)	52.5 ± 0.3
Argument of periastron, ω (°)	168.9 ± 0.3
Ascending node, Ω (°)	-17.6 ± 0.2
Orbital period, $P_{\rm orb}$ (days)	550.7 ± 0.2
Time of periastron passage, T_0 (MJD)	55765.45 ± 0.04
Velocity semi-amplitude, $K_{\rm A}$ (km/s)	11.1 ± 0.5
System velocity, γ (km/s)	5.33 ± 0.07

6.5 Analysis and Results

The 2011 and 2013 datasets were separately imaged onto a prolate ellipsoid via the imaging software SURFING (SURFace ImagING), an aperture synthesis imaging technique (Monnier et al., in prep.). This novel approach replicates the fundamental ideas behind Doppler imaging in that the whole data set is mapped onto the rotating surface at once instead of night-by-night snapshots. Treating all of the data as an ensemble also allows SURFING to fit stellar and orbital parameters (see Table 6.5) along with the surface temperature maps (see Figures 6.3 and 6.4). To convert H-band intensities from the reconstructed images into photospheric temperatures, we utilized Kurucz atmospheric models (Kurucz, 1979) for $[Fe/H] = -0.25$ and appropriate $\log g$. Note that the overall temperature scale in our maps is uncertain (overall multiplicative scaling) due to lack of coeval photometry at H-band; here we adopted mean H-band mag 1.64 based on archival infrared photometry.

The surface temperature maps for ζ And show peaks of 4530 K and 4550 K and minimum values of 3540 K and 3660 K in 2011 and 2013, respectively. The ~ 900 K range of temperatures we see across the surface is slightly larger than the ~ 700 K found from recent Doppler imaging work (from the Fe I 6430 Å line). A strong dark polar spot is present in both of our imaging epochs, also consistent with recent Doppler imaging studies (Kővári et al., 2007a; Korhonen et al., 2010; Kővári et al.,

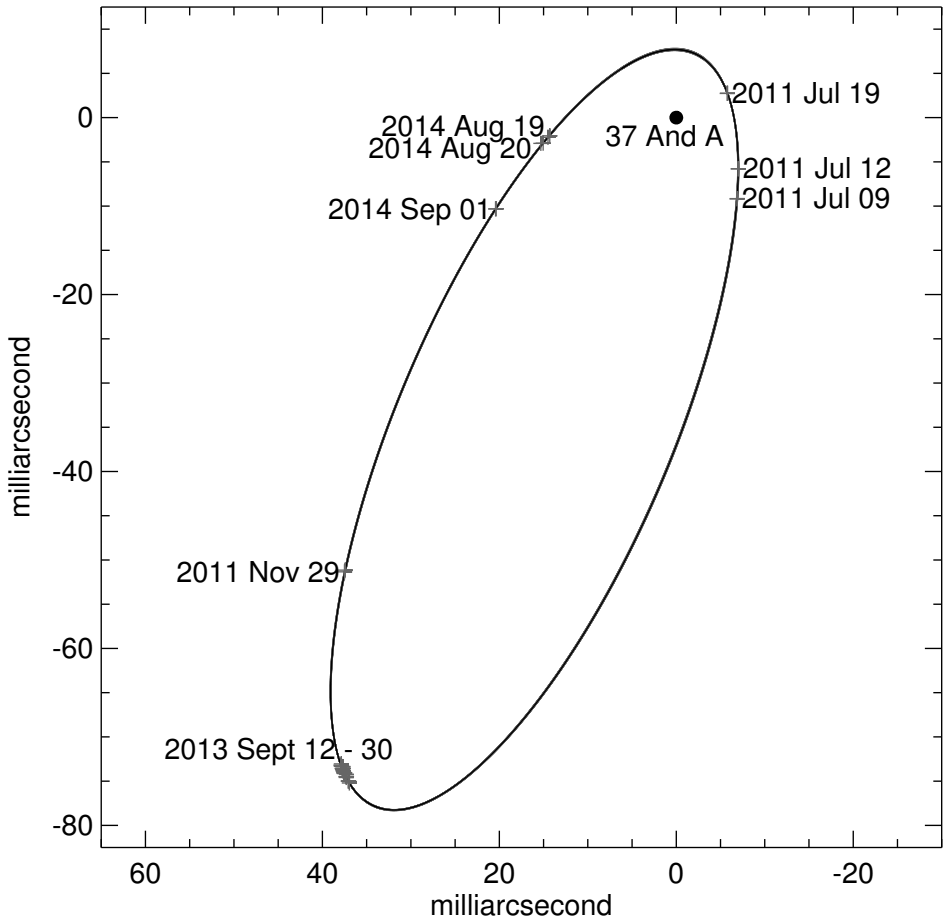

Figure 6.1: Orbit of 37 And. The gray plus signs represent measurements of the companion (errors on detections are smaller than the symbols). The observed resolved disk of 37 And is plotted as the black dot at the origin. The thin solid black line is the best-fit orbit from combining the interferometric detections and the ELODIE radial velocities. Note: the axis units are milliarcseconds (mas) with north up and east to the left.

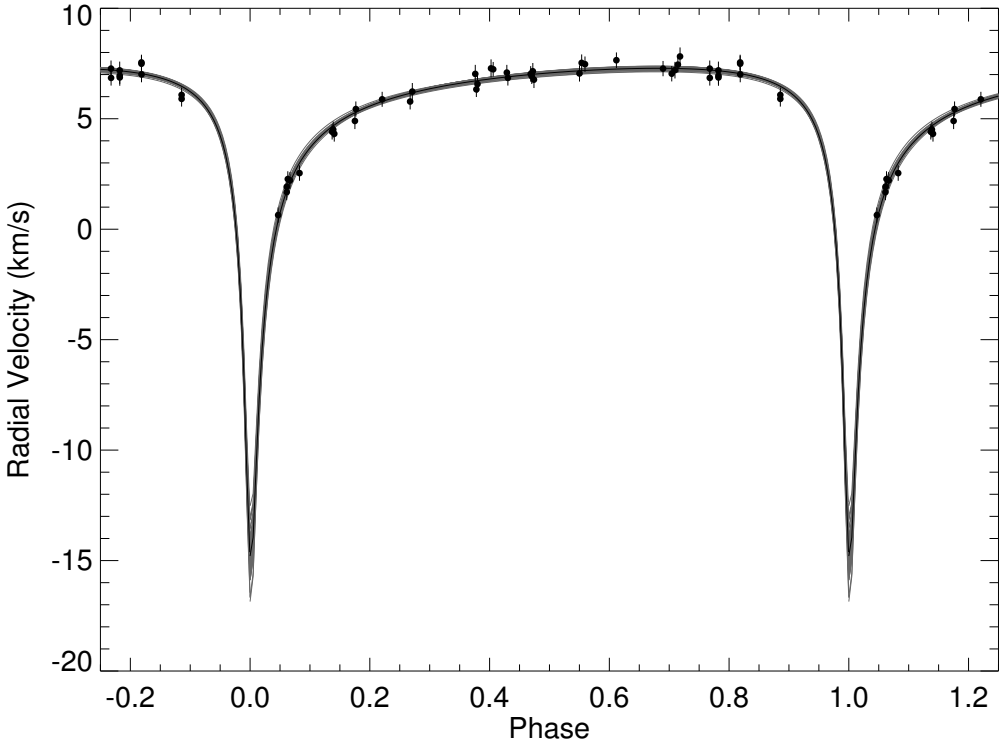

Figure 6.2: Radial velocity curve of the primary star of 37 And. The data points are based upon archival ELODIE spectra. The orbital solution used the velocity measurements and the interferometric measurements simultaneously. The solid line is the best-fit orbit and the gray lines are fifty Monte Carlo realizations of the orbit.

Table 6.5. Parameters of ζ Andromedae from SURFING

Parameter	SURFING Value
Angular diameter, $\theta_{\rm LD}$ (mas)	2.502 ± 0.008
Oblateness (major to minor axis) ratio	1.060 ± 0.011
Inclination, i (°)	70.0 ± 2.8
Pole Position Angle (°, E of N)	126.0 ± 1.9

Note. — SURFING models assumed circular orbit ($e = 0$) using circular radial velocity conventions with an orbital period $P_{\rm orb} = 17.7694260 \pm 0.00004$ days and time of nodal passage $T_0 = 49992.281 \pm 0.017$ (MJD; Fekel et al., 1999). Limb darkening was held fixed with power-law exponent $\mu = 0.269$, appropriate for ζ And based upon spectral type.

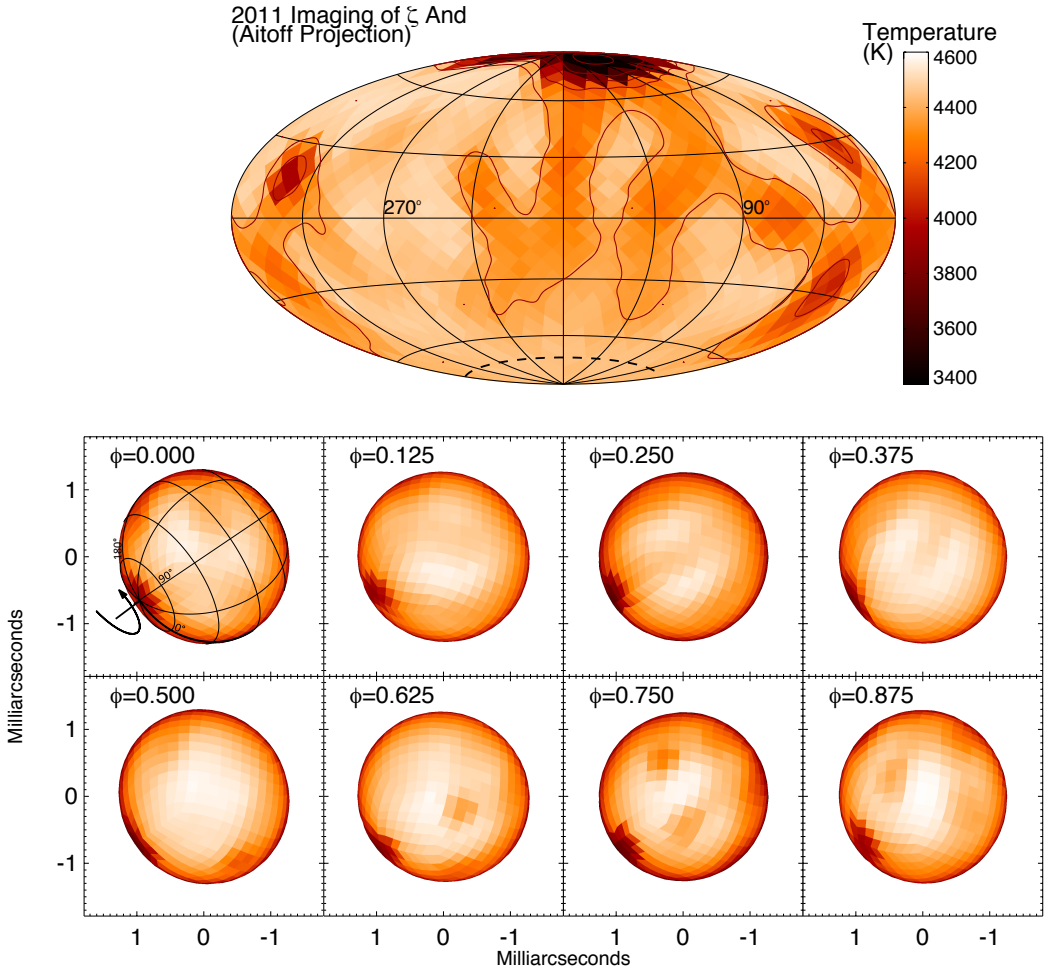

Figure 6.3: Surface image of ζ And from 2011 July with eleven nights of data. Using SURFING, the interferometric data of the rotating star were imaged together to recreate the stellar surface. In the upper plot, the temperature of ζ And is presented in an Aitoff projection of the entire surface. The contours represent every 200 K from 3400-4600 K. The dashed line at the bottom pole is hidden due to inclination. In the bottom eight panels, the surface reflects how the star is observed on the sky with H-band intensities. The $\phi = 0.000$ plot shows longitude 0° at the bottom of the star with 90° across the middle. The phases of the hemispheres are listed in the upper left of each plot. The phases assume circular orbit radial velocity conventions.

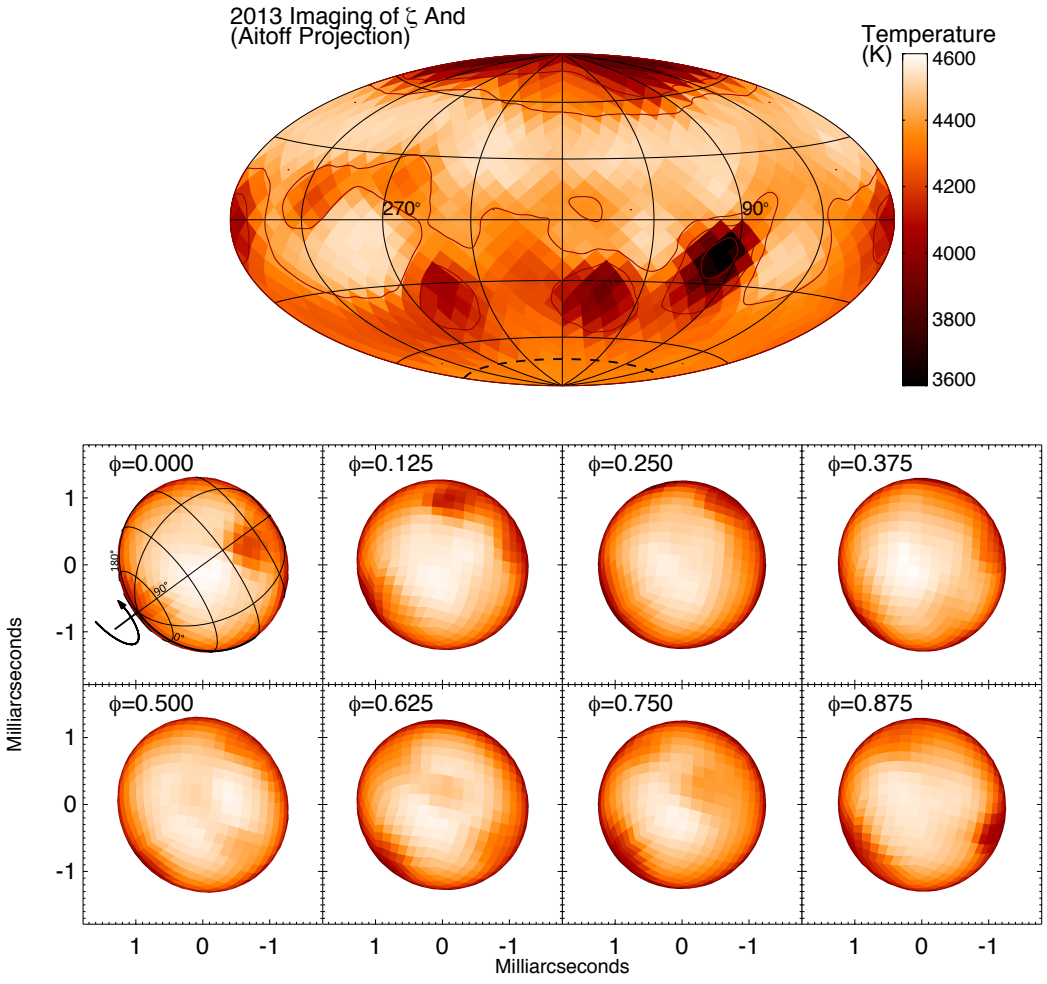

Figure 6.4: Surface images of ζ And from 2013 September using fourteen nights of data. These images are presented as in Figure 6.3, except the contours of the Aitoff projection range from 3600-4600 K.

2012). In contrast to this persistent feature, many other large dark regions completely change from 2011 to 2013 with no apparent overall symmetry or pattern. These new features and their locations are only unambiguously imaged by interferometry, and we now discuss their implications on the dynamical large-scale magnetic field of ζ And.

The extended network of cool regions stretching across the star suggest that strong magnetic fields can suppress convection on global scales, not just locally. The observations in hand lend support to studies that have suggested magnetic activity can be so widespread as to alter the apparent fundamental parameters of a star (Spruit, 1982; López-Morales, 2007). For example, a larger region of suppressed convection gives a lower observed temperature and luminosity, leading to inaccurate estimates for stellar mass and age (Somers & Pinnsoneault, 2015). The degree and physical extent of the global magnetic suppression change over time making photospheric temperature measurements time-variable. The changes in the global magnetic structures (at all latitudes) will produce long-term photometric variations that are often only attributed to changes in a growing or shrinking polar starspot. We note that a polar starspot for ζ And does not affect the flux of the star as significantly as global magnetic structures due to the effects of limb darkening and foreshortening on this highly inclined system ($i \sim 70.0^{\circ}$).

The interferometric images of ζ And provide a clear confirmation of the existence of polar spots. Polar spots have been seen in basically all of the Doppler images of ζ And Kővári et al. (2007a); Korhonen et al. (2010); Kővári et al. (2012) and also on many other active stars (Strassmeier, 2009). Polar spots produce spectral line-profile changes only in the line core itself (no Doppler shift), and the spectral signature of a symmetric polar spot is the same at each rotational phase of the star. This makes them very easy to be produced as artifacts in the Doppler imaging process; for example, if the depth of the spectral line-profile is not correctly modeled, then the image will exhibit a polar spot. In addition, strong chromospheric activity has

been postulated to fill in at least some of the photospheric lines used in Doppler imaging, and also produce a polar spot Unruh & Collier Cameron (1997); Bruls et al. (1998). These facts made the reliability of polar spots highly debated in the early days of Doppler imaging (Strassmeier et al., 1991; Piskunov & Wehlau, 1994) and the independent confirmation of their existence here is highly significant.

While our results only strictly apply for giant stars in RS CVn binaries, we note strong parallels between the physical conditions and manifest magnetic behavior of these and pre-main sequence stars. The giant primary stars in RS CVn binaries rotate rapidly due to tidal spin-up, while pre-main sequence stars rotate rapidly due to contraction and angular momentum transfer due to accretion of material from a circumstellar disk. These similar physical conditions hint at shared field-generation mechanisms that are observationally indistinguishable (Bouvier & Bertout, 1989) and manifest as starspots. In young associations, it has been noted that derived ages are likely strongly affected by global suppression of convection (Somers & Pinnsoneault, 2015). These commonalities and the known consequences argue that strong stellar magnetism must be accounted for in stellar models for both pre-main sequence and giant stages of evolution for the most active stars.

6.6 Conclusions

In conclusion, results from imaging studies using light-curve inversion and Doppler imaging techniques, as well as new interferometric spot studies (Parks et al., submitted), all re-enforce the picture that global magnetic structures cover the faces of the most active stars. Our interferometric imaging has found unambiguous signposts of these structures and clearly points to a perspective beyond the conventional isolated "starspot" paradigm inspired by heliophysics. The large-scale suppression of convection by these large-scale fields will have structural effects on the stellar atmosphere, including puffing up the star and decreasing the effective temperature and luminosity,

dramatic alterations that must be accounted for by modern stellar structure calculations especially for young, low-mass stars that universally show strong magnetic activity (Somers & Pinnsoneault, 2015; Oláh et al., 2014).

CHAPTER VII

Concluding Remarks

7.1 Discussion of Results

Throughout this work, I have concentrated efforts on imaging stellar magnetism through the proxy of starspots. To do so, I have taken advantage of state-of-the-art observational and imaging resources in order to create detailed images of stellar surfaces. By observing how starspots appear and evolve, the work presented here has further pushed a shift from starspots being sunspot analogs to being a region of increased magnetism among a global network of suppressed convection.

7.1.1 Inverting *Kepler* Light Curves

By using the precision light curves of the *Kepler* satellite, I applied a light-curve inversion algorithm to two targets showing evidence of starspots. These long-term, detailed studies of spot evolution revealed one system to be rapidly-changing with spots quickly forming and disintegrating on the stellar surface (KIC 5110407), while the other system (KOI-1003) had long-lived spots that persisted for the length of the observations. These two targets begin to show the diversity of stellar magnetism, and potentially its dependence on a variety of factors including rotation period.

With the first of these systems (KIC 5110407) I compared the timing of white-light flares to the stellar surface at the time of the flare. I found that the largest of

flares occurred when the largest spot features were facing *Kepler*, but for weak flares there was no correlation. This is potentially due to flares not requiring the presence of localized starspots to occur, but rather are a phenomenon of a global magnetic network like that observed on ζ And. KOI-1003 exhibited less-frequent flares than KIC 5110407, so a similar analysis was not preformed.

With its constantly forming and dissolving starspots, KIC 5110407 was an optimal star on which to test differential rotation. LI is capable of only weakly resolving relative latitudes between starspots with a single filter. With *Kepler* data we were able to only weakly constrain the amount of differential rotation observed to being less than that of the Sun, which was to be expected for a star rotating every 3.4683 days.

The persistent formation of starspots at particular longitudes of KOI-1003 confirms the existence of active longitudes, and reveals a system in stark contrast to KIC 5110407. While both stars have approximately the same temperatures based upon the *Kepler* Input Catalog and have rotation periods much less than the Sun, KOI-1003's rotation period is more than twice that of KIC 5110407 and KOI-1003 has a companion.

An investigation of more spotted systems in the *Kepler* archives could reveal the stellar and system properties that dictate the structure and evolution of starspots. Further studies of these spotted stars would reveal insight into a correlation between flare strength and starspot location, differential rotation, and ultimately stellar evolution as affected by stellar magnetism.

7.1.2 Detecting Faint Stellar Companions

In two of the RS CVn systems observed during this work, I was able to detect the faint companions. Making those detections on several nights each and combining them with radial velocity curves allowed for precise determinations of orbital and stellar parameters. Using those parameters to model the systems' light curves provided

an opportunity to analyze long-term, ground-based multiband photometry. In both light curves, ellipsoidal variations were detected and allowed for gravity darkening to be measured. In the first parameter-free measurements of convective envelope stars, gravity darkening was found to be consistent with canonical theory.

Additionally, with σ Gem, I was able to refute the claim of active longitudes on the star (Henry et al., 1995). Instead, the ellipsoidal variations were being observed when the star was not otherwise spotted. In the instances when large starspots dominated the surface, masking the ellipsoidal variations, the radial velocity observations were found to be shifted such that the system would appear slightly eccentric.

Previous observations of o Dra claimed the star to be spotted, but we found that what had been thought to be starspots was actually the combination of the ellipsoidal variation and a previously unknown secondary eclipse. Because the secondary star is significantly hotter than the primary star, the primary eclipse is barely detectable but the secondary eclipse is prominent.

These observations and analyses have led to an improved understand of the systems while emphasizing the power of interferometric observations and the utility of long-term data sets including the radial velocity and photometric data sets used in this work.

7.1.3 Directly Imaging Stellar Surfaces

The methods used for detecting the companions of σ Gem and o Dra were not capable of revealing the companion of ζ And reliably. This was due to the presence of large spot structures that obscured the binary signal in the interferometric data, which makes ζ And an ideal candidate for surface imaging.

Using a novel imaging technique that combines observational epochs to image on a sphere, improving resolution, the surface of ζ And from two sets of observations was imaged. In both epochs, large polar spots were observed, confirming the existence

of the structures previously only detected with Doppler imaging. Notably, global networks of magnetically-suppressed convection also appear on the surfaces, as opposed to the standard starspot paradigm of isolated regions of suppressed convection analogous to sunspots.

The observation of these global spot structures lends support to previous theories and observations suggesting that strong magnetic fields are causing inaccurate estimates of star sizes and ages.

7.2 Future Work

While this work has focused on observing particular objects in great detail, extending this work to both more observational techniques and more targets will provide ample opportunities for future projects. Below, I discuss a project presently being investigated and a potential project that would benefit the fields of stellar activity and evolution, exoplanet detection and characterization, and star and planet formation.

7.2.1 Comparative Imaging

Simultaneously with the CHARA/MIRC interferometric observations of σ Gem and ζ And, I organized with the help of collaborators simultaneous spectroscopic and photometric observations of these stars. Spectroscopic observations were collected by collaborator Heidi Korhonen with a number of telescopes including the Very Large Telescope's Ultraviolet and Visual Échelle Spectrograph (UVES), the Nordic Optical Telescope (NOT), and STELLA échelle spectrograph and are intended for Doppler imaging of the starspots of σ Gem and ζ And. Photometric observations were obtained by Gregory Henry with the Tennessee State University Automated Photometric Telescopes (APT) and through National Optical Astronomy Observatory (NOAO) at the Small and Medium Aperture Research Telescope System (SMARTS) 1.3m telescope at Cerro Tololo Inter-American Observatory (CTIO).

With these simultaneous data sets we will compare different techniques to directly highlight their unique advantages and contrasts. Additionally, we will further investigate the observability of the global networks of suppressed convection present on ζ And.

Difficulties for this task include the presence of ellipsoidal variations requiring both LI and Doppler imaging algorithms to account for the distortion from spherical and poor phase coverage. Another challenge has been obtaining good phase coverage in all data sets. For example, two data sets for σ Gem were obtained in 2011 November-December and 2012 November-December. While interferometric phase coverage is better in the 2012 data set, it is much better for Doppler imaging in the 2011 data set diminishing our ability to compare the data sets.

We additionally have two sets of spectroscopic observations for ζ and from 2011 July and 2013 September, contemporaneous with the interferometric observations discussed in Chapter VI, both of which have reasonably good phase coverage in all observing methods.

7.2.2 Future Interferometric Targets

While there is no fundamental limit to the resolving power of an interferometer, a practical limit is in place due to the inability to presently create facilities with longer baselines. The longest baseline interferometric facility is the CHARA array with its longest baseline of 331m (ten Brummelaar et al., 2005). The combiner best able to image stellar surfaces is MIRC (Monnier et al., 2004) used in this work. MIRC uses all six CHARA telescopes to obtain the best possible uv coverage. As MIRC primarily operates in H-band, the combination of it with CHARA allows for detailed imaging of stars of angular diameter $\theta \gtrsim 2$ mas. Under this value, details cannot be distinguished, but surface asymmetries may be detected.

The set of active stars presently available for imaging with CHARA/MIRC is very

Table 7.1. Potential Interferometric Imaging Targets

Target Name	Classification	Target Size, θ_{UD} (mas)[a]	V	H
λ And	RS CVn	2.759[b]	3.82[c]	1.40[c]
ϵ Hya	RS CVn	2.708[d]	3.38[c]	1.40[e]
ζ And	RS CVn	2.502[f]	4.06[c]	1.615[e]
σ Gem	RS CVn	2.335[g]	4.29[c]	1.799[e]
o Dra	RS CVn	2.115[h]	4.642	1.87[e]
ϵ Eri	BY Dra	2.112	3.73[c]	1.75[c]
33 Psc	RS CVn	2.033	4.61[c]	2.31[c]
ϵ UMi	RS CVn	1.85	4.222	2.422[e]
ι Cap	BY Dra	1.75	4.27[c]	2.32[c]
61 Cyg A	BY Dra	1.775[i]	5.21[j]	2.50[c]
10 LMi	RS CVn	1.573	4.60	2.31[c]
TX Pic	RS CVn	1.48	6.106	2.906[e]
δ CrB	RS CVn	1.392	4.63[c]	2.798[e]
ϵ UMa	α^2 CVn	1.356	1.77[c]	1.73[c]
KX Lib	BY Dra	1.252	5.72[c]	3.23[c]
IM Peg	RS CVn	1.128	5.892	3.398[e]

Note. — [a]Target sizes are theoretical estimates given by Bonneau et al. (2006) unless otherwise noted.
[b]Parks et al. (submitted)
[c]Ducati (2002)
[d]ϵ Hya is a known multi-star system with a close binary system in the center (Mason et al., 2015). This binarity is likely causing the size of this star to be overestimated.
[e]Cutri et al. (2003)
[f]See Chapter VI.
[g]See Chapter IV.
[h]See Chapter V.
[i]Kervella et al. (2008)
[j]Nicolet (1978)

limited. Because the stars are required to be nearby, bright, and spatially large, we are restricted to only a few targets (see Table 7.1 for potential targets). Focusing on RS CVns, as I have in Chapters IV − VI, one other target is sufficiently large and known to be spotted to resolve surface features: λ And, which has been imaged by Parks et al. (2011, submitted). Because the sample RS CVns available for imaging starspots consists only of ζ And, σ Gem, and λ And, these stars could be monitored for starspot evolution over years of study.

Since only a few more RS CVns would be good for determining only surface asymmetries (e.g., SU LMi, IM Peg), we must consider other active stars with large spots, such as young K and M main sequence stars (sometimes classified as BY Draconis). Boyajian et al. (2012a) measured the radii of 21 of the nearest K and

M stars, finding many of them to have submilliarcsecond angular diameters, which is too small for understanding surface features with current capabilities. The cool, main-sequence stars with the largest angular diameter and potential starspots are the components of 61 Cygni (K5V and K7V Kervella et al., 2008). With component angular diameters of $\theta_{\rm LD,A} = 1.775 \pm 0.013$ mas and $\theta_{\rm UD,B} = 1.581 \pm 0.022$ mas both stars could have potential for at least observing surface asymmetries. In fact, there was a 2015 July observing run to observe 61 Cyg A and B with this goal, but the run was plagued by high humidity.

To improve upon the resolution of CHARA/MIRC one must improve upon the array's angular resolution, $\theta \sim \lambda/B$, where θ is the angular resolution, λ is the observed wavelength, and B is the baseline length from the edge of one telescope to the edge of another. To shrink θ, either the wavelength must decrease or the baseline must increase. To decrease wavelength, it is necessary to build beam combiners in the visible wavelengths, such as the Navy Precision Optical Interferometer's (NPOI) Visible Imaging System for Interferometric Observations at NPOI (VISION), as well as the Precision Astronomical Visible Observations (PAVO) and the Visible spEctro-Graph and polArimeter (VEGA) instruments at CHARA. Combining this with the long baselines of CHARA or longer for future arrays would push the resolution limit even further allowing access surface imaging for more than a small handful of nearby, cool stars (see Table 7.1).

7.2.3 Starspot Catalog for Stellar Activity and Planet Detection

As mentioned in Chapter I, magnetic activity is correlated with rotation and spectral type (Noyes et al., 1984). In order to investigate the saturation of magnetic activity at small R_o, a study of active M dwarfs would utilize the imaging methods discussed in the preceding chapters of this work.

To study the activity, a variety of imaging techniques would be used to determine

the role of starspot coverage in the saturation of magnetic activity in M dwarfs. This study would include examining the spotted M stars in the public *Kepler/K2* archive and the upcoming data from the Transiting Exoplanet Survey Satellite (TESS, August 2017 planned launch) with LI (Harmon & Crews, 2000). Because so many stars have been or will be observed with these satellites, a variety of starspot characteristics can be found ranging in size, shape, and number.

To supplement these images, a representative sample of bright, rapidly rotating M dwarfs would be imaged with Doppler imaging using resources that would allow both optical and infrared imaging, the combination of which will allow for detecting starspot-affected atomic (e.g., Fe) and molecular lines (e.g., CO) in both the optical and infrared. Observing molecular lines will allow for the measurement of vertical structure of starspots due to the depths molecular lines probe. This vertical structure can improve estimates of the convective turnover time, $\tau_{\rm conv}$, which is important to understanding the saturation of the stellar-activity-rotation relationship. Additionally, direct images could be obtained for the small number of M dwarfs that are both bright and spatially large enough to resolve surface features using long-baseline optical interferometry (e.g., with CHARA/MIRC).

The compilation of these images will lead to a catalog of starspots to be used to investigate the transition between unsaturated and saturated activity in M dwarfs, shedding light onto the reason for the transition (i.e., is there a limiting amount of the surface that can be covered with starspots, when does that occur, and what does it look like). The understanding of main-sequence stellar magnetism through this study would have an impact on star and planet formation because pre-main sequence stars are prone to even more rapid rotation, are fully convective, and have small Rossby numbers, suggesting that they are in the saturated regime. Quantifying the level of activity (starspots, flares, winds, etc.) is important to discerning the stellar magnetic field's effect on the star's circumstellar disk during formation of both the star and

any planets. After formation, the amount of activity on the star can dictate whether or not a planet in the habitable zone (potential for liquid water) is actually habitable (an atmosphere is present).

A survey of the activity of low-mass, main-sequence stars has implications beyond helping resolve the reason for saturation of the stellar-activity-rotation relationship. M dwarfs are of particular interest to TESS because the satellite's observing strategy focuses on transiting Earths and super-Earths with orbital periods $P_{\rm orb} \lesssim 20$ days (Sullivan et al., 2015). For M dwarfs, these periods are well-aligned with planets in the habitable zones (analogous to $P_{\rm orb} \lesssim 10$ days; Kasting et al., 1993), where understanding activity is vital.

To further exploit the usefulness of this catalog, the information gathered could quantify the effects of the imaged starspots on radial velocity curves through modifying model spectra by injecting the effects of cataloged spots rotating across the star. The starspot catalog and model radial velocities would be used to understand the noise that will be present in these data, potentially enabling its removal. A detailed study extending to those results contained in this dissertation will be invaluable to other fields of study including stellar evolution and planet characterization.

7.3 Final Remarks

In Gerald Kron's "Star Spots?" (1950), he told a story of looking at the Sun through haze in Pasadena, CA. When he suggested that starspots could not be observed directly with that telescopes of the time or in the future, he did not consider the possibility of optical interferometry becoming something more than what the Michelson interferometer (installed on the Mount Wilson Observatory 100-inch telescope) was capable of, which was measuring the angular diameters of the closest, largest stars. In the decades since, optical interferometers have been built with longer and longer baselines. In fact, the present best facility for interferometry is just up

the mountain from where he found himself considering the notion of starspots—the CHARA Array at Mount Wilson.

While many stars can be resolved today, only a handful of those stars can have had their surfaces imaged. Even fewer of those have features analogous to sunspots, those features that Kron did not think could ever be resolved. While my work here is not the first to resolve surface features, it is the first to directly image the surface of a spotted star as it rotates, the first to verify the existence of polar spots beyond Doppler images, and the first to image globally-suppressed convection. Combining those successes with my other efforts to image spotted stars in the vast catalogs of space-based photometery and to perform detailed analyses of other active stars combining a variety of observational techniques, I have helped to push the collective understanding of stellar magnetism beyond what pioneers in stellar astrophysics thought could be possible when they were first considering starspots.

APPENDICES

APPENDIX A

Surface Reconstructions of KIC 5110407

We include our complete collection of Mercator surface maps that have been reconstructed with LI. For each angle of inclination, we present panels of the surface reconstructions. In Figures A.1 − A.8, we present these panels split between Quarters 2−5 and 7−9. The beginning Barycentric Julian date (BJD-2455000) of each light curve is given in the lower left corner of each surface map.

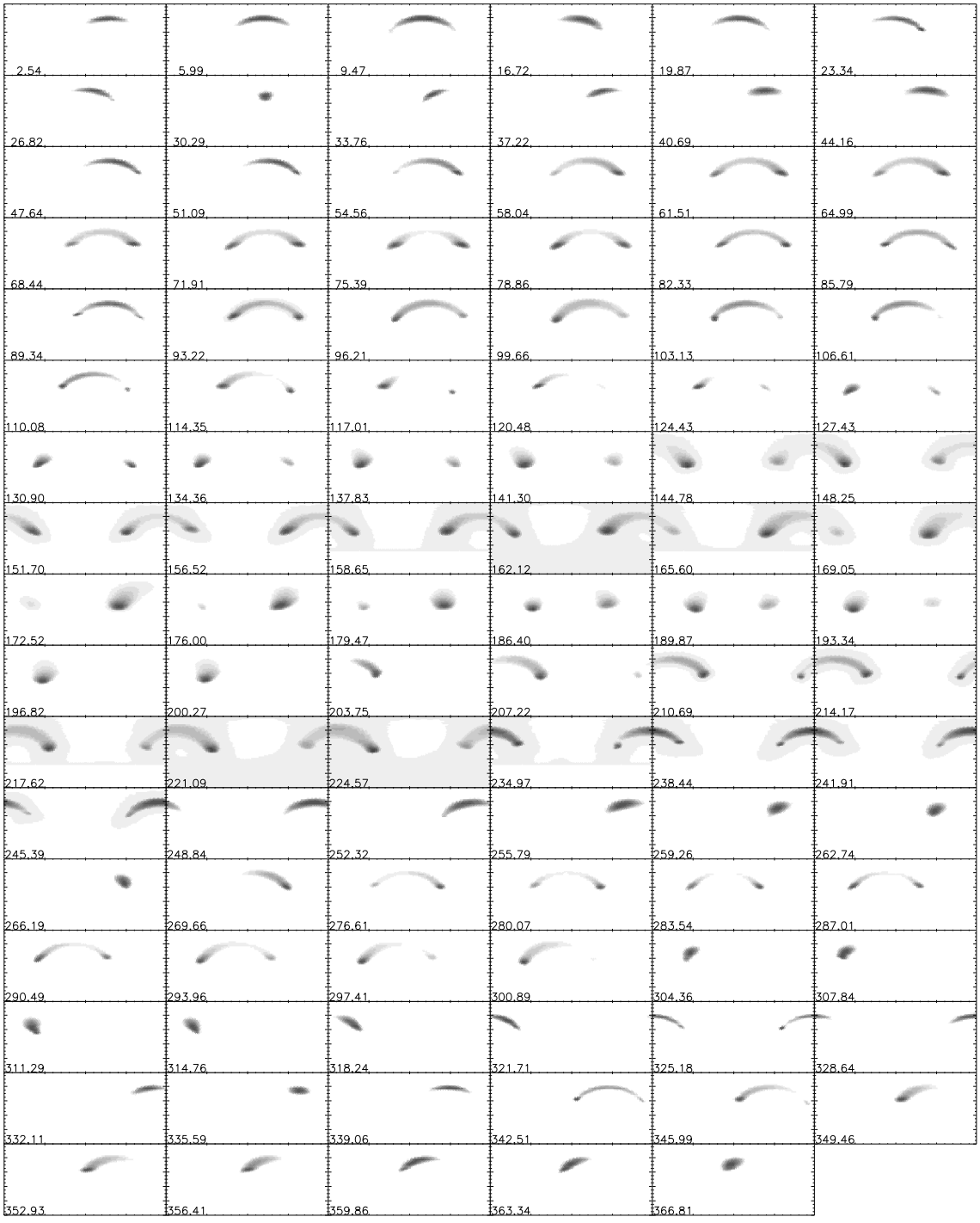

Figure A.1: Panel of the reconstructed surfaces for KIC 5110407 with $i = 30°$ using data from Quarters 2−5. The beginning Barycentric Julian Date (BJD-2455000) of each light curve is included in the lower left corner of each plot.

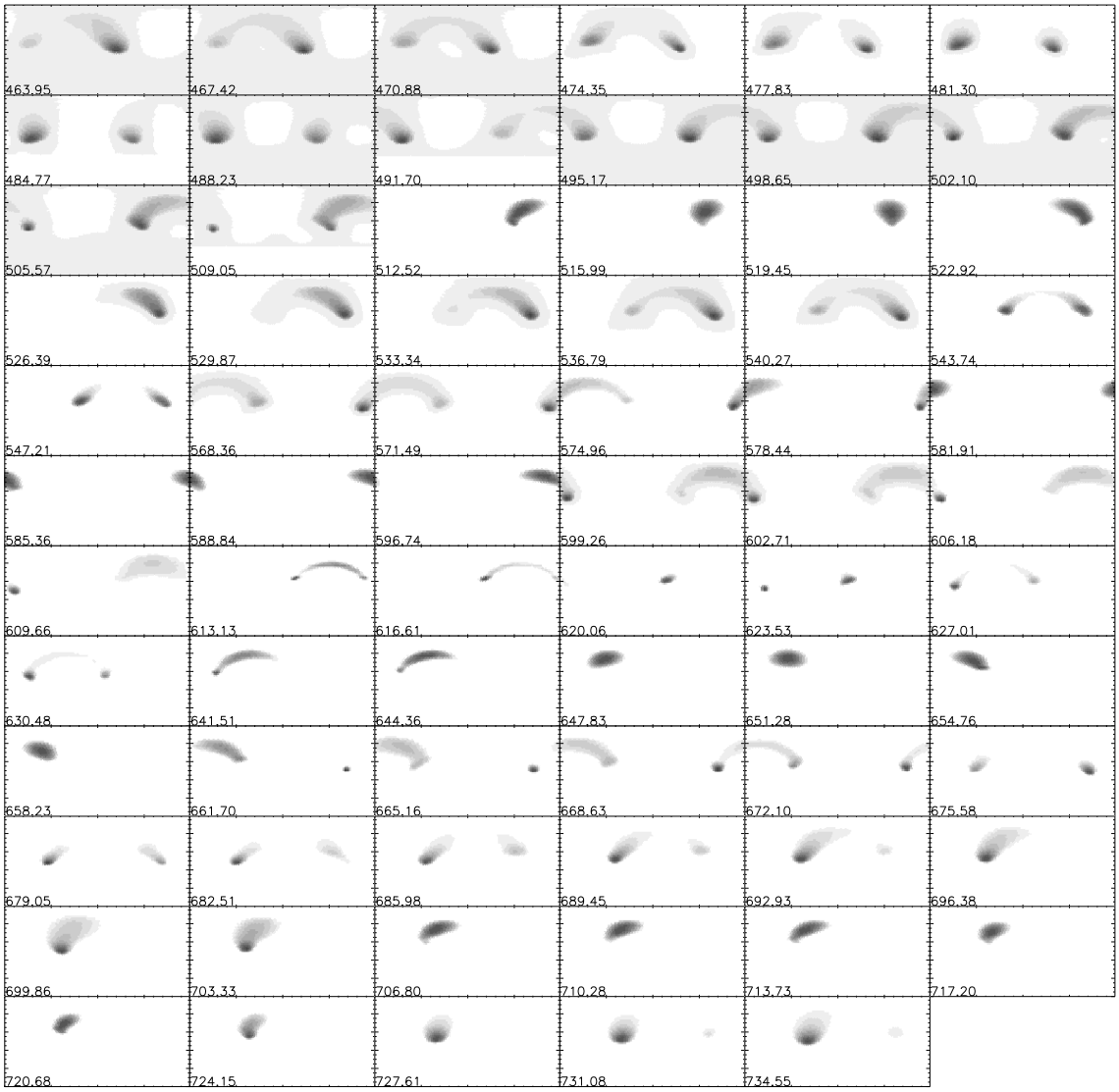

Figure A.2: Panel of the reconstructed surfaces for KIC 5110407 with $i = 30°$ using data from Quarters 7−9. The beginning Barycentric Julian Date (BJD-2455000) of each light curve is included in the lower left corner of each plot.

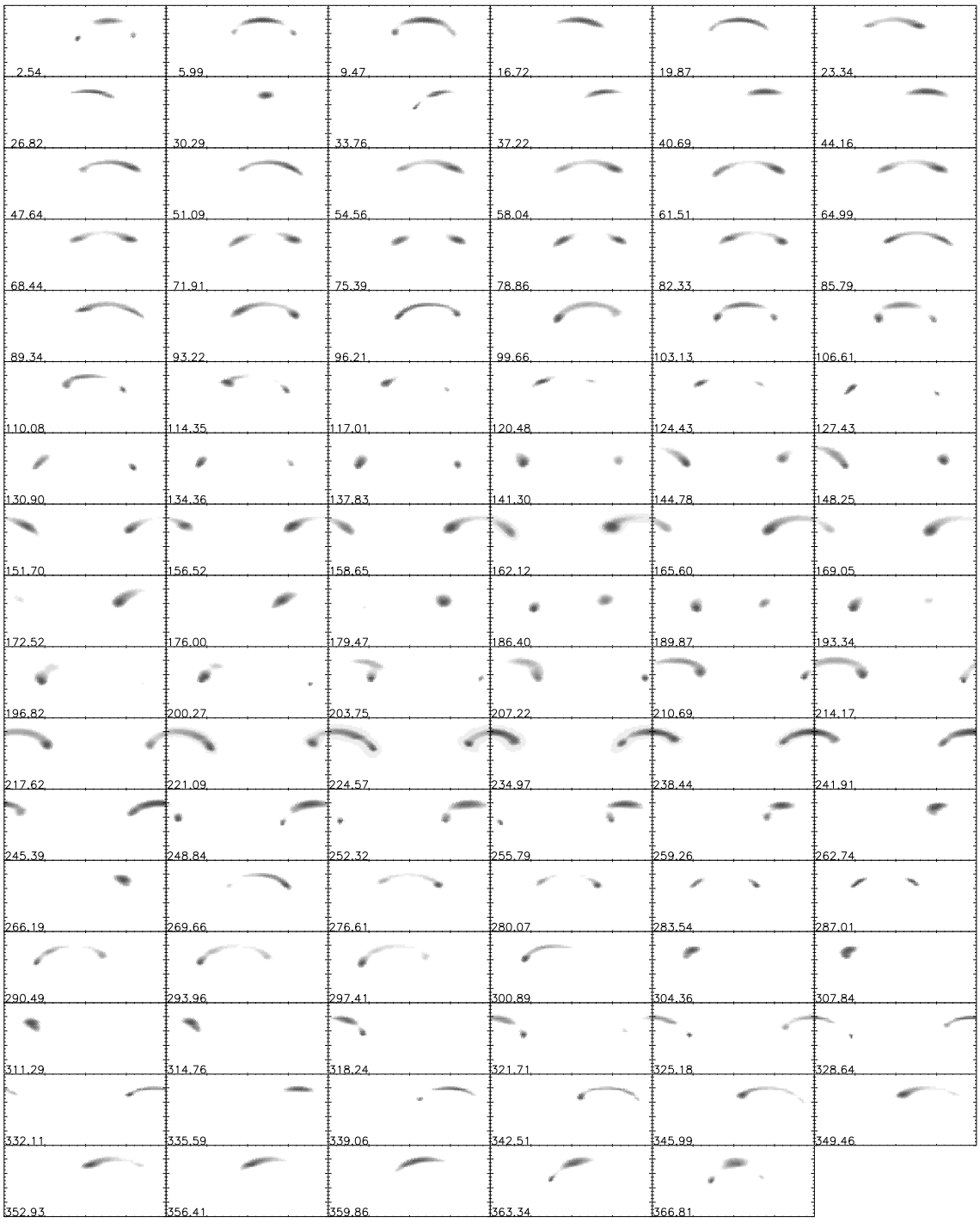

Figure A.3: Panel of the reconstructed surfaces for KIC 5110407 as in Figure A.1 with $i = 45°$.

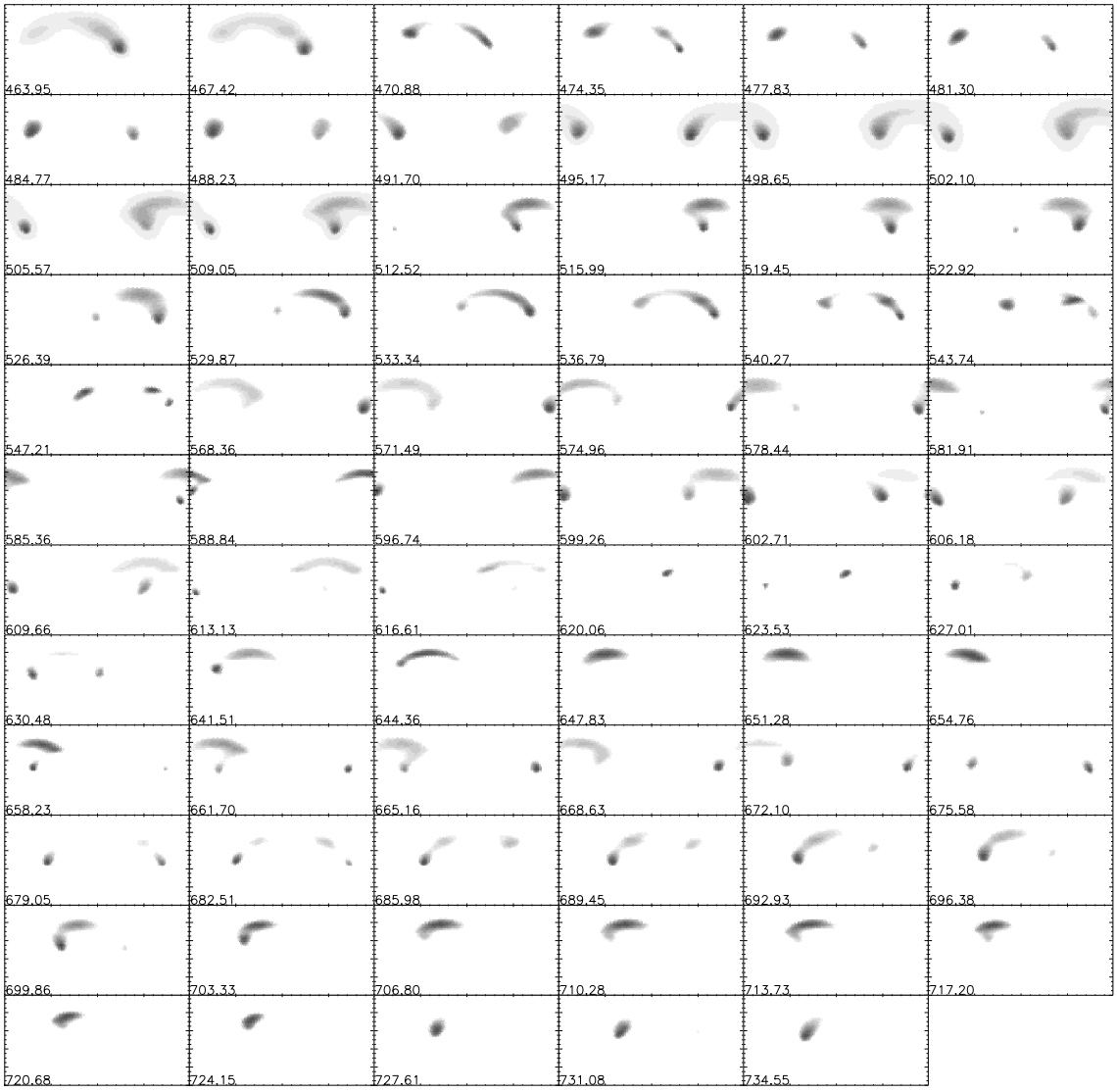

Figure A.4: Panel of the reconstructed surfaces for KIC 5110407 as in Figure A.2 with $i = 45°$.

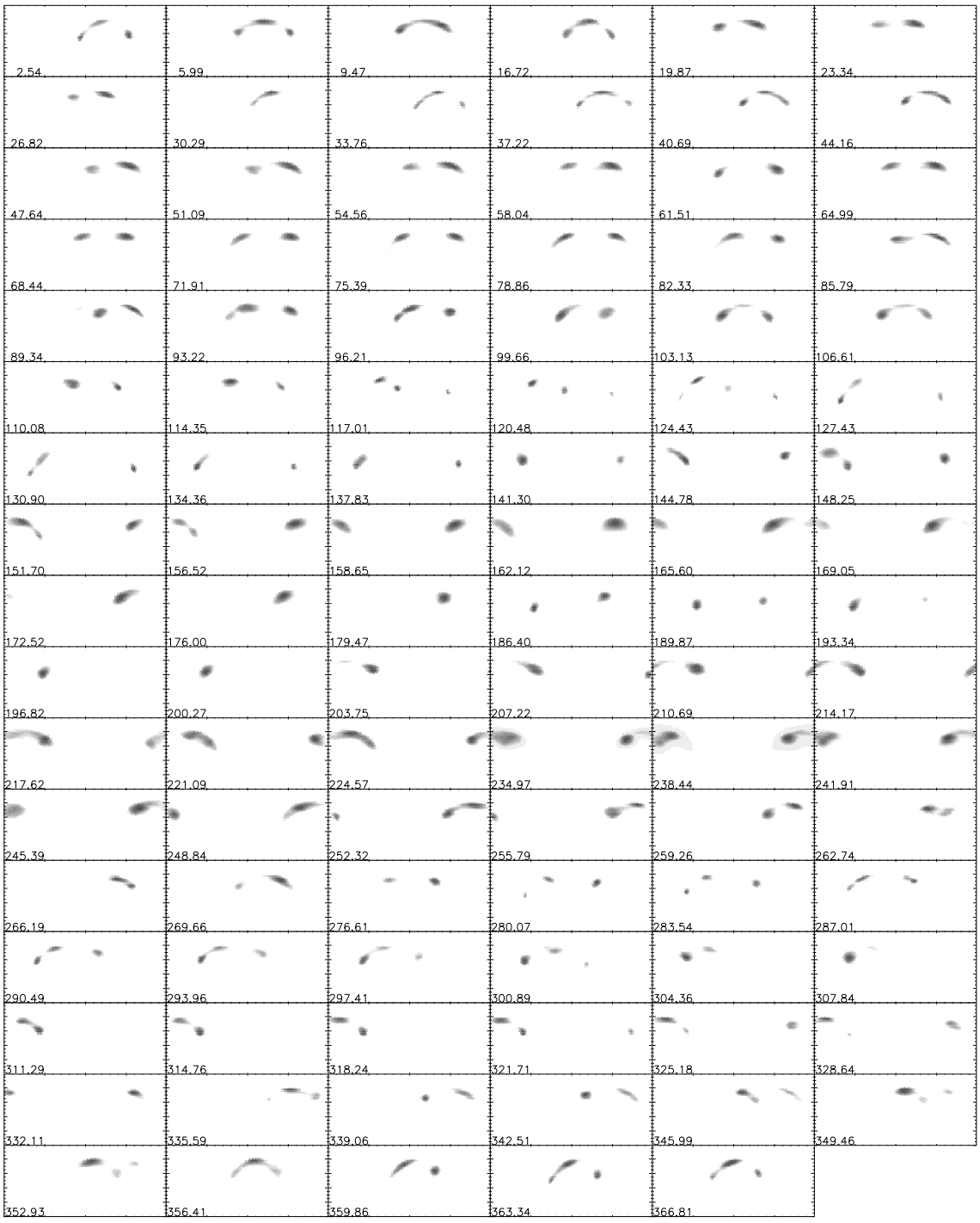

Figure A.5: Panel of the reconstructed surfaces for KIC 5110407 as in Figure A.1 with $i = 60°$.

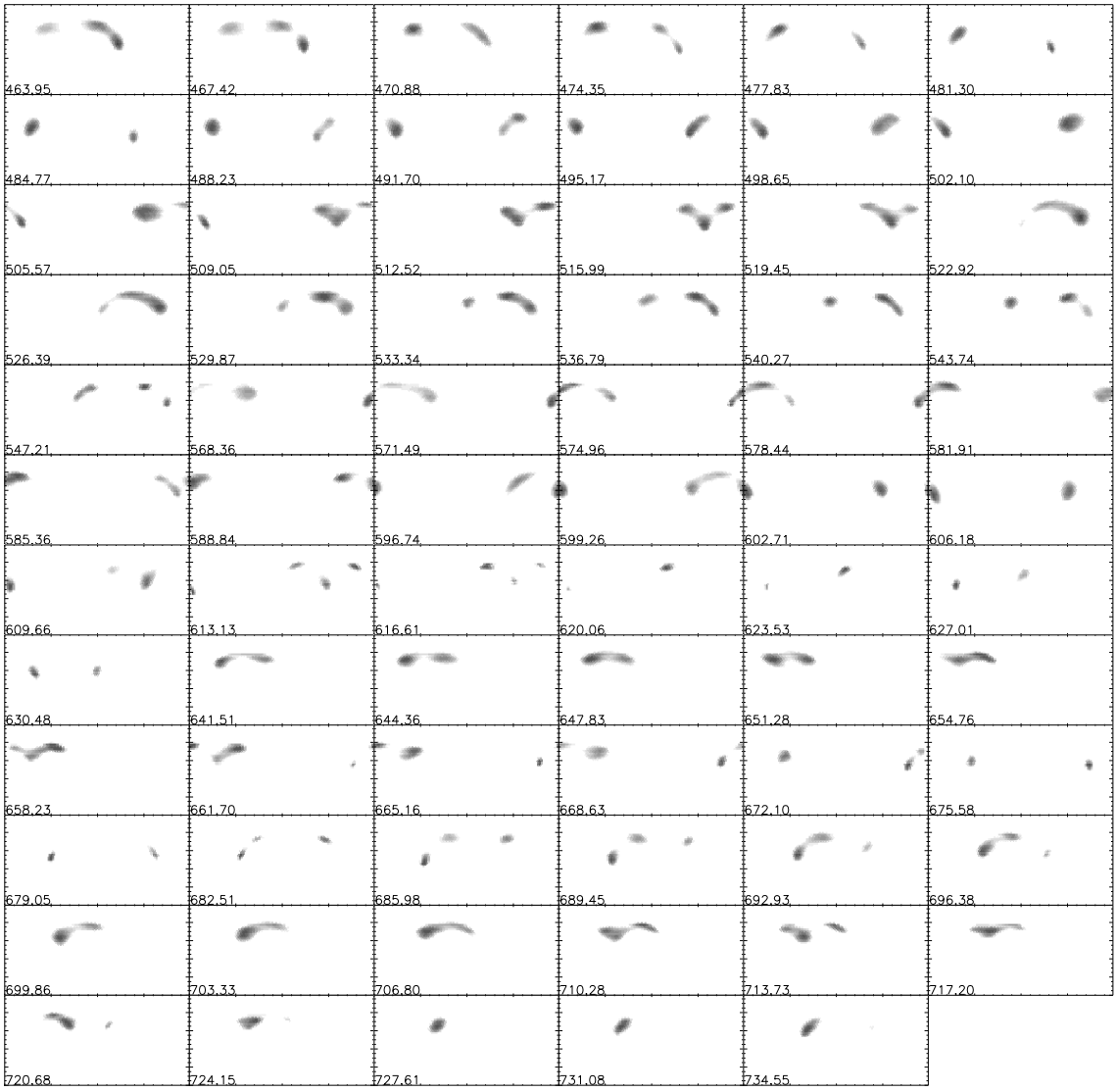

Figure A.6: Panel of the reconstructed surfaces for KIC 5110407 as in Figure A.2 with $i = 60°$.

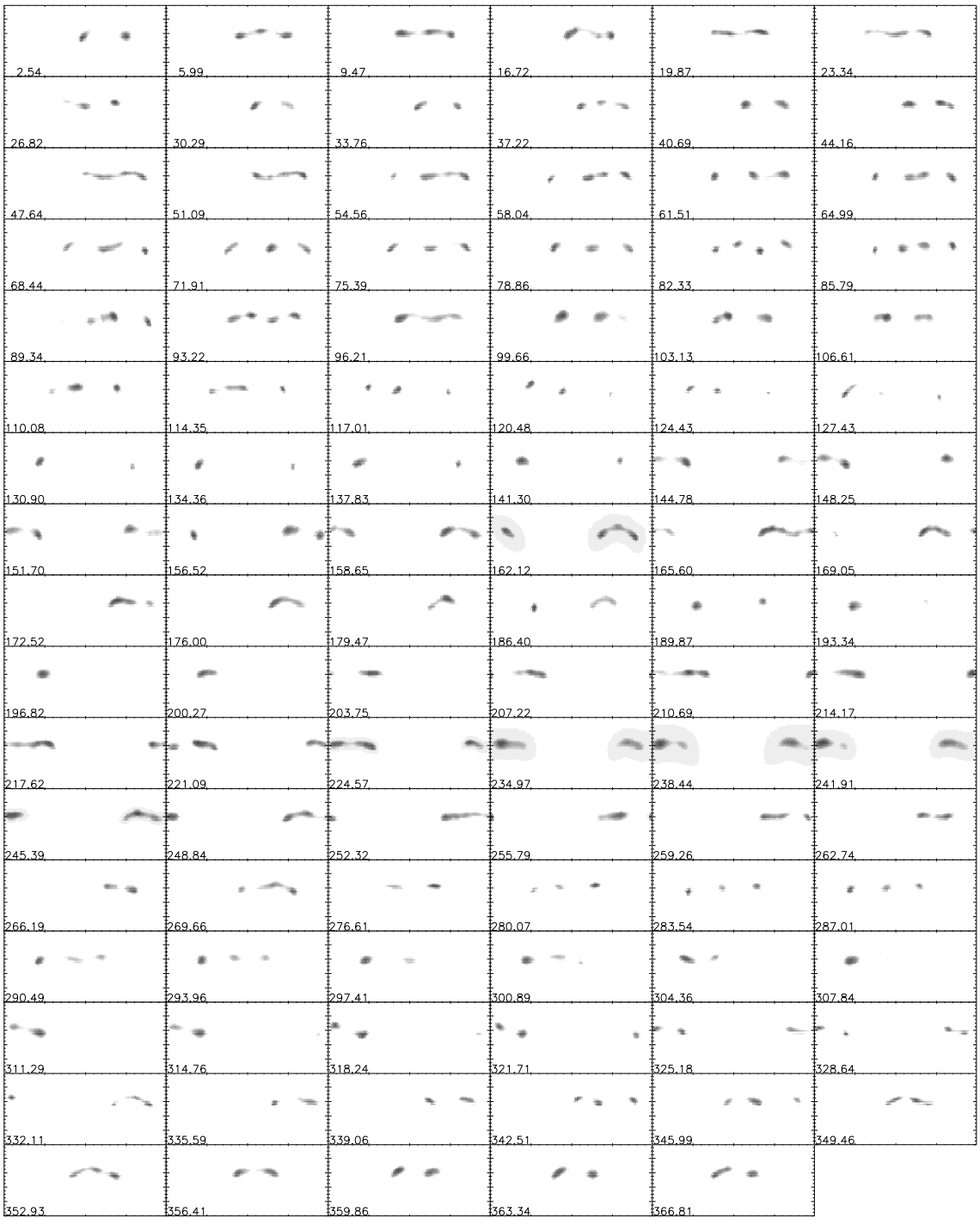

Figure A.7: Panel of the reconstructed surfaces for KIC 5110407 as in Figure A.1 with $i = 75°$.

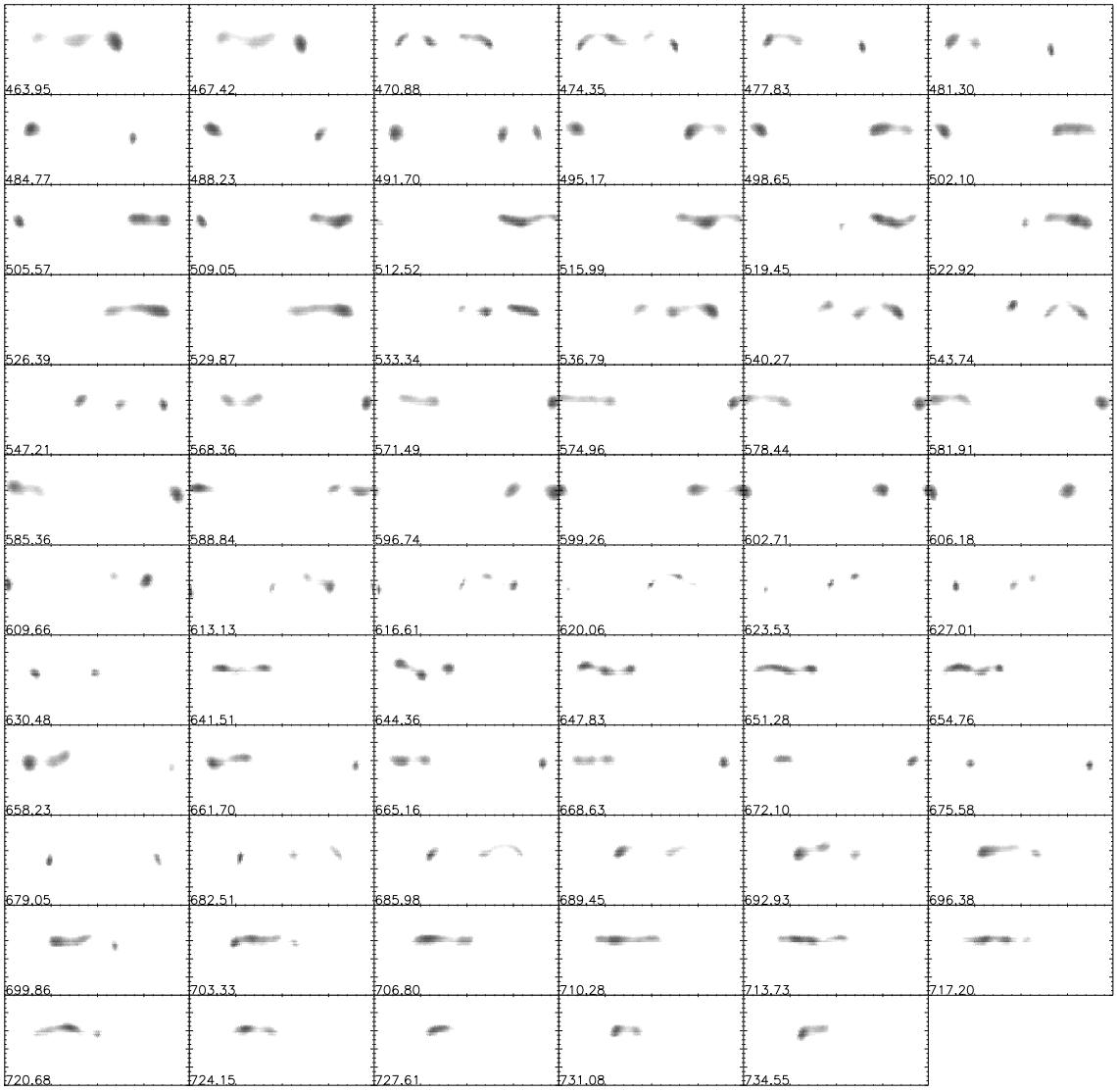

Figure A.8: Panel of the reconstructed surfaces for KIC 5110407 as in Figure A.2 with $i = 75°$.

APPENDIX B

Surface Reconstructions of KOI-1003

For five different inclination angles ($i = 30, 45, 60, 75$, and 90°), we include the pseudo-Mercator maps of the results surface reconstructions from LI in Figures B.1 − B.10. Each map has the Barycentric Julian Date - 2454833 in the lower left corner. The vertical line on each plot indicates the phase at which the secondary component begins to eclipse the primary star.

For each map, the long cadence *Kepler* data were used with the CBVs removed from the simple aperture photometry data. The eclipses were removed, and the data were binned in fifty phase bins (to reduce computation time). Single-rotation period light curves were inverted with LI if the phase coverage was greater than 65%.

As stated in Chapter III, LI assumes the following input parameters: $T_{\rm eff} \sim 5200$ K, $T_{\rm spot} \sim 3900$ K, and limb-darkening coefficients $e = 0.7369$ and $f = 0.1359$.

The maps presented were chosen from a series with varying rms values between the observed and reconstructed light curves. The criteria for selecting a map is based upon identifying the amount of noise required to balance between fitting to the noise and smoothing the surface features. For a detailed discussion of LI and its application to *Kepler* data, see Chapter II. Statistics on the rms values used for these reconstructions are found in Table B.1.

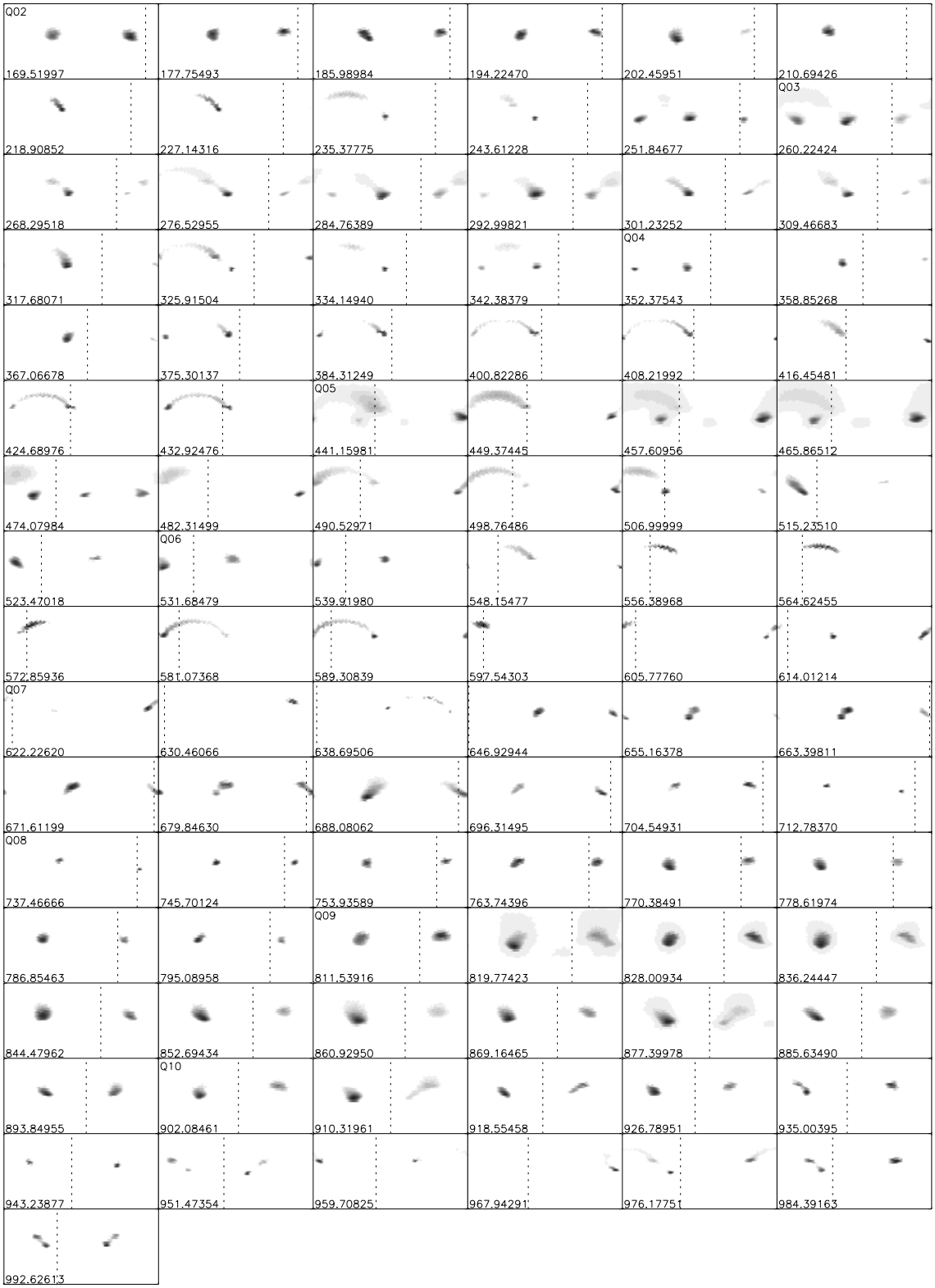

Figure B.1: Panel of LI-reconstructed pseudo-Mercator surfaces of KOI-1003 for $i = 30°$ (Q2−10). The beginning Barycentric Julian Date - 2454833 is included in the lower left corner of each plot. The beginning of eclipse on each map is represented by the vertical line.

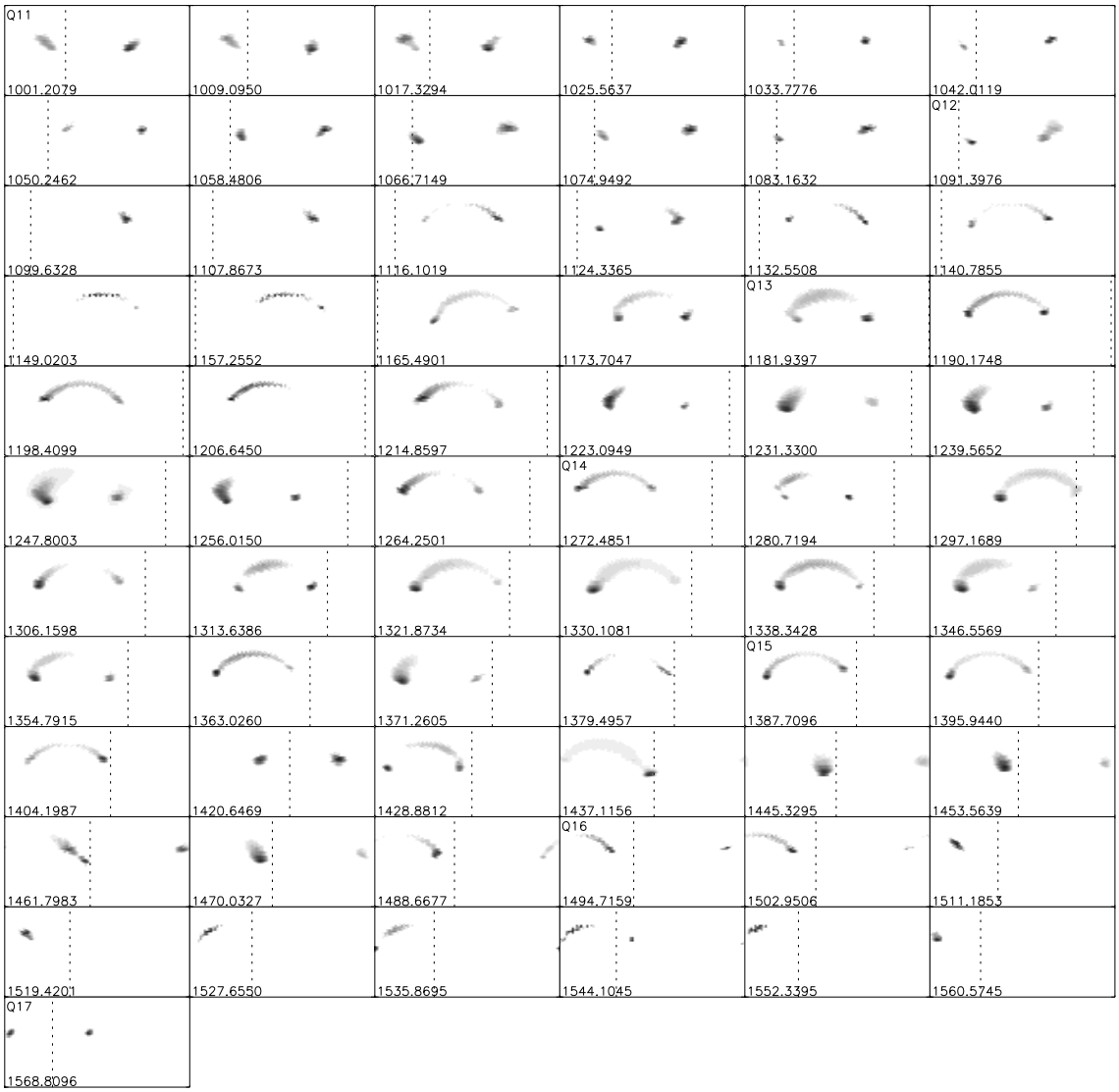

Figure B.2: Panel of LI-reconstructed pseudo-Mercator surfaces of KOI-1003 for $i = 30°$, as in Figure B.1, but for Q11−17.

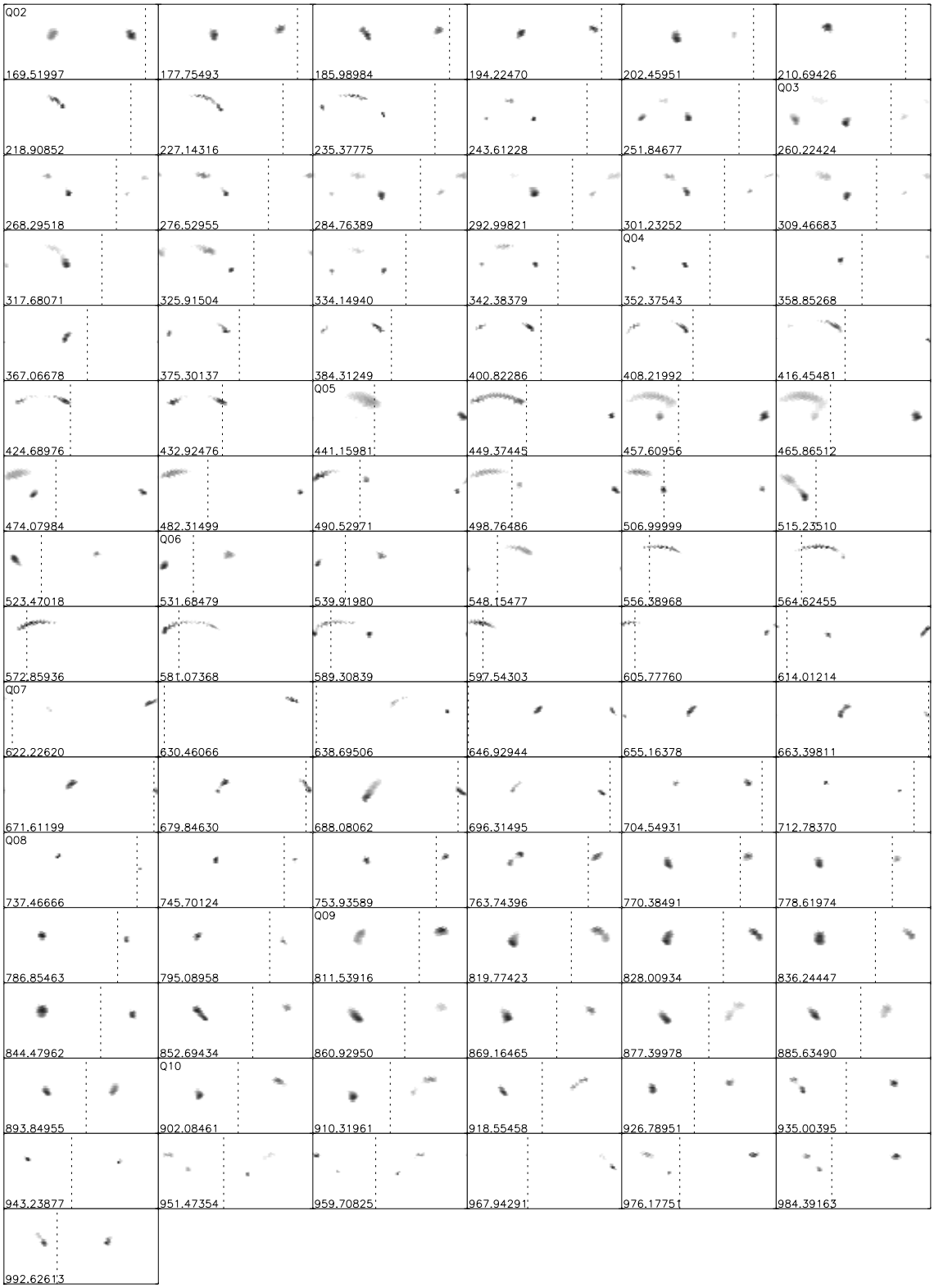

Figure B.3: Panel of LI-reconstructed pseudo-Mercator surfaces of KOI-1003 for $i = 45°$, as in Figure B.1.

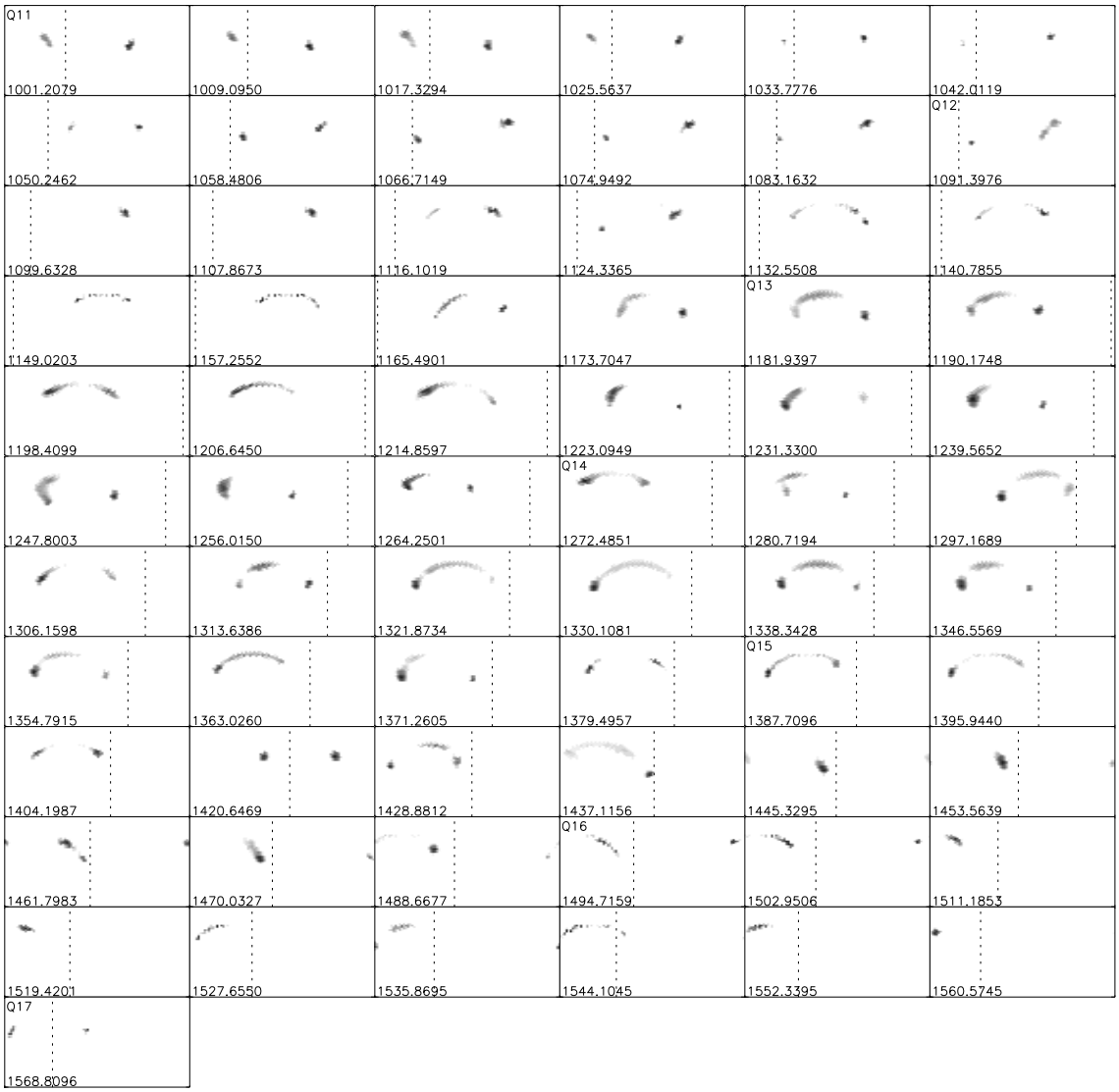

Figure B.4: Panel of LI-reconstructed pseudo-Mercator surfaces of KOI-1003 for $i = 45°$, as in Figure B.2.

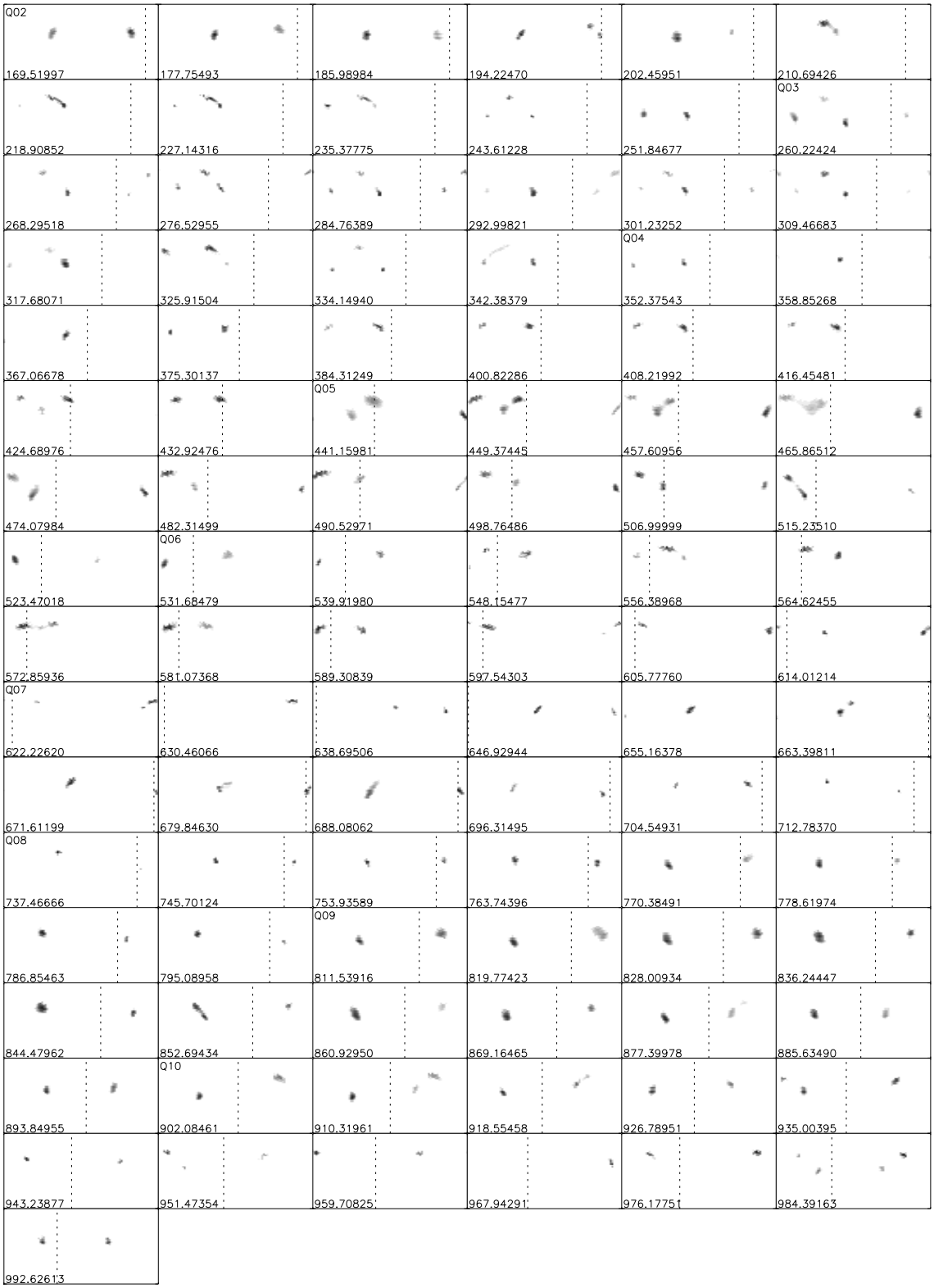

Figure B.5: Panel of LI-reconstructed pseudo-Mercator surfaces of KOI-1003 for $i = 60°$, as in Figure B.1.

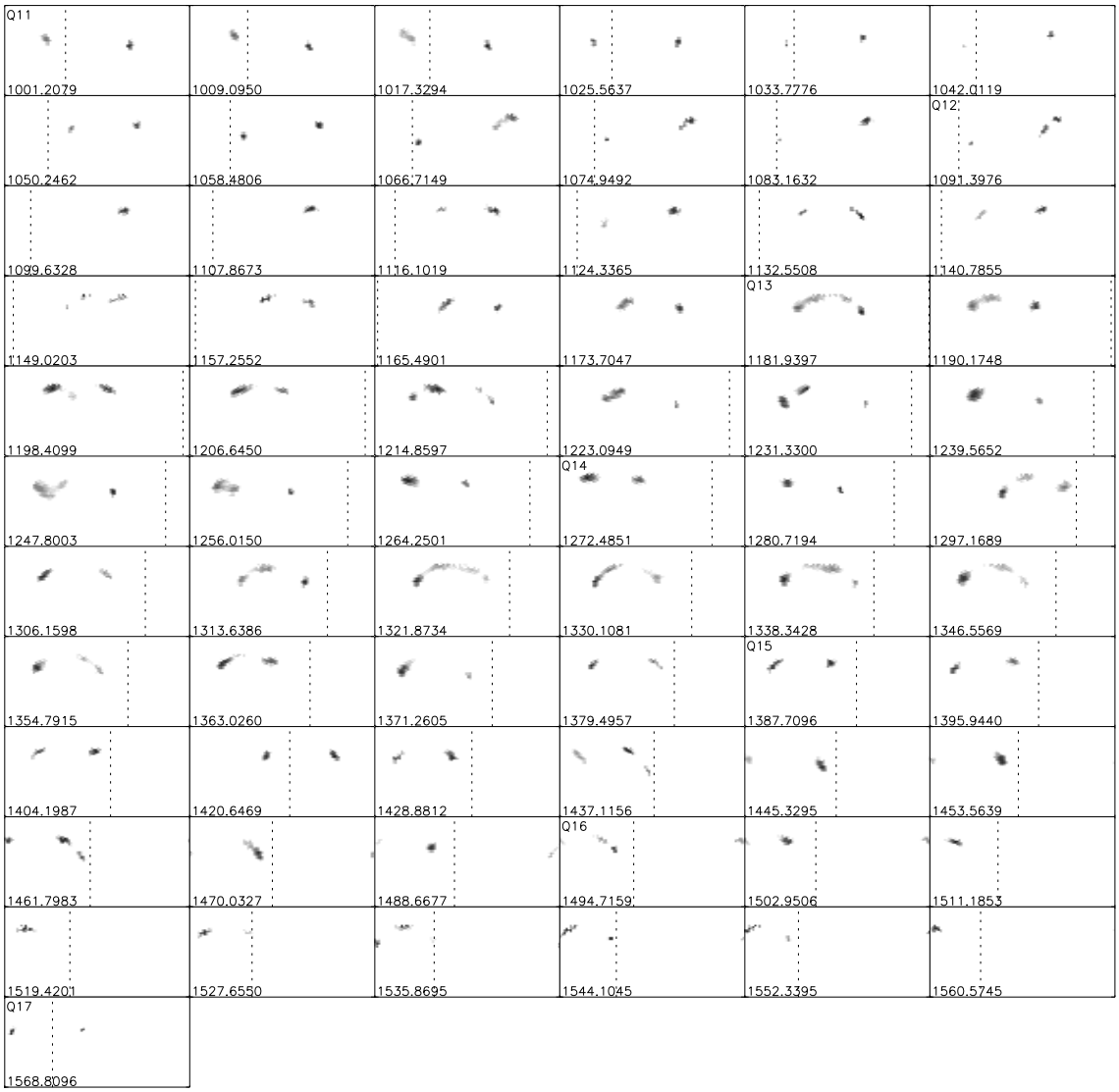

Figure B.6: Panel of LI-reconstructed pseudo-Mercator surfaces of KOI-1003 for $i = 60°$, as in Figure B.2.

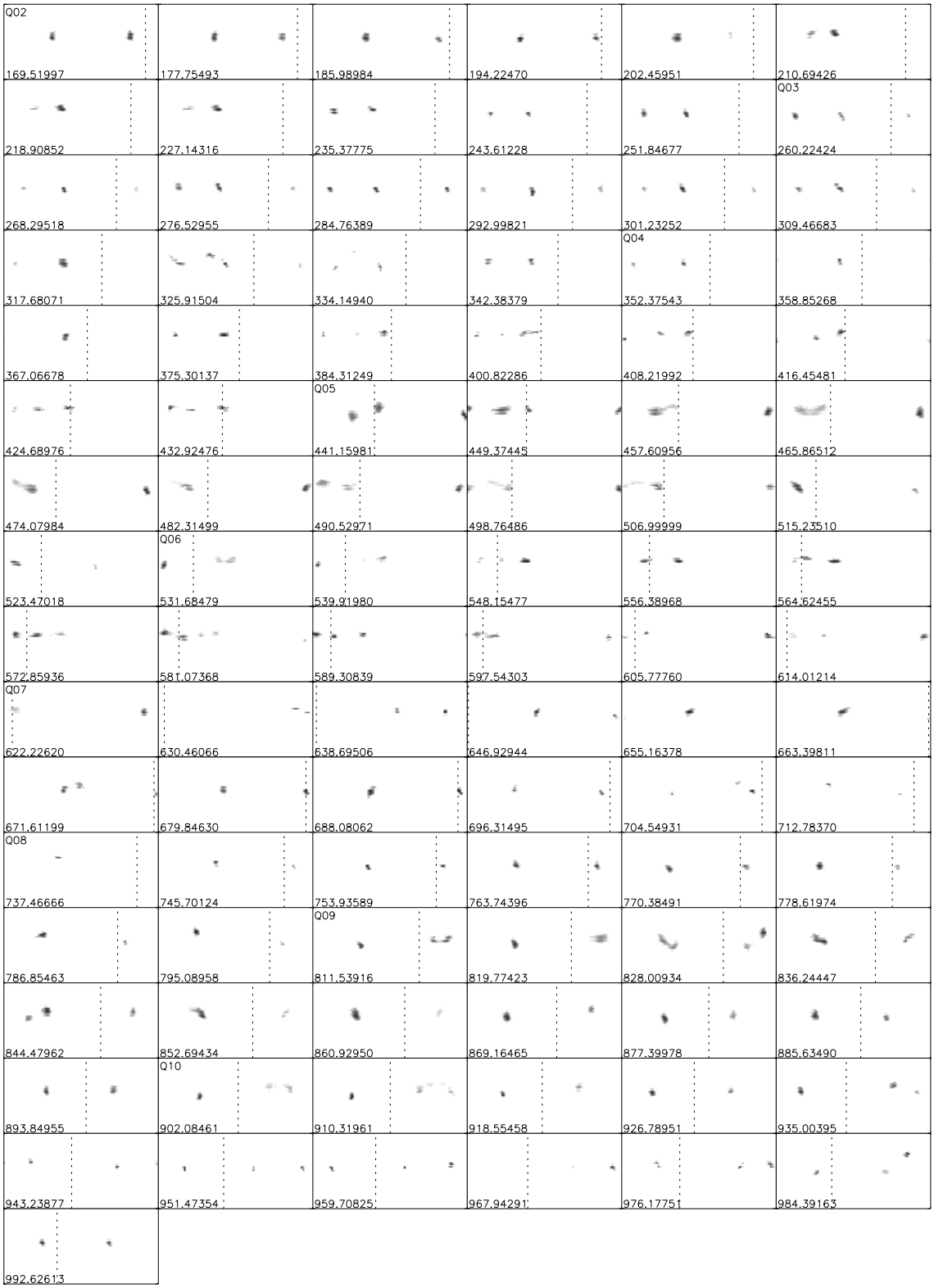

Figure B.7: Panel of LI-reconstructed pseudo-Mercator surfaces of KOI-1003 for $i = 75°$, as in Figure B.1.

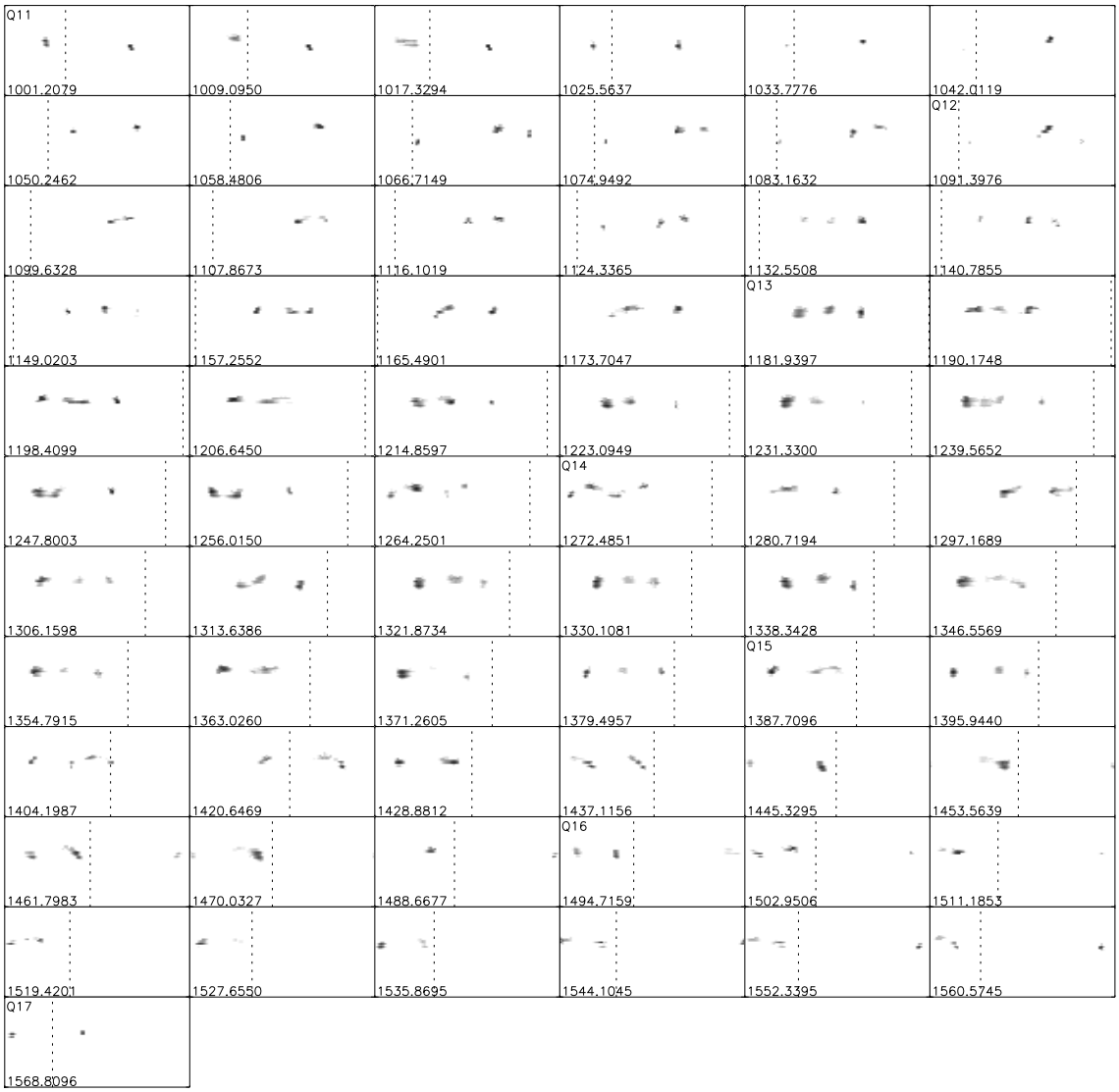

Figure B.8: Panel of LI-reconstructed pseudo-Mercator surfaces of KOI-1003 for $i = 75°$, as in Figure B.2.

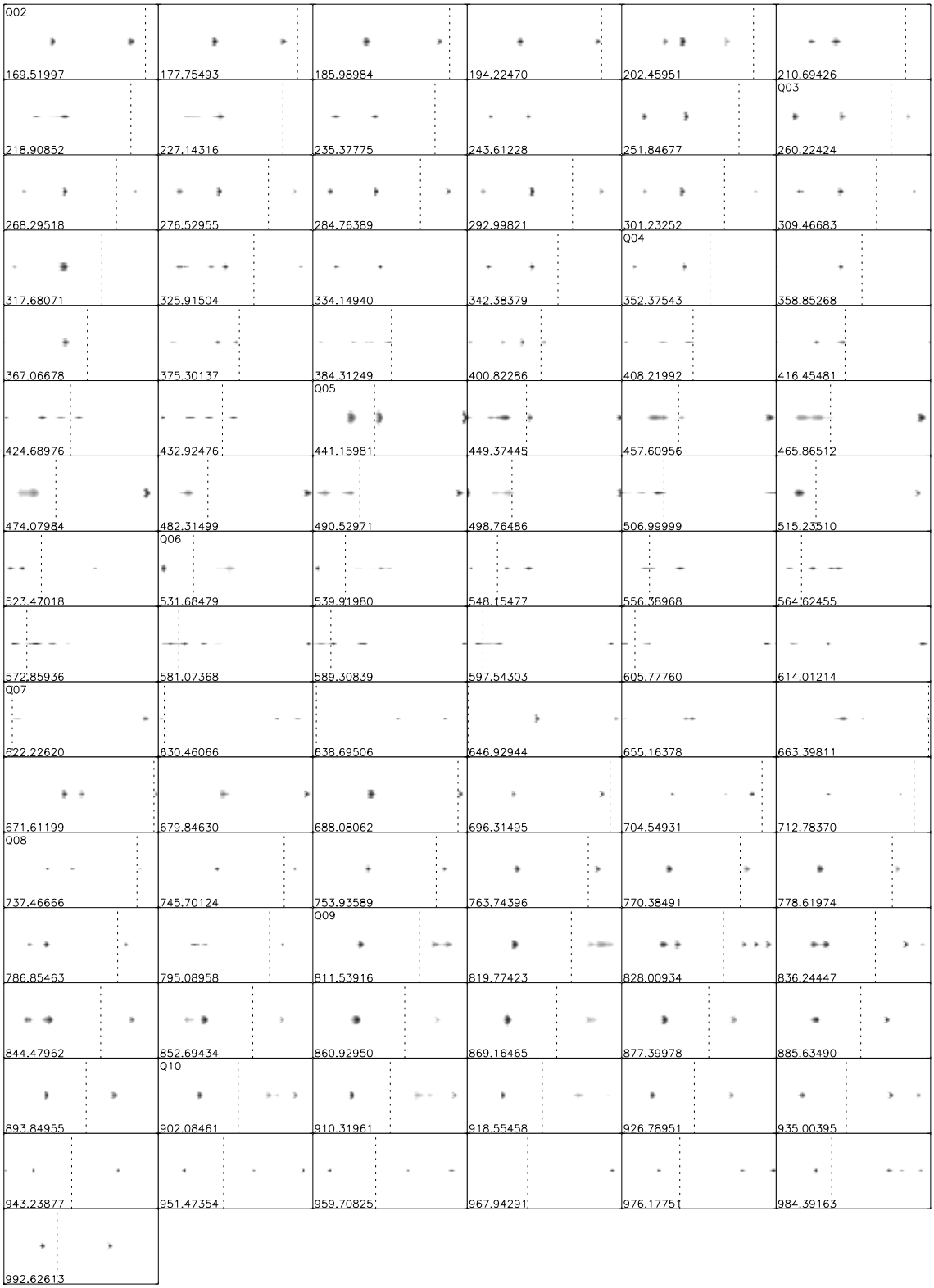

Figure B.9: Panel of LI-reconstructed pseudo-Mercator surfaces of KOI-1003 for $i = 90°$, as in Figure B.1.

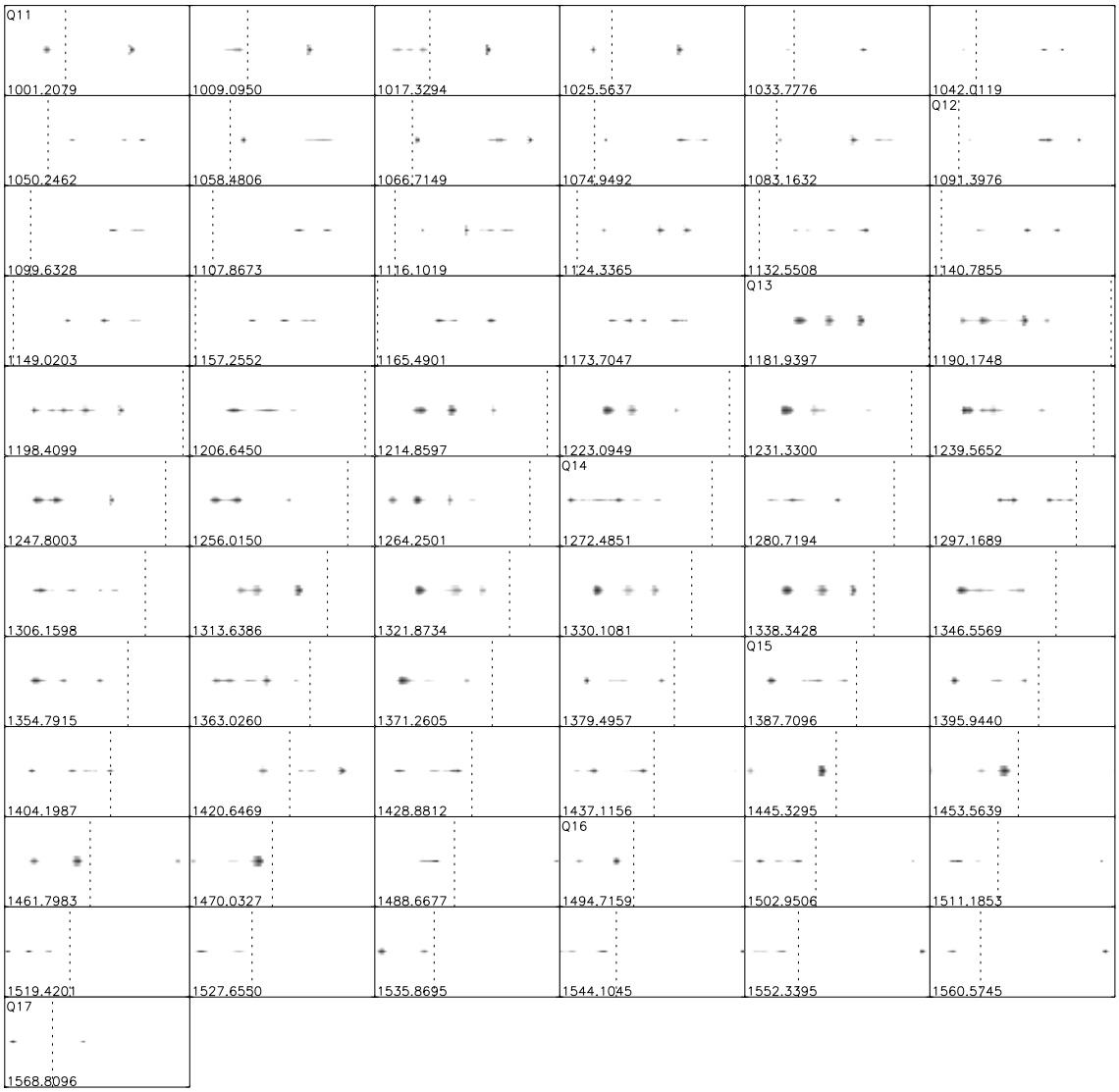

Figure B.10: Panel of LI-reconstructed pseudo-Mercator surfaces of KOI-1003 for $i = 90°$, as in Figure B.2.

Table B.1. Rms Deviations between Observed and Reconstructed Light Curves (magnitudes)

Angle of Inclination	Mean	Median	Minimum	Maximum	Standard Deviation
30	0.0010	0.0009	0.0004	0.0026	0.0004
45	0.0009	0.0008	0.0003	0.0025	0.0004
60	0.0009	0.0008	0.0004	0.0023	0.0004
75	0.0009	0.0008	0.0004	0.0022	0.0004
90	0.0009	0.0008	0.0004	0.0021	0.0004

APPENDIX C

Interferometric Observables of σ Gem

In Figures C.1 − C.4, we present a sample comparison of the calibrated σ Gem data from 2012 Nov 7 and the best-fit detection of the companion from our χ^2-space fit.

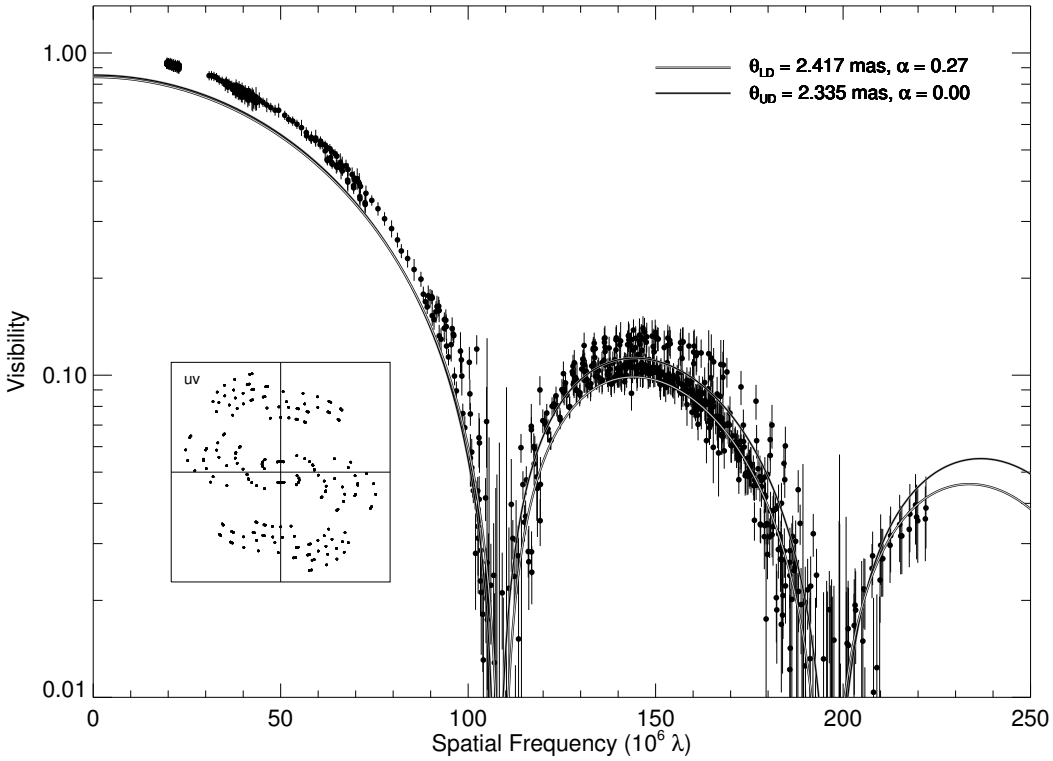

Figure C.1: Visibility curve of the 2012 Nov 7 observations of σ Gem with CHARA/MIRC. The observed visibility curve is plotted in black with 1σ error bars. The best-fit model from fitting for the companion is overplotted in as the black line ($\theta_{\rm UD} = 2.335$ mas, $V(0) = 854$, $\alpha = 0.00$). The white line is our limb-darkened model ($\theta_{\rm LD} = 2.417$ mas, $V(0) = 0.842$, $\alpha = 0.27$. The inset is the uv-coverage on the night of observation.

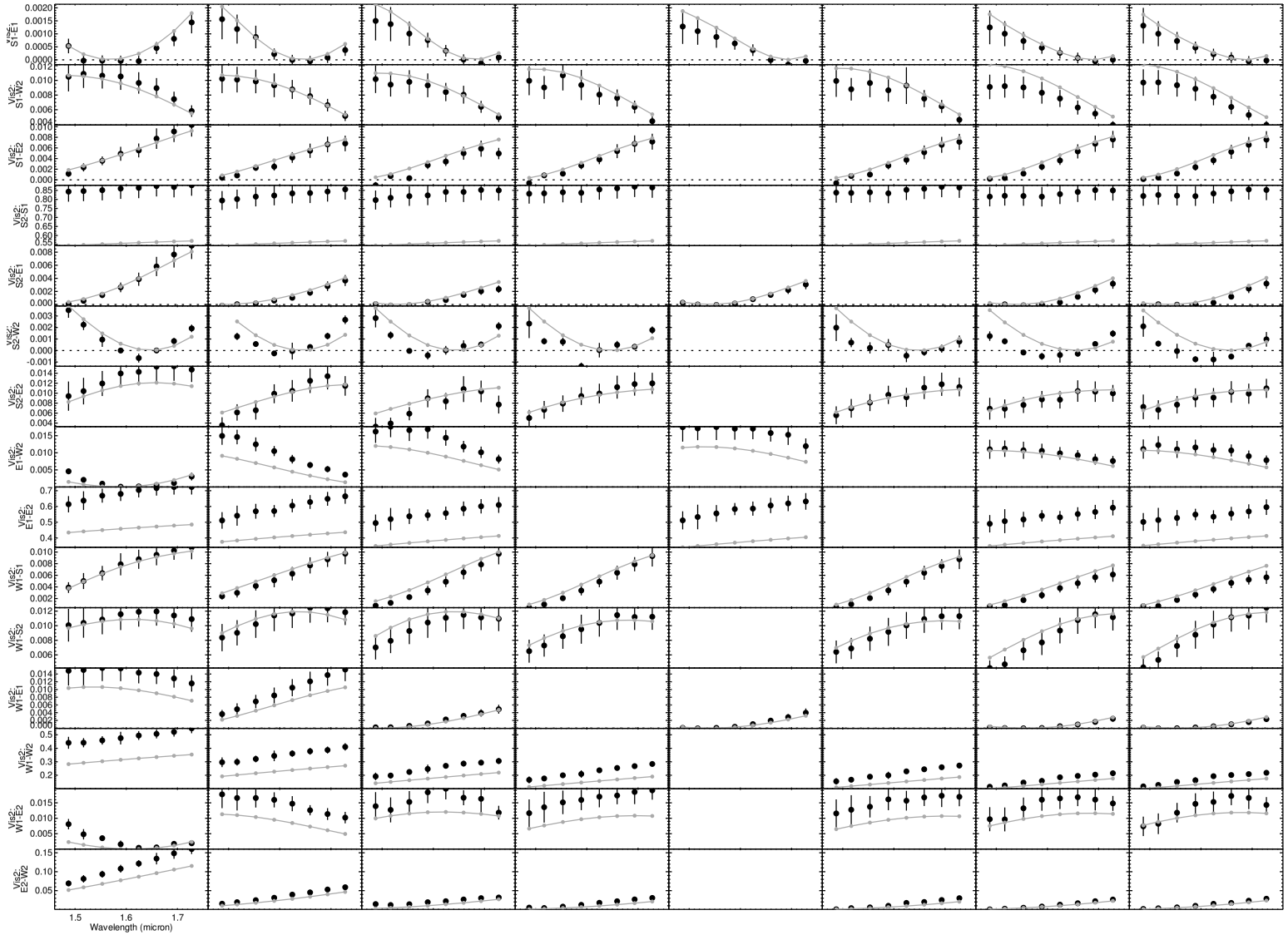

Figure C.2: Squared visibilities of the 2012 Nov 7 observations of σ Gem with CHARA/MIRC. Each block of observations represents a temporal block of observations. The data are plotted in black and model is overplotted in gray.

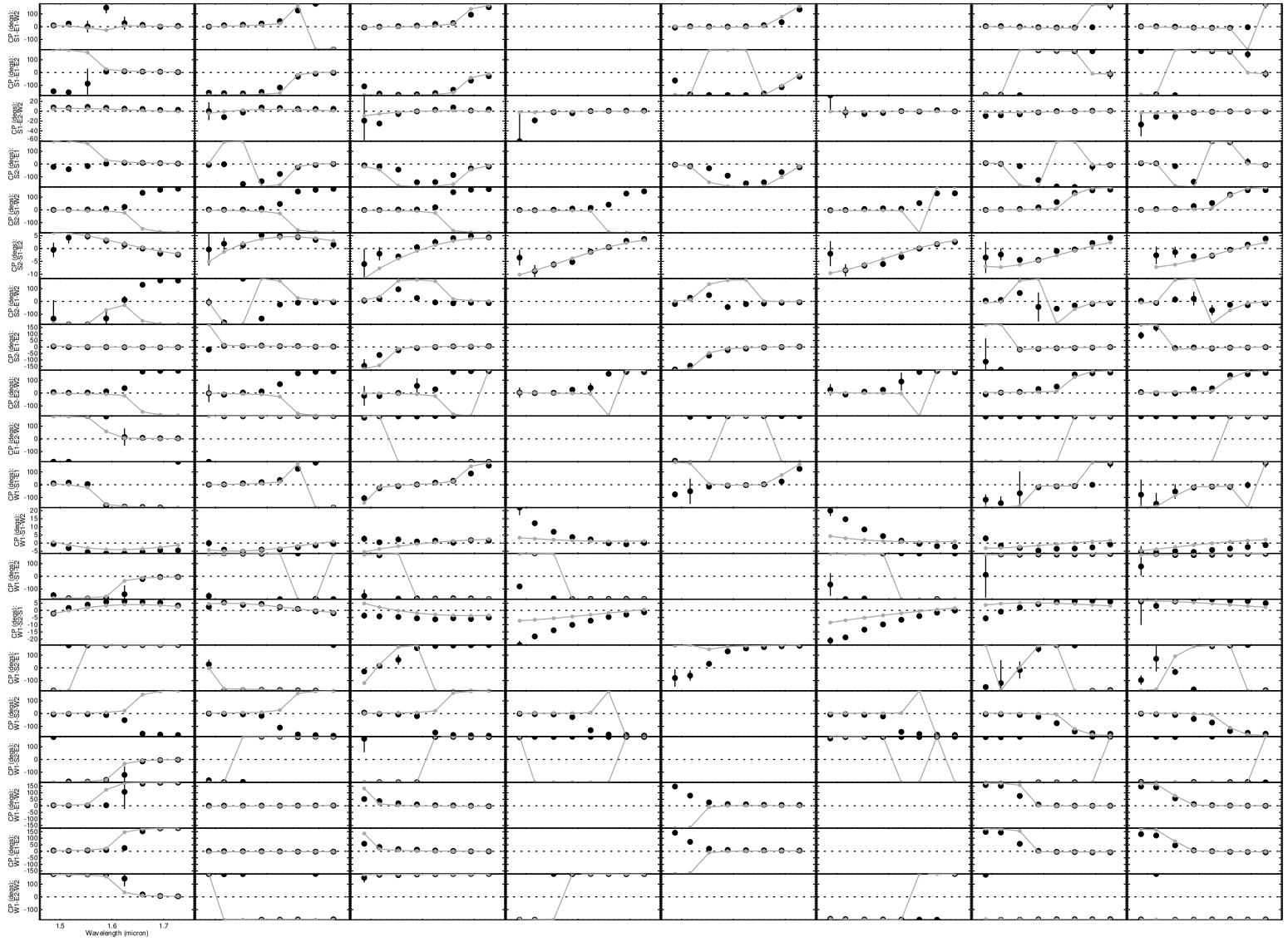

Figure C.3: Closure phases of the 2012 Nov 7 observations of σ Gem with CHARA/MIRC plotted as in Figure C.2.

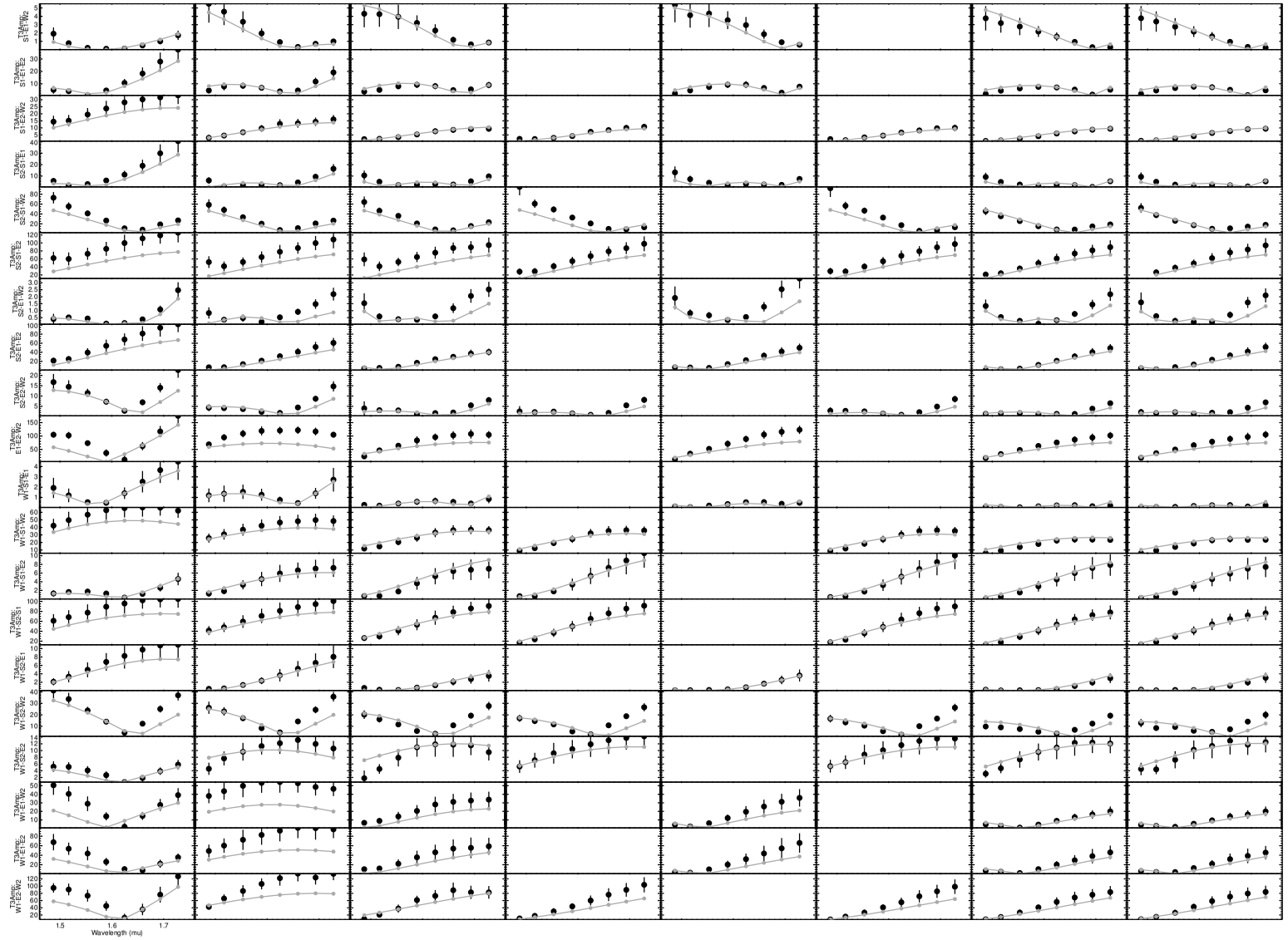

Figure C.4: Triple amplitudes (multiplied by 10^4 for clarity) of the 2012 Nov 7 observations of σ Gem with CHARA/MIRC plotted as in Figure C.2.

APPENDIX D

Difference Light Curves of σ Gem

In order to better justify our conclusion that ellipsoidal variations can explain previous claims of "active longitudes" on σ Gem, we have re-plotted some photometry from Kajatkari et al. (2014) in Figure D.1 along with our prediction of the expected ellipsoidal variation component using the ELC software and system parameters from Table 4.3 using gravity darkening parameter $\beta = 0.02$. In Figure D.1, we include data from two epochs, one showing very little overall variability and one showing high variability. In the first epoch ("Segment 8, Set 45" of Kajatkari et al. (2014)), the photometric data showed clearly a double-peaked light curve when phased with the orbital period, previously interpreted as due to active longitudes (see Kajatkari et al., 2014). Here, we now see by removing the expected ellipsoidal variation, the signature of two spots on opposite sides of the star (the basis for the active longitudes claims) nearly completely disappears (see Figure D.1). The second epoch ("Segment 9, Set 1" of Kajatkari et al. (2014)) is dominated by one spot and the ellipsoidal variations are not discernible. Nonetheless, future starspot modelers should account for the underlying ellipsoidal variations before performing detailed light curve analysis or surface brightness inversions.

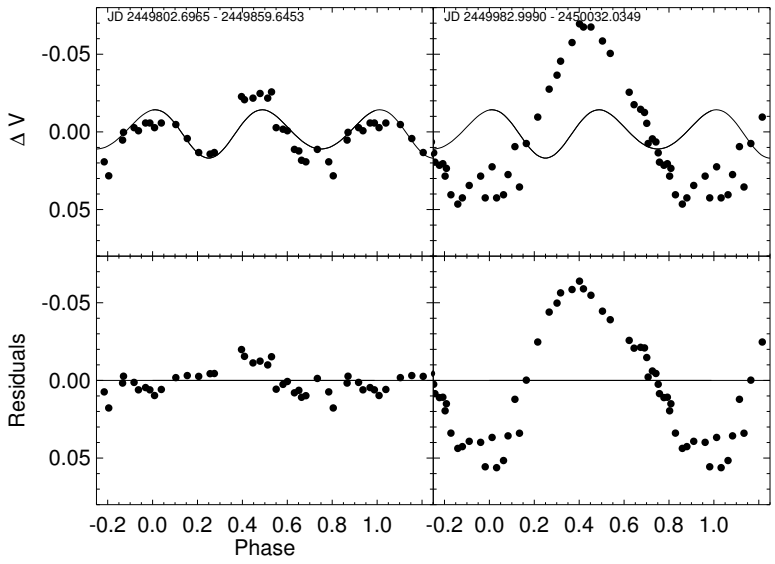

Figure D.1: Average-subtracted, differential Johnson V light curves of σ Gem plotted for JD 2449802.6965 − 2449859.6453 (left; Segment 8, Set 45 (Kajatkari et al., 2014)) and JD 2449982.9990 − 2450032.0349 (right; Segment 9, Set 1 (Kajatkari et al., 2014)). The top panel contains a plot of the APT data sets (circles) and the model ellipsoidal variations created with ELC for the orbital parameters of σ Gem and best-fit gravitational darkening coefficient $\beta = 0.02$ (solid line). The bottom panel contains the residuals of the APT light curve with the ellipsoidal variation signature removed (circles).

APPENDIX E

Interferometric Observables of o Dra

In Figures E.1 − E.4, we present a sample comparison of the calibrated o Dra data from 2012 Jun 18 and the best-fit detection of the companion from our χ^2-space fit.

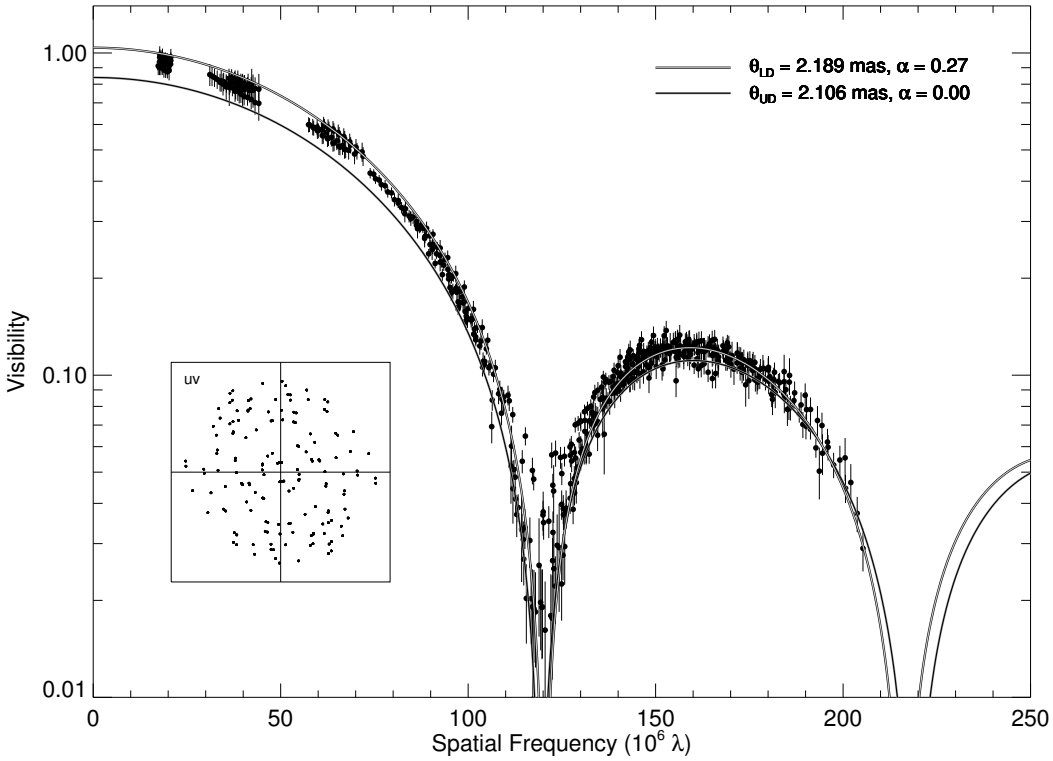

Figure E.1: Visibility curve of the 2012 Jun 18 observations of o Dra with CHARA/MIRC. The observed visibility curve is plotted in black with 1σ error bars. The best-fit model from fitting for the companion is overplotted in as the black line ($\theta_{\rm UD,A} = 2.106$ mas, $V(0) = 0.839$, $\alpha = 0.00$). The white line is our limb-darkened model ($\theta_{\rm LD,A} = 2.189$ mas, $V(0) = 1.038$, $\alpha = 0.27$. The inset is the uv-coverage on the night of observation.

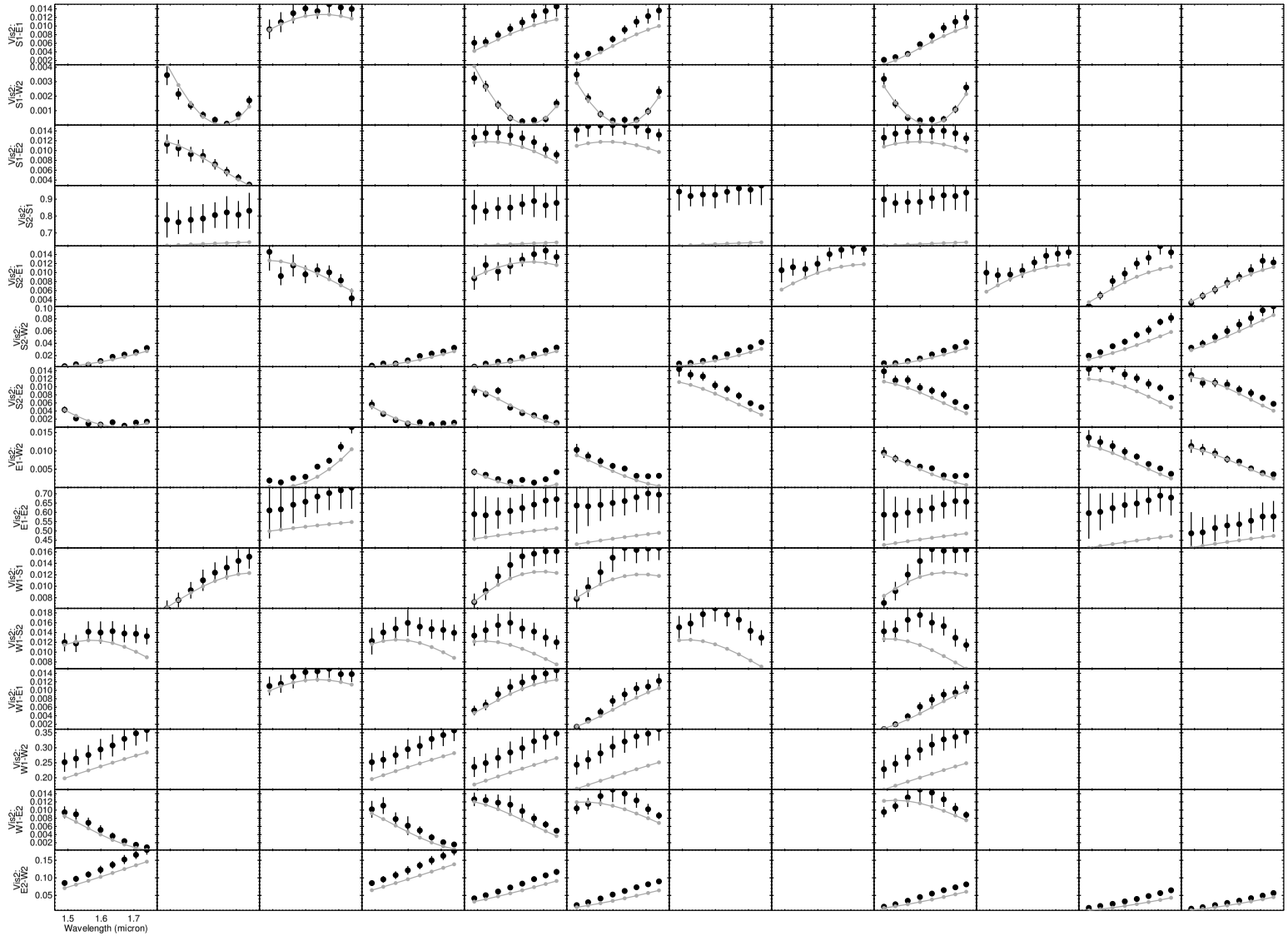

Figure E.2: Squared visibilities of the 2012 Jun 18 observations of o Dra with CHARA/MIRC. Each block of observations represents a temporal block of observations. The data are plotted in black and model is overplotted in gray.

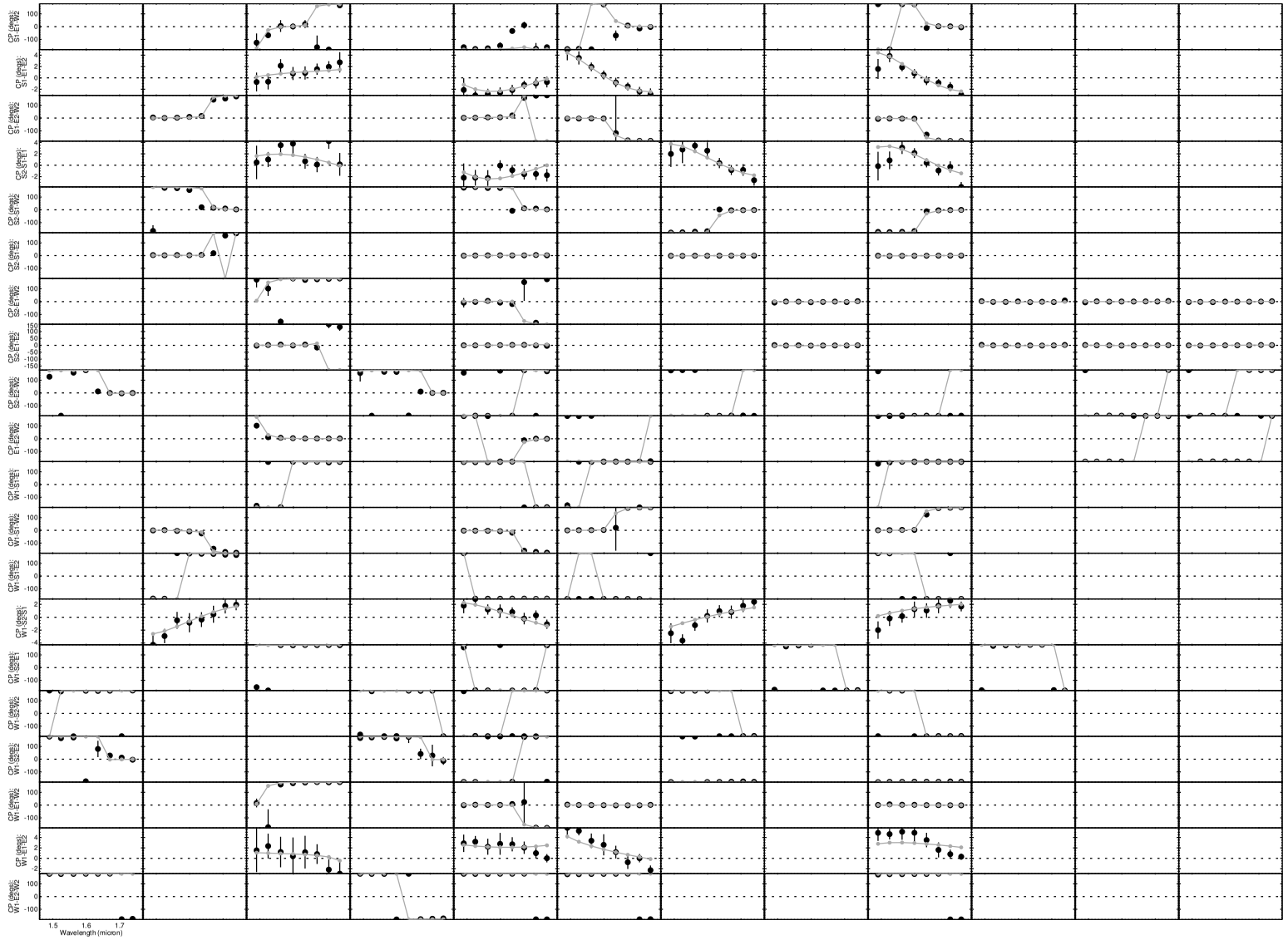

Figure E.3: Closure phases of the 2012 Jun 18 observations of o Dra with CHARA/MIRC plotted as in Figure E.2.

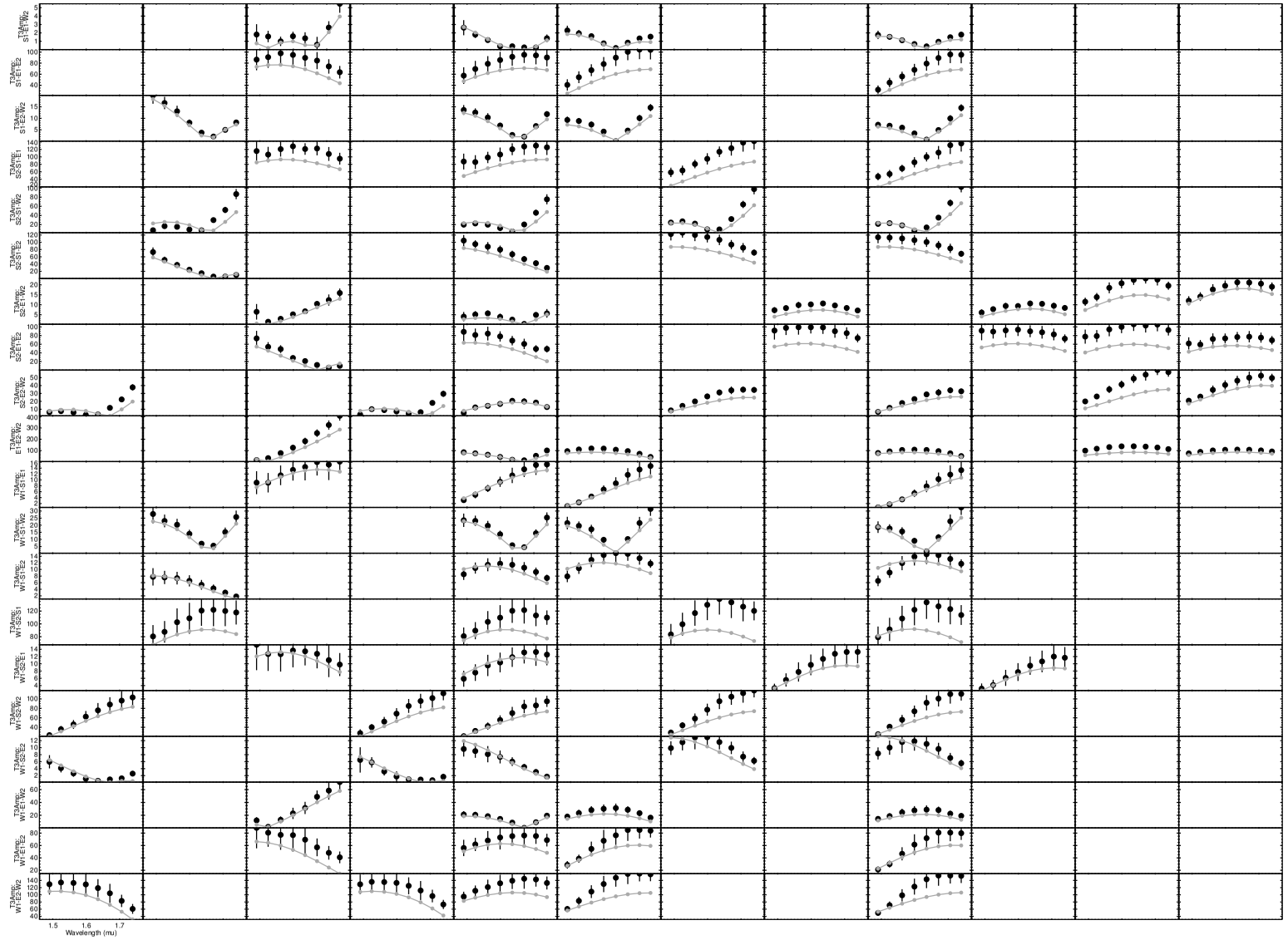

Figure E.4: Triple amplitudes (multiplied by 10^4 for clarity) of the 2012 Jun 18 observations of *o* Dra with CHARA/MIRC plotted as in Figure E.2.

APPENDIX F

Interferometric Observables of ζ And

The data products obtained from reducing the CHARA/MIRC data with the standard pipelines consist of visibilities, closure phases, and triple amplitudes. Representative samples of the observables are presented in Figures F.1 − F.4 for a single night (UT 2013 September 15) of six-telescope CHARA/MIRC observations of ζ And.

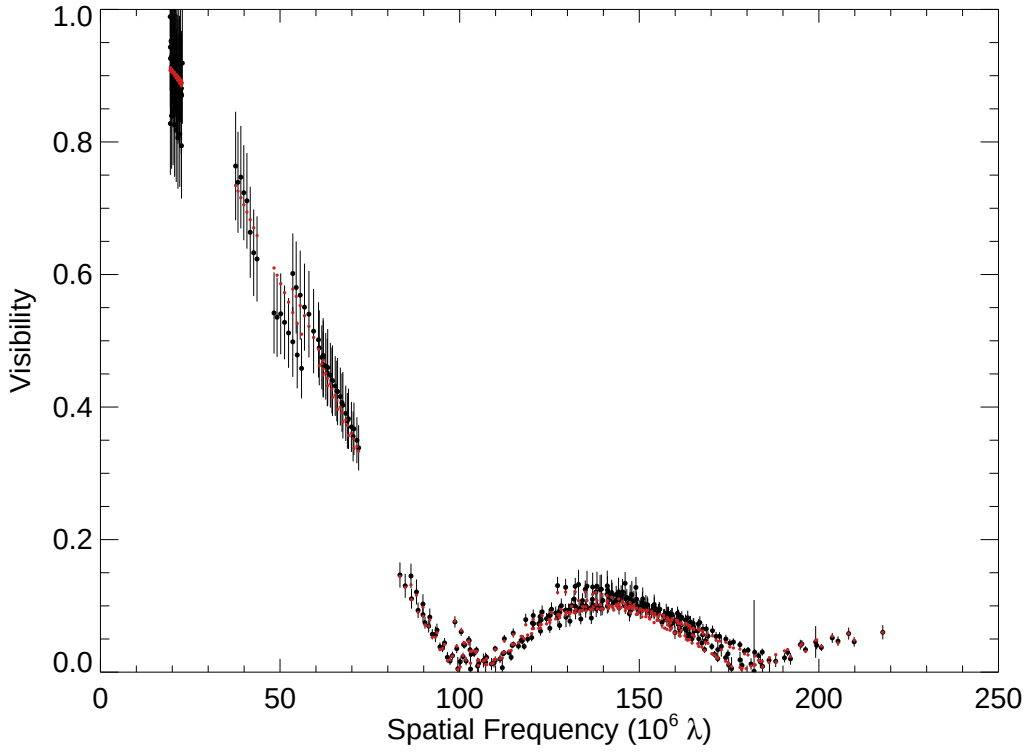

Figure F.1: Visibility curve of UT 2013 September 15 observations of ζ And with CHARA/MIRC. The observed visibilities are plotted in black with 1σ error bars and the SURFING model visibilities are overlaid in red.

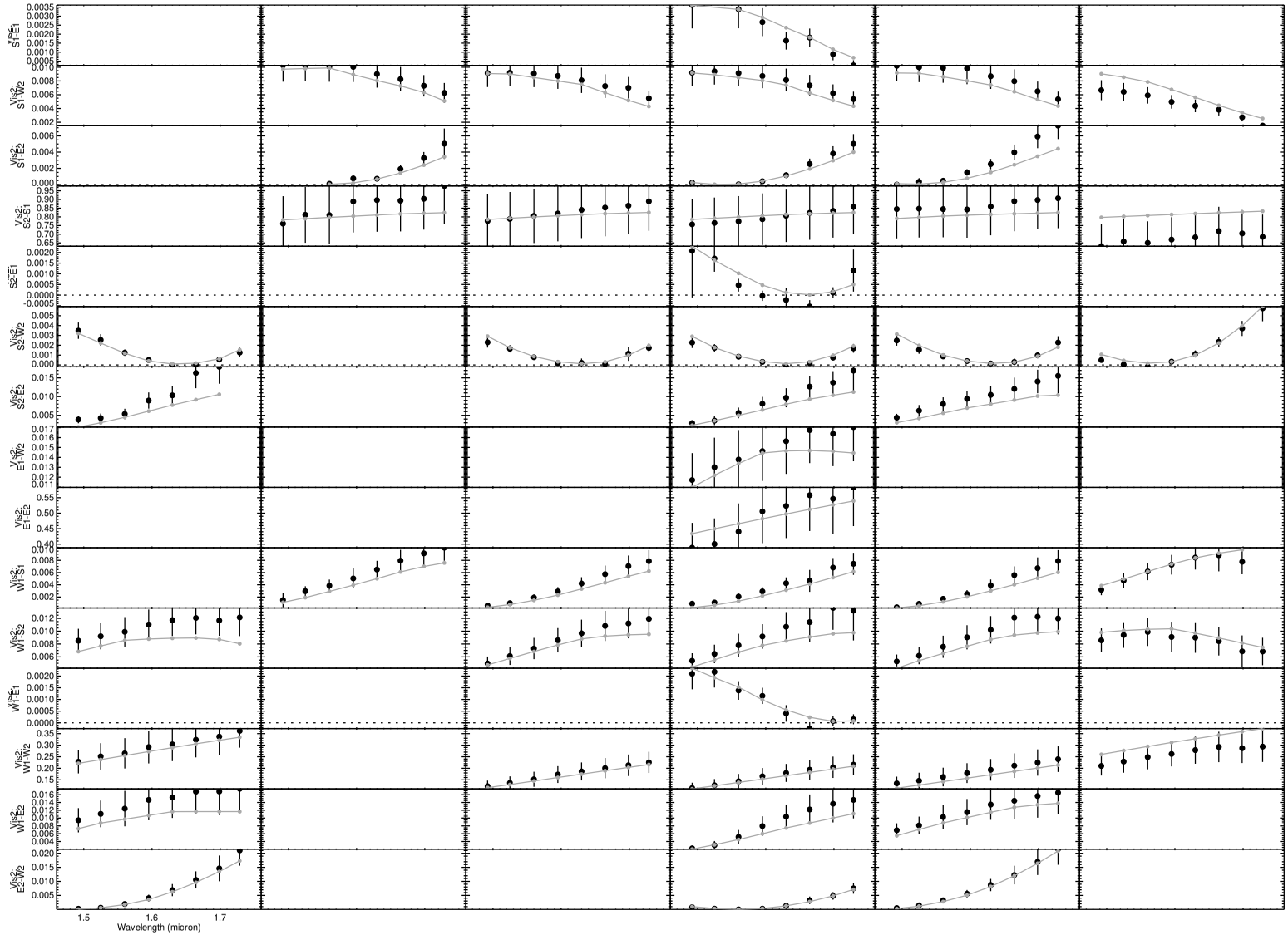

Figure F.2: Squared visibilities of the 2013 Sep 15 observations of ζ And with CHARA/MIRC. Each block of observations represents a temporal block of observations. The data are plotted in black and model is overplotted in gray.

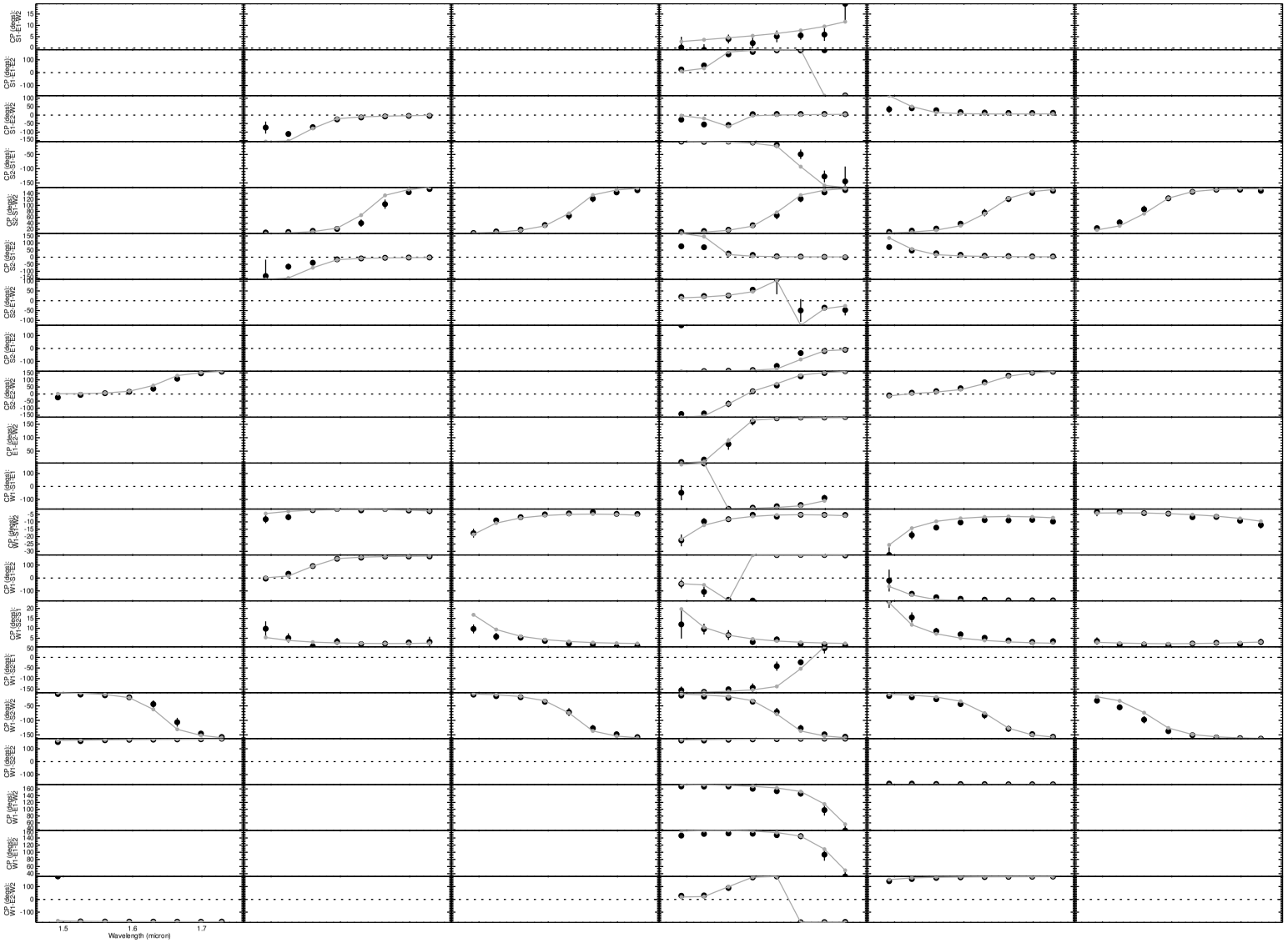

Figure F.3: Closure phases of UT 2013 September 15 observations of ζ And with CHARA/MIRC. Each block represents a temporal block of observations with data plotted in black (with 1σ errors) and SURFING model in gray.

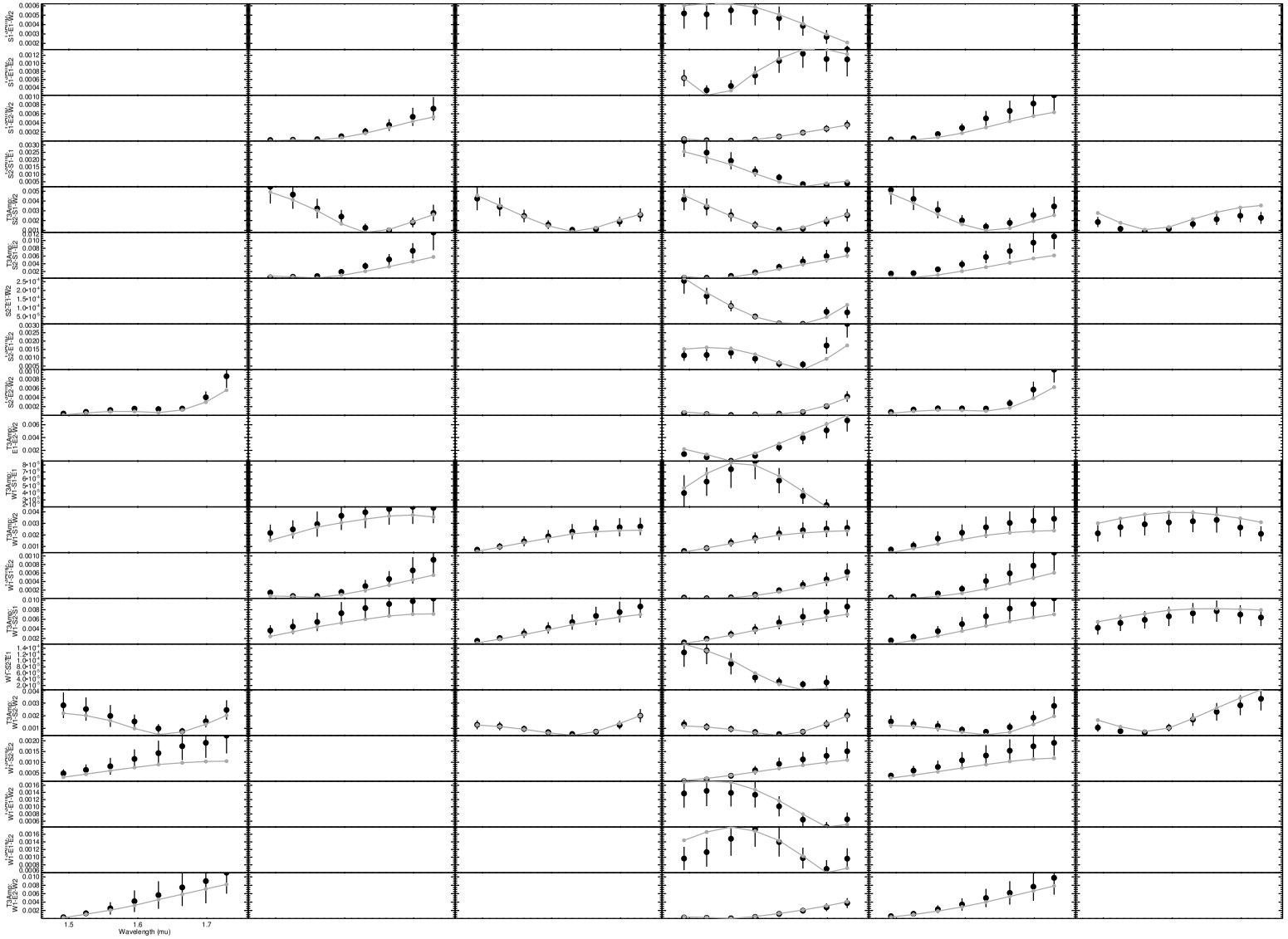

Figure F.4: Triple amplitudes of UT 2013 September 15 observations of ζ And with CHARA/MIRC. Each block represents a temporal block of observations with data plotted in black (with 1σ errors) and SURFING model in gray.

BIBLIOGRAPHY

BIBLIOGRAPHY

Adams, E. R., Ciardi, D. R., Dupree, A. K., et al. 2012, AJ, 144, 42

Adams, E. R., Dupree, A. K., Kulesa, C., & McCarthy, D. 2013, AJ, 146, 9

Anderson, D. R., Hellier, C, Gillon, M., et al. 2010, ApJ, 709, 159

Aurière, M., Konstantinova-Antova, R., Charbonnel, C., et al. 2015, A&A, 574, A90

Babcock, H. W. 1947, ApJ, 105, 105

Babcock, H. W. 1961, ApJ, 133, 572

Baraffe, I., Chabrier, G., Barman, T. 2008, A&A, 482, 315

Baraffe, I., Chabrier, G., Barman, T. 2010, Rep. Prog. Phys., 73, id. 016901

Barclay, T., Still, M., Jenkins, J. M., Howell, S. B., & Roettenbacher, R. M. 2012, MNRAS, 422, 1219

Barnes, J. R., Jeffers, S. V., Jones, H. R. A., et al. 2015, ApJ, 812, 42

Baron, F., Monnier, J. D., Kiss, L. L., et al. 2014, ApJ, 785, 46

Basri, G., Laurent, R. & Walter, F. M. 1985, ApJ, 298, 761

Basri, G., Walkowicz, L. M., Batalha, N., et al. 2010, ApJL, 713, L155

Basri, G., Walkowicz, L. M., Batalha, N., et al. 2011, AJ, 141, 20

Basri, G., Walkowicz, L. M., Reiners, A. 2013, ApJ, 769, 37

Basu, S. & Antia, H. M. 2003, ApJ, 585, 553

Bathala, N. M., Rowe, J. F., Bryson, S. T., et al. 2013, ApJS, 204, 24

Batten, A. H., Fletcher, J. M., & Mann, P. J. 1978, PDAO, 15, 121

Berdyugina, S. V. 2005, LRSP, 2, 8

Berdyugina, S. V., Berdyugin, A. V., Ilyin, I., & Tuominen, I. 1998, A&A, 340, 437

Berdyugina, S. V., Berdyugin, A. V., Ilyin, I., & Tuominen, I. 1999, A&A, 350, 626

Berdyugina, S. V. & Tuominen, I. 1998, A&A, 336, L25

Böhm-Vitense, E. 2004, AJ, 128, 2436

Bonneau, D., Clausse, J.-M., Delfosse, X., et al. 2006, A&A, 456, 789

Borucki, W. J., Koch, D., Basri, G., et al. 2010, Science, 327, 977

Borucki, W. J., Koch D. G., Basri, G., et al. 2011a, ApJ, 728, 117

Borucki, W. J., Koch D. G., Basri, G., et al. 2011b, ApJ, 736, 19

Borrero, J. M. & Ichimoto, K. 2011, LRSP, 8, 4

Bouvier, J. & Bertout, C. 1989, A&A, 211, 99

Boyajian, T. S., von Braun, K., van Belle, G., et al. 2012, ApJ, 757, 112

Boyajian, T. S., McAlister, H. A., van Belle, G., et al. 2012, ApJ, 746, 101

Brandenburg, A. & Dobler, W. 2002, AN, 323, 411

Brown, T. M., Latham, D. W., Everett, M. E., & Esquerdo, G. A. 2011, AJ, 142, 112

Bruls, J. H. M. J., Solanki, S. K., & Schuessler, M. 1998, A&A, 336, 231

Burke, C.J., et al. 2014, ApJS, 210, 19

ten Brummelaar, T. A., McAlister, H. A., Ridgway, S. T., et al. 2005, ApJ, 628, 453

Castelli, F. & Kurucz, R. L. 2004, Modelling of Stellar Atmospheres, ed. N. Piskunov et al., IAU Symp., 210 [arXiv:astro-ph/0405087]

Chaboyer, B., Green, E. M., & Liebert, J. 1999, AJ, 117, 1360

Charbonneau, P. 2005, LRSP, 2, 2

Charbonneau, P., Christensen-Dalsgaard, J., Henning, R., et al. 1999, ApJ, 527, 445

Che, X., Monnier, J. D., Zhao, M., et al. 2011, ApJ, 732, 68

Christian, C. A. & Janes, K. A. 1977, PASP, 89, 415

Claret, A. 2009, A&A, 507, 377

Claret, A. & Bloemen, S. 2011, A&A, 529, 75

Claret, A., Hauschildt, P. H., Witte, S. 2013, A&A 522, 16

Collier Cameron, A., Donati, J.-F., & Semel, M. 2002, MNRAS, 333, 339

Craig, I. J. D., & Brown, J. C. 1986, Inverse Problems in Astronomy (Boston, MA: A. Hilger)

Crossfield, I. J. M, Biller, B., Schlieder, J. E., et al. 2014, Nature, 505, 654

Cutri, R. M., Skrutskie, M. F., van Dyk, S., et al. 2003, yCat, 2246, 0

David, E.-M., Quintana, E. V., Fatuzzo, M., & Adams, F. C. 2003, PASP, 115, 825

Djurašević, G., Rovithis-Livaniou, H., Rovithis, P., et al. 2006, A&A, 445, 291

Donati, J.-F., Jardine, M. M., Gregory, S. G. et al. 2007, MNRAS, 380, 1297

Donati, J.-F. & Landstreet, J. D. 2009, ARA&A, 47, 333

Dotter, A., Chaboyer, B., Javremović, D. et al. 2008, ApJS, 178, 89

Ducati, J. R., 2002, yCat, 2237, 0

Dümmler, R., Ilyin, I. V., & Tuominen, I. 1997, A&AS, 123, 209

Eastman, J., Gaudi, B. S., & Agol, E. 2013, PASP, 125, 83

Eaton, J. A., & Williamson, M. H. 2004, SPIE, 5496, 710

Eaton, J. A., & Williamson, M. H. 2007, *PASP*, 119, 886

Eberhard G. & Schwarzschild K. 1913, ApJ, 38, 292

Eggleton, P. P. 1983, ApJ, 268, 368

Eker, Z. 1986, MNRAS, 221, 947

ESA. 1997, The Hipparcos and Tycho Catalogues (ESA SP-1200)

Espinosa Lara, F. & Rieutord, M. 2011, A&A, 533, 43

Espinosa Lara, F. & Rieutord, M. 2012, A&A, 547, 32

Fekel, F. C., Henry, G. W., & Lewis, C. 2005, AJ, 130, 794

Fekel, F. C., Strassmeier, K. G., Weber, M., & Washuettl, A. 1999, A&ASS, 137, 369

Fekel, F. C., Tomkin, J., & Williamson, M. H. 2009, AJ, 137, 3900

Foreman-Mackey, D., Hogg, D. W., Lang. D., & Goodman, J. 2013, PASP, 125, 306

Frasca, A., Fröhlich, H.-E., Bonanno, A., et al. 2011, A&A, 532, 81

Fried, R. E., Eaton, J. A., Hall, D. S., et al. 1983, Ap&SS, 93, 305

Frölich, H.-E., Frasca, A., Catanzaro, G., et al. 2012, A&A, 543, 146

Fűrész, G., 2008, PhD Thesis, Univ. Szeged

Galileo, G. Istoria e Dimostrazioni Intorno Alle Macchie Solari. Rome, 1613.

Gallenne, A., Mérand, A., Kervella, P., et al. 2015, A&A, 579, 68

Głębocki, R. & Stawikowski, A. 1977, Acta Astron., 27, 225

Głębocki, R. & Stawikowski, A. 1979, Acta Astron., 29, 505

Głębocki, R. & Stawikowski, A. 1988, A&A, 189, 199

Gondoin, P. 2005, A&A, 444, 531

Górski, K., M., Hivon, E., Banday, A. J., et al. 2005, ApJ, 622, 159

Gu, S.-H., Tan, H.-S., Wang, X.-B., & Shan, H.-G. 2003, A&A, 405, 763

Gurzadyan, G. A. & Cholakyan, V. G. 1995, Ap&SS, 229, 185

Halbwachs, J. L. & Pourbaix, D. 2005, in Proc. of the Gaia Symp.: The Three-Dimensional Universe with Gaia, eds. C. Turon, K. S. O'Flaherty, & M. A. C. Perryman, 576, 575

Hale, G. E. 1908, PASP, 20, 220

Hall, D. S. 1976, in ASSL Vol. 60: IAU Colloq. 29: Multiple Periodic Variable Stars, ed. W. S. Fitch (Dordrect: Reidel), 287

Hall, D. S. 1986, ApJ, 309, L83

Hall, D. S. 1991, in The Sun and Cool Stars: Activity, Magnetism, Dynamos, Lecture Notes in Physics, Vol. 380, ed. I. Tuominen, D. Moss, & G. Rüdiger (Berlin: Springer-Verlag), 353

Hall, D. S., Henry, G. W., Landis, H. J. 1977, IBVS, 1328, 1

Hall, D. S. & Persinger, W. T. 1986, in LNP Vol. 254: Cool Stars, Stellar Systems and the Sun, eds. M. Zeilik & D. M. Gibson, 88

Harmon, R. O. & Crews, L. J. 2000, AJ, 120, 3274

Harper, W. E. 1935, PDAO, 6, 207

Harrison, T. E., Coughlin, J. L., Ule, N. M., & López-Morales, M. 2012, AJ, 143, 4

Hatzes, A. P. 1993, ApJ, 410, 777

Hatzes, A. P. 1998, A&A, 330, 541

Hauschildt, P. H., Allard, F., Ferguson, J., Baron, E., & Alexander, D. R. 1999, ApJ, 525, 871

Heintz, W. D. 1978, Double Stars (Dordrecht: Reidel)

Henry, G. W. 1999, PASP, 111, 845

Henry, G. W., Eaton, J. A., Hamer, J., & Hall, D. S. 1995, ApJS, 97, 513

Herbig, G. H. & Spalding, J. Jr. 1955, ApJ, 121, 118

Hevelius, J. 1647, Selenographia. Danzig: Andres Hënefeld

Hillenbrand, L. A. & White, R. J. 2004, ApJ, 604, 741

Holzwarth, V., Mackay, D. H., & Jardine, M. 2006, MNRAS, 369, 1703

Hotta, H. & Yokoyama, T. 2011, ApJ, 740, 12

Hunt-Walker, N. M., Hilton, E. J., Kowalski, A. F., Hawley, S. L., & Matthews, J. M. 2012, PASP, 124, 545

Hut, P. 1981, A&A, 99, 126

Jenkins, J. M., Caldwell, D. A., Chandrasekaran, H., et al. 2010, ApJ, 713, L87

Jetsu, L. 1996, A&A, 314, 153

Kajatkari, P., Hackman, T., Jetsu, L., Lehtinen, J., & Henry, G. W. 2014, A&A, 562, 107

Kane, S. R., Schneider, D. P., & Ge, J. 2007, MNRAS, 377, 1610

Kane, S. R. & Gelino, D. M. 2012, MNRAS, 424, 779

Kasting, J. F., Whitmire, D. P., & Reynolds, R. T. 1993, Icarus, 101, 108

Kawahara, H., Hirano, T., Kurosaki, K, Ito, Y., & Ikoma, M. 2013, ApJL, 776, L6

Kenyon, S. J. & Hartmann, L. 1995, ApJS, 101, 117

Kervella, P., Mérand, A., Pichon, B., et al. 2008, A&A, 488, 667

Kiurkchieva, D. P. 1989, Astroph. Space Sci., 155, 125

Koch, D. G., Borucki, W. J., Basri, G., et al. 2010, ApJ, 713, L79

Koch, R. H. & Hrivnak, B. J. 1981, AJ, 86, 438

Korhonen, H., Berdyugina, S. V., & Tuominen, I. 2002, A&A, 390, 179

Korhonen, H., Wittkowski, M., Kővári, Zs., et al. 2010, A&A , 515, 14

Kővári, Zs., Kriskovics, L., Künstler, A. et al. 2015, A&A, 573, 98

Kővári, Zs., Bartus, J., Strassmeier, K. G., et al. 2007a, A&A, 463, 1071

Kővári, Zs., Bartus, J., Švanda, M., et al. 2007b, AN, 328, 1081

Kővári, Zs., Korhonen, H., Kriskovics, L., et al. 2012, A&A, 539, A50

Kővári, Zs., Strassmeier, K. G., Bartus, J. et al. 2001, A&A, 373, 199

Kron, G. E. 1947, PASP, 59, 261

Kron, G. E. 1950a, ASP Leaflets, 6, 52

Kron, G. E. 1950b, AJ, 55, 69

Küker, M., Rüdiger, G., & Kitchatinov, L. L. 2011, A&A, 530, 48

Kurucz, R. L. 1979, ApJSS, 40, 1

Latham, D. W. 1992, in IAU Coll. 135, Complementary Approaches to Double and Multiple Star Research, ASP Conf. Ser. 32, ed. H. A. McAlister, & W. I. Hartkopf (San Francisco, CA: ASP) 110

Lehmann, H., Southworth, J., Tkachenko, A., & Pavlovski, K. 2013, A&A, 557, A79

van Leeuwen, F. 2007, A&A, 474, 653

Leighton, R. B. 1964, ApJ, 140, 1547

Leighton, R. B. 1969, ApJ, 156, 1

López-Morales, M. 2007, ApJ, 660, 732

Luck, R. E. 1991, ApJS, 75, 579

Lucy, L. B. 1967, Zs. Ap., 65, 89

Lucy, L. B. & Sweeney, M. A. 1971, AJ, 76, 544

Luyten, W. J. 1936, ApJ, 84, 85

Mackay, D. H., Jardine, M., Collier Cameron, A., Donati, J.-F., Hussain, G. A. J. 2004, MNRAS, 354, 737

Maeder, A. & Meynet, G. 2012, Rev. Mod. Phys., 84, 25

Mallik, S. V. 1998, A&A, 338, 623

Mamajek E. E. & Hillenbrand L. A. 2008, ApJ, 687, 1264

Mason, B. D., Wycoff, G. L., Hartkopf, W. I., et al. 2015, yCat, 102026

Massarotti, A., Latham, D. W., Stefanik, R., & Fogel, J. 2008, AJ, 135, 209

Mathys, G. 1989, Fundam. Cosmic Phys., 13, 143

Maunder, E. W. 1894, Knowledge, 17, 173

Maunder, E. W. 1904, MNRAS, 64, 747

Mayor, M. & Mermilliod, J.-C. 1984, Observational Tests of the Stellar Evolution Theory, ed. A. Maeder, A. Renziniin, in IAU Symp., 105, 411

Mazeh, T. 2008, EAS, 29, 1

Mazeh, T., Holczer, T., & Shporer, A. 2015, ApJ, 800, 142

McDonald, I., Zijlstra, A. A., Boyer, M. L. 2012, MNRAS, 427, 343

McWilliam, A. 1990, ApJS, 74, 1075

Mochejska, B. J., Stanek, K. Z., Sasselov, D. D., & Szentgyorgyi, A. H. 2002, AJ, 123, 3460

Mochejska, B. J., Stanek, K. Z., Sasselov, D. D., et al. 2005, AJ, 129, 2856

Monnier, J. D. 2007, New Astron. Rev., 51, 604

Monnier, J. D., Berger, J., Millan-Gabet, R., & ten Brummelaar, T. A. 2004, Proc. SPIE, 5491, 1370

Monnier, J. D., Che, X., Zhao, M., et al. 2012, ApJL, 761, L3

Monnier, J. D., Pedretti, E., Thureau, N., et al. 2006, Proc. SPIE, 6268, 62681

Monnier, J. D., Zhao, M., Pedretti, E., et al. 2007, Science, 317, 342

Monnier, J. D., et al. in preparation

Mosser, B., Baudin, F., Lanza, A. F., et al. 2009, A&A, 506, 245

Moultaka, J., Ilovaisky, S. A., Prugniel, P., and Soubiran, C. 2004, PASP, 116, 821

Nelson, E. R. & Zeilik, M. 1990, ApJ, 349, 163

Nicolet, B. 1978, A&AS, 34, 1

Nielsen, M. B., Gizon, L., Schunker, H., & Karoff, C. 2013, Progress in Physics of the Sun and Stars: A New Era in Helio- and Asteroseismology, ed. H. Shibahashi & A. E. Lynas-Gray, in ASPC, 479, 137

Noyes, R. W., Hartmann, L. W., Baliunas, S. L., Duncan, D. K., & Vaughan, A. H. 1984, ApJ, 279, 763

O'Neal, D., Saar, S. H., & Neff, J. E. 1996, ApJ, 463, 766

Oláh, K., Moór, A., Kővári, Zs., et al. 2014, A&A, 572, 94

Oláh, K., Panov, K. P, Pettersen, B. R., Valtaoja, E., & Valtaoja, L. 1989, A&A 218, 192

Orosz, J. A. & Hauschildt, P. H. 2000, A&A, 364, 265

Padmakar & Pandey, S. K. 1999, A&AS, 138, 203

Parker, E. N. 1955, ApJ, 122, 293

Parks, J. R., White, R. J., Schaefer, G. H., Monnier, J. D., & Henry, G. W. 2011, ASPC, 448, 1217

Parks, J. R., White, R. J., Baron, F., et al. submitted to ApJ

Paxton, B. 2004, PASP, 116, 699

Petrov, P. P. 2003, Astrophys., 46, 506

Pinsonneault, M. H., An, D., Molenda-Żakowicz, J., et al. 2012 ApJS, 199, 30

Piskunov, N. & Wehlau, W. H. 1994, A&A, 289, 868

Pizzolato, N., Maggio, A., Micela, G., Sciortino, S., & Ventura, P. 2003, A&A, 397, 147

Poe, C. H. & Eaton, J. A. 1985, ApJ, 289, 644

Pourbaix, D. 2002, A&A, 385,686

Pourbaix, D. & Boffin, H. M. J. 2003, A&A, 398, 1163

Pourbaix, D., Tokovinin, A. A., Batten, A. H. et al. 2004, A&A, 424 727

Prato, L., Simon, M., Mazeh, T., et al. 2002, ApJ, 569, 863

Quintana, E. V., Jenkins, J. M., Clarke, B. D., et al. 2010, Proc. SPIE, 7740

Reiners, A., Basri, G., & Browning, M. 2009, ApJ, 692, 538

Richichi, A., Percheron, I., & Khristoforova, M. 2005, A&A, 431, 773

Roettenbacher, R. M., Harmon, R. O., Vutisalchavakul, N., & Henry, G. W. 2011, AJ, 141, 138

Roettenbacher, R. M., Monnier, J. D., Harmon, R. O., Barclay, T., & Still, M. 2013, ApJ, 767, 60

Roettenbacher, R. M., Monnier, J. D., Fekel, F. C., et al. 2015, ApJ, 809, 159

Roettenbacher, R. M., Monnier, J. D., & Harmon, R. O. 2015, 18th Cambridge Workshop on Cool Stars, Stellar Systems, and the Sun, ed. G. van Belle and H. C. Harris, 377

Roettenbacher, R. M., Monnier, J. D., Henry, G. W., et al. 2015, ApJ, 807, 23

Roman, N. G. 1952, ApJ, 116, 122

Rutter, R. G. M. & Schrijver, C. J. 1987, A&A, 177, 155

Saar, S. H. & Donahue, R. A. 1997, ApJ, 485, 319

Sanchis-Ojeda, R., Winn, J. N., Holman, M. J., et al. 2011, ApJ, 733, 127

Savanov, I. S. 2011a, ARep, 55, 341

Savanov, I. S. 2011b, ARep, 55, 801

Savanov, I. S. & Dmitrienko, E. S. 2011, ARep, 55, 890

Savanov, I. S. & Dmitrienko, E. S. 2012, ARep, 56, 116

Savanov, I. S. & Strassmeier, K. G. 2008, AN, 329, 364

Scarfe, C. D., Batten, A. H., & Fletcher, J. M. 1990, Publ. Dominion Astrophys. Obs., 18, 21

Schatzman, E. 1962, Ann. Astrop., 25, 18

Schröder, K.-P. & Connon Smith, R. 2008, MNRAS, 386, 155

Schwabe, H. 1844, AN, 21, 233

Siess, L., Dufour, E., & Forestini, M. 2000, A&A, 358, 593

Simon, T. & Fekel, F. C., Jr. 1987, ApJ, 316, 434

Spruit, H. C. 1982, A&A, 108, 348

Somers, G. & Pinnsoneault, M. H. 2015, ApJ, 807, 174

Soubiran, C., Le Campion, J.-F., Cayrel de Strobel, G., & Caillo, A. 2010, A&A, 515, 111

Stassun, K. G., Mathieu, R. D., & Valenti, J. A. 2007, ApJ, 664, 1154

Stawikowski, A. & Głębocki, R. 1994, Acta Astron., 44, 393

Stefanik, R. P., Latham, D. W., & Torres, G. 1999, in Precise Stellar Radial Velocities, ASP Conf. Series 185, IAU Colloq. 17:. Eds. J. B. Hearnshaw & C. D. Scarfe, 354

Still, M., & Barclay, T. 2012, Astrophysics Source Code Library, 8004

Strassmeier, K. G. 1999, A&A, 347, 225

Strassmeier, K. G. 2009, A&ARv, 17, 251

Strassmeier, K. G., Hall, D. S., Boyd, L. J., & Genet, R. M. 1989, ApJS, 69, 141

Strassmeier, K. G., Hall, D. S., Eaton, J. A., et al. 1988, A&A, 192, 135

Strassmeier, K. G., Hall, D. S., Henry, G. W. 1994, A&A, 282, 535

Strassmeier, K. G., Rice, J. B., Wehlau, W. H., et al. 1991, A&A, 247, 130

Street, R. A., Horne, K., Lister, T. A., et al. 2005, MNRAS, 358, 795

Sullivan, P. W., Winn, J. N., Berta-Thompson, Z. K., et al. 2015, ApJ, 809, 77

Thompson, S. E. & Fraquelli, D. 2012, Kepler Archive Manual, KSCI-10008-003

Torres, G., Anderson, J., & Giménez, A. 2010, A&ARv 18, 67

Twomey, S. 1977, Introduction to the Mathematics of Inversion in Remote Sensing and Indirect Measurements (Amsterdam: Elsevier)

Unruh, Y. C. & Collier Cameron, A. 1997, MNRAS, 290, L37

Vaquero, J. M. & Vázquez, M. 2009, The Sun Recorded through History (New York: Springer)

Vogt, S. S. & Penrod, G. D. 1983, PASP, 95, 565

Walter, F. M. 1985, PASP, 97, 643

Walter, K. 1949, Nature, 164, 1129

Weiss, L. M. & Marcy, G. W. 2014, ApJ, 783, L6

White, T. R., Huber, D., Maestro, V., et al. 2013, MNRAS, 433, 1262

Wright, N. J., Drake, J. J., Mamajek, E. E., & Henry, G. W. 2011, ApJ, 743, 48

Yang, S.-C., Sarajedini, A., Deliyannis, C. P., et al. 2013, ApJ, 762, 3

Young, R. K. 1921, JRASC, 15, 161

Young, A. & Koniges, A. 1977, ApJ, 211, 836

Zahn, J.-P. 1977, A&A, 57, 383

Zahn, J.-P. & Bouchet, L. 1989, A&A, 223, 112

von Zeipel, H. 1924, MNRAS, 84, 655

Zhao, M., Monnier, J. D., Pedretti, E., et al. 2009, ApJ, 701, 209